Understanding of fission dynamics from fragment mass distribution studies

By

Nishant Kumar

Enrolment Number: PHYS01201304027

Bhabha Atomic Research Centre, Mumbai

A thesis submitted to the

Board of Studies in Physical Sciences

In partial fulfillment of requirements

For the Degree of

DOCTOR OF PHILOSOPHY

of

HOMI BHABHA NATIONAL INSTITUTE

May, 2019

Homi Bhabha National Institute

Recommendations of the Viva Voce Board

As members of the Viva Voce Board, we certify that we have read the dissertation prepared by Nishant Kumar entitled "Understanding of fission dynamics from fragment mass distribution studies" and recommend that it may be accepted as fulfilling the dissertation requirement for the Degree of Doctor of Philosophy

Chairman : Dr. B. K. Nayak _______ Date: 17/11/2020

Guide/Convener : Dr. D. C. Biswas Biswas _______ Date: 16/11/2020

Examiner : Prof. Surjit Mukherjee _______ Date: 25/11/2020

Member 1 : Dr. B. V. John Benay John _______ Date: 27/11/2020

Member 2 : Dr. R. Tripathi _______ Date: 25/11/2020

Member 3 : Dr. T. K. Ghosh T. Ghosh _______ Date: 20/11/20

Final approval and acceptance of this dissertation is contingent upon the candidate's submission of the final copies of the dissertation to HBNI.

I hereby certify that I have read this dissertation prepared under my direction and recommend that it may be accepted as fulfilling the dissertation requirement.

Biswas

Date: 16-11-2020

Place: Mumbai

Guide

STATEMENT BY AUTHOR

This dissertation has been submitted in partial fulfillment of requirements for an advanced degree at Homi Bhabha National Institute (HBNI) and is deposited in the Library to be made available to borrowers under rules of the HBNI.

Brief quotations from this dissertation are allowable without special permission, provided that accurate acknowledgement of source is made. Requests for permission for extended quotation from or reproduction of this manuscript in whole or in part may be granted by the Competent Authority of HBNI when in his or her judgement the proposed use of the material is in the interests of scholarship. In all other instances, however, permission must be obtained from the author.

Nishant Kumar

Nishant Kumar

DECLARATION

I, hereby declare that the investigation presented in the thesis has been carried out by me. The work is original and has not been submitted earlier as a whole or in part for a degree / diploma at this or any other Institution / University.

Nishant Kumar

Nishant Kumar

List of Publications

Publications relevant to the thesis

Referred Journals:

1. "Role of quasifission in fission fragment mass distributions for the ^{28}Si + ^{197}Au reaction", **Nishant Kumar**, D. C. Biswas, T. K. Ghosh, J. Sadhukhan, B. N. Joshi, Y. K. Gupta, R. P. Vind, G. K. Prajapati, Shradha Dubey, L. S. Danu, S. Mukhopadhyay, K. Mahata, B. V. John, and S. Sodaye, Phys. Rev. C 99, 041602(R) (2019).

2. "Fission fragment velocity distribution measurement using time of flight technique", D. C. Biswas, R. P. Vind, **Nishant Kumar**, Y. K. Gupta, R. V. Jangale, A. L. Inkar, L. A. Kinage, B. N. Joshi, S. Mukhopadhyay, G. K. Prajapati, Shradha Dubey, Nuclear Inst. and Methods in Physics Research, A 901 (2018) 76–83.

Chapter in Book:

1. "Development of position sensitive multi-wire gas detectors for Nuclear Physics Experiments", D.C. Biswas, R.P. Vind, **Nishant Kumar**, R.V. Jangale, A.L. Inkar, Y.K. Gupta, A.T. Chaudhari, L.S. Choughule, Manish Kumar, BARC News Letter, January-February, 2018, P-7.

Conference Proceedings:

1. "Fission fragment mass distribution studies in ^{9}Be + ^{232}Th fission reaction", **Nishant Kumar**, Y. K. Gupta, B. N. Joshi, G. K. Prajapati, L. S. Danu, S. Mukhopadhyay, B. V. John, S. Dubey, D. C. Biswas, Proceedings of DAE-BRNS International Symp. on Nucl. Phys. (2018), 684.

N. Shant Kumar

2. "Role of quasi-fission on fragment mass distribution in ^{28}Si + ^{197}Au reaction", **N. Kumar**, B. N. Joshi, T. K. Ghosh, R. P. Vind, G. K. Prajapati, L. S. Danu, Y. K. Gupta, S. Mukhopadhyay, R. G. Thomas, S. Dubey, K. Mahata, B. V. John, D. C. Biswas, Proceedings of DAE-BRNS Symp. on Nucl. Phys. 62, (2017), 404.

3. "Fission fragment mass distribution studies for ^{28}Si + ^{197}Au, ^{209}Bi, ^{235}U reactions", **Nishant Kumar**, B. N. Joshi, R. P. Vind, G. K. Prajapati, S. Dubey, L. S. Danu, S. Mukhopadhyay, K. Mahata, S. Sodaye, T. K. Ghosh, B. V. John, D. C. Biswas, Proceedings of DAE-BRNS Symp. on Nucl. Phys. 60, (2015), 378.

Other Publications

Referred Journals:

1. "Affirmation of transfer-breakup as a source for α-particle emission in $^{12,13}C$ + ^{232}Th fission reactions", Y. K. Gupta, D. C. Biswas, G. K. Prajapati, L. S. Danu, B. N. Joshi, S. Mukhopadhyay, B. V. John, S. Dubey, Siddarth Chettri, N. Kumar, R. P. Vind, and S. Mukherjee, Phys. Rev. C 98, 041601(R) (2018).

Conference Proceedings:

1. "Multi-nucleon transfer and fission cross sections for ^{28}Si + ^{197}Au, ^{209}Bi and ^{232}Th reactions at 179 MeV", D. C. Biswas, **Nishant Kumar**, Shradha Dubey, G. K. Prajapati, B. N. Joshi, K. Mahata, Y. K. Gupta, S. Mukhopadhyay, L. S. Danu, S. Sodaye, R. P. Vind, B. V. John, Proceedings of DAE-BRNS Symp. on Nucl. Phys. 60, (2015), 568.

Nishant Kumar

2. "Characterization of a ΔE_{gas}-E_{Si-Pad} hybrid detector telescope for fission fragments", R. P. Vind, **Nishant Kumar**, R. V. Jangale, Omeshwari Bisen, Abhilasha Singh, Shradha Dubey, A. L. Inkar, L. A. Kinage, G. K. Prajapati, B. N. Joshi, B. V. John, D. C. Biswas, Proceedings of DAE-BRNS Symp. on Nucl. Phys. 60, (2015), 1060.

3. "Energy and timing characteristics of Silicon-Pad detector for fission fragments", **Nishant Kumar**, R. P. Vind, R. V. Jangale, L. A. Kinage, A. L. Inkar, S. Mukhopadhyay, B. V. John, D. C. Biswas, Proceedings of DAE-BRNS Symp. on Nucl. Phys. 60, (2015), 1062.

4. "Measurement of high-energy γ-rays in spontaneous fission of ^{252}Cf", R. P. Vind,D. C. Biswas, **N. Kumar**, Y. K. Gupta, Reha Grover, S. Dubey, R. V. Jangale, A. L. Inkar, D. R. Chakrabarty, Proceedings of DAE-BRNS Symp. on Nucl. Phys. 61, (2016), 314.

5. "Fission fragement angular anisotropy in ^{18}O+^{232}Th,^{209}Bi fission at 110 and 125 MeV", B. N. Joshi, **N. Kumar**, Y. K. Gupta, L. S. Danu, R. P. Vind, G. K. Prajapati, S. Mukhopadhyay, B. V. John, D. C. Biswas, K. Mahata, I. Mazumdar, Proceedings of DAE-BRNS Symp. on Nucl. Phys. 61, (2016), 520.

6. "Variation of Nuclear level density parameter as function of excitation energy", G. K. Prajapati, Y. K. Gupta, B. N. Joshi, L. S. Danu, **N. Kumar**, Shradha Dubey, S. Mukhopadhyay, B. V. John, R. P. Vind, D. C. Biswas, Proceedings of DAE-BRNS Symp. on Nucl. Phys. 62, (2017), 412.

7. "Transfer angular distributions in ^{12,13}C + ^{232}Th and ^{13}C + ^{206,208}Pb reactions at E_{Beam} =75 MeV", Y. K. Gupta, S. Chettri, D. C. Biswas, G. K. Prajapati, B. N. Joshi, S. Dubey, L. S. Danu, S. Mukhopadhyay, **N. Kumar**, R. P. Vind, B. V. John, R. V. Jangale, A. L. Inkar, Proceedings of DAE-BRNS Symp. on Nucl. Phys. 62, (2017), 620.

8. "Measurement of fission fragment angular anisotropy and level density parameter in ^{18}O+^{209}Bi reaction", B. N. Joshi, **Nishant Kumar**, Y. K. Gupta, L. S. Danu, G. K. Prajapati, R. P. Vind, S. Mukhopadhyay, S. Dubey, B. V. John, K. Mahata, I. Mazumdar, D. C. Biswas, Proceedings of DAE-BRNS International Symp. on Nucl. Phys. (2018), 440.

9. "Investigation of nuclear level density in the temperature range of 1 to 3 MeV for a mass region of A ~110", G. K. Prajapati, Y. K. Gupta, B. N. Joshi, L. S. Danu, **N. Kumar**, S. Dubey, S. Mukhopadhyay, R. P. Vind, B. V. John, D. C. Biswas, Proceedings of DAE-BRNS International Symp. on Nucl. Phys. (2018), 676.

Nishant Kumar

Dedicated to my parents

ACKNOWLEDGEMENTS

I would like to express my sincere gratitude to my Ph.D. Supervisor, Dr. D. C. Biswas for his invaluable guidance and encouragement throughout my thesis work. I am also grateful to him for careful draft's reading of this thesis and his valuable suggestions. He is a wonderful teacher, and is a source of knowledge that I will be very thankful throughout my career.

I express my sincere thanks to Dr. B. K. Nayak, Head Nuclear Physics Division, for his many helpful disccussions and suggestions. I would like to express my sincere appreciation to Dr. T. K. Ghosh, VECC, Kolkata for his useful suggestions and guidance in the experimental work. I also thank Dr. B. V. John, Dr. R. Tripathi and Dr. Alok Saxena for their valuable suggestions at different stages of thesis work. I would like to express my profound gratitude to Mr. R. P. Vind who played a key role in development of MWPC for their use in this thesis work. The technical support received from Mr. R.V. Jangle, Mr. A. L. Inkar, Mr. L. A. Kinage is greatly acknowledged all along the development of MWPC detector and smooth running of experiments. I gratefully acknowledge Dr. B. N. Joshi, Mr. G. K. Prajapati, Mr. L. S. Danu, Dr. S. Mukhopadhyay, Dr. Shradha Dubey, and Dr. Y. K. Gupta for hours spent explaining the various aspects of nuclear Physics, electronics, data acquisition system, and the data analysis in the early part of my Ph.D. I learned many things and enjoyed performing different experiments. I wish to thank J. Sadhukhan for valuable discussions and inputs during theoretical calculation of thesis work. I thank Dr. K. Mahata and Dr. S. Sodaye for their valuable discussions during the experiment time. I sincerely thank all the members of doctoral committee for their kind support and many fruitful suggestions during this thesis work.

I also thank all the administrative staff at BARC, NPD office, for their cooperation related to administrative paperwork. I am very grateful to the LINAC-Pelletron staff at TIFR for smooth operation of the accelerator during the experiments.

Nishant Kumar

Contents

List of Figures

List of Tables

Chapter 1

Introduction

Nuclear fission is one of the most important discovery in the history of modern science. This has made a profound influence in the field of nuclear physics and has triggered many other important discoveries both in basic as well as applied nuclear physics research. The fission of a nucleus was first observed by Hahn and Strassmann in 1939 when they bombarded Uranium target with the neutrons from a Ra-Be source [1]. In nuclear fission, a nucleus splits into two more or less, equal nuclei along with the emission of neutrons, gamma rays, light charged particles and a large amount of energy (~200 MeV). Meitner and Frisch compared the nucleus with charged liquid drop and gave the explanation of the fission process [2]. The liquid drop model (LDM) provided the first qualitative picture of the fission process, which has been developed over the years by Bohr and Wheeler, Swiatecki and others [3–5]. During the complex nuclear fission dynamics, various degrees of freedom such as the elongation (deformation), mass asymmetry, etc. are involved in the multi-dimensional potential energy surface which governs the dynamical evolution of the fissioning nucleus from ground state to the stage where two fission fragments are in just touching configuration. In the description of the LDM, the collective motion in the fission degree of freedom is caused by the oppositely varying surface and Coulomb energies as a function of deformation. In addition to the macroscopic aspects of bulk matter such as surface and Coulomb energies, the fission process is also influenced by the microscopic effects of the finite number of fermions (e.g., shell correction). On the basis of the LDM one gets the smooth variation of the potential energy with deformation as shown by the dashed line in the Fig. 1.1, and after incorporating the shell effects, the potential energy curve is modified to double hump shape as shown by the solid line.The existence of double hump barrier explains various low energy fission observables such as asymmetric mass distribution, occurrence of spontaneous fission isomers, etc [6]. Although, many of the basic features of actinide fission were described by Bohr and Wheeler soon after the discovery, the fission process is very complex involving large scale rearrangement of the nucleons. Though the phenomenon of nuclear fission was discovered about 80 years back, it continues to be very interesting even today. It has been a challenge for both theorists and experimentalists to obtain a satisfactory understanding of the fission phenomena.

In heavy ion induced fission reactions, the interacting nuclei in the nuclear many body system undergo dynamical evolution and finally divides into two fragments. Kramers [7] pointed out the importance of dissipation in the nuclear fission process. In the statistical model of fission, it is considered that after the formation of the compound nucleus, the fall time from saddle to scission point were very fast as compared to the transition time up to saddle point and does not have any influence in the fission process. Fig. 1.2 shows the statistical decay of compound nucleus.

Heavy ion induced fission is a unique tool for probing the nuclear potential-energy landscape as a function of elongation, mass asymmetry, spin, and excitation energy, from the single 'compound-nucleus' system over the top of the fission barrier. Finally, it reaches the scission point and culminating in the formation of two fission fragments, along with emission of neutrons, light charged particles and gamma rays, which carry information about the fission dynamics. This transition involves a subtle interplay of collective (macroscopic) and single-particle (microscopic) effects, such as shell effects and pairing, all of which considered both for the initial nuclei and for the final fission fragments. With

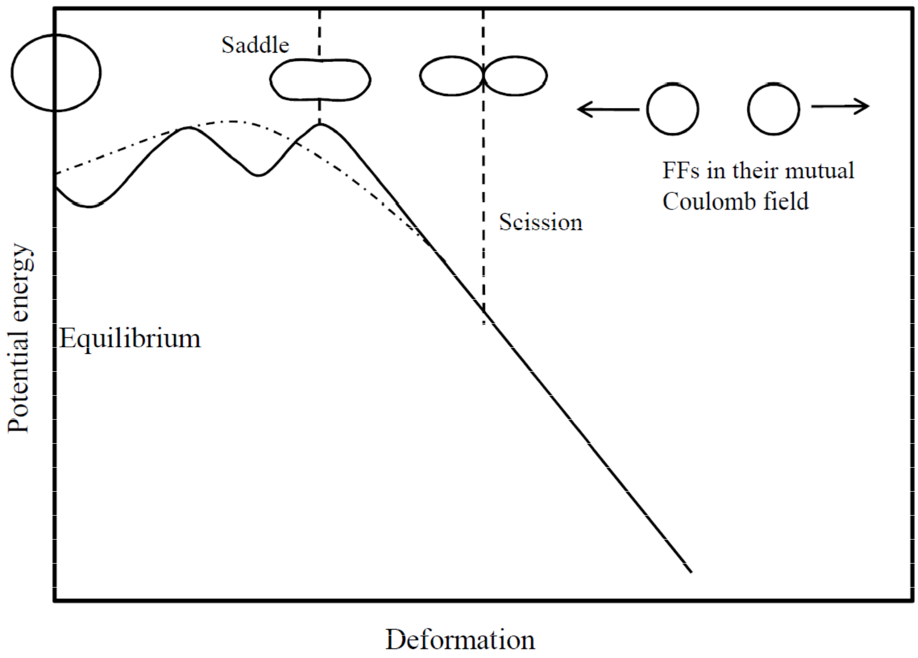

Figure 1.1: Schematic diagram of potential energy as a function of deformation calculated using liquid drop model (dashed line) and after incorporating shell corrections (solid line).

the advent of advanced accelerators, it is possible to populate states with high excitation and high spin in heavy ion induced reactions. The mass, charge and angular momentum distribution of fission fragments is sensitive to dynamics of heavy ion induced fission. The topic of heavy-ion induced fission fragment mass and angular distribution is rather unique, as it has been possible through this study to have insight regarding the evolution of the composite system formed during the interaction of two nuclei [8]. The shape and width of fission-fragment (FF) mass distribution provides a lot of information on the fission reaction mechanism and the structure of the compound nucleus (CN), the fragments as well as the interacting nuclei. From mass angle correlation studies one can learn about the degree of equilibration in mass degree of freedom.

Nucleus-nucleus collisions at moderate bombarding energies exhibit a broad spectrum of reaction types ranging from direct process (elastic, inelastic, knock-out, multi-nucleon transfer etc.) to fully equilibrated compound nucleus formation. For large impact parameters associated with peripheral collisions, a negligible overlap of the colliding nuclei occurs, and mostly direct reaction processes take place. For small impact parameters, the

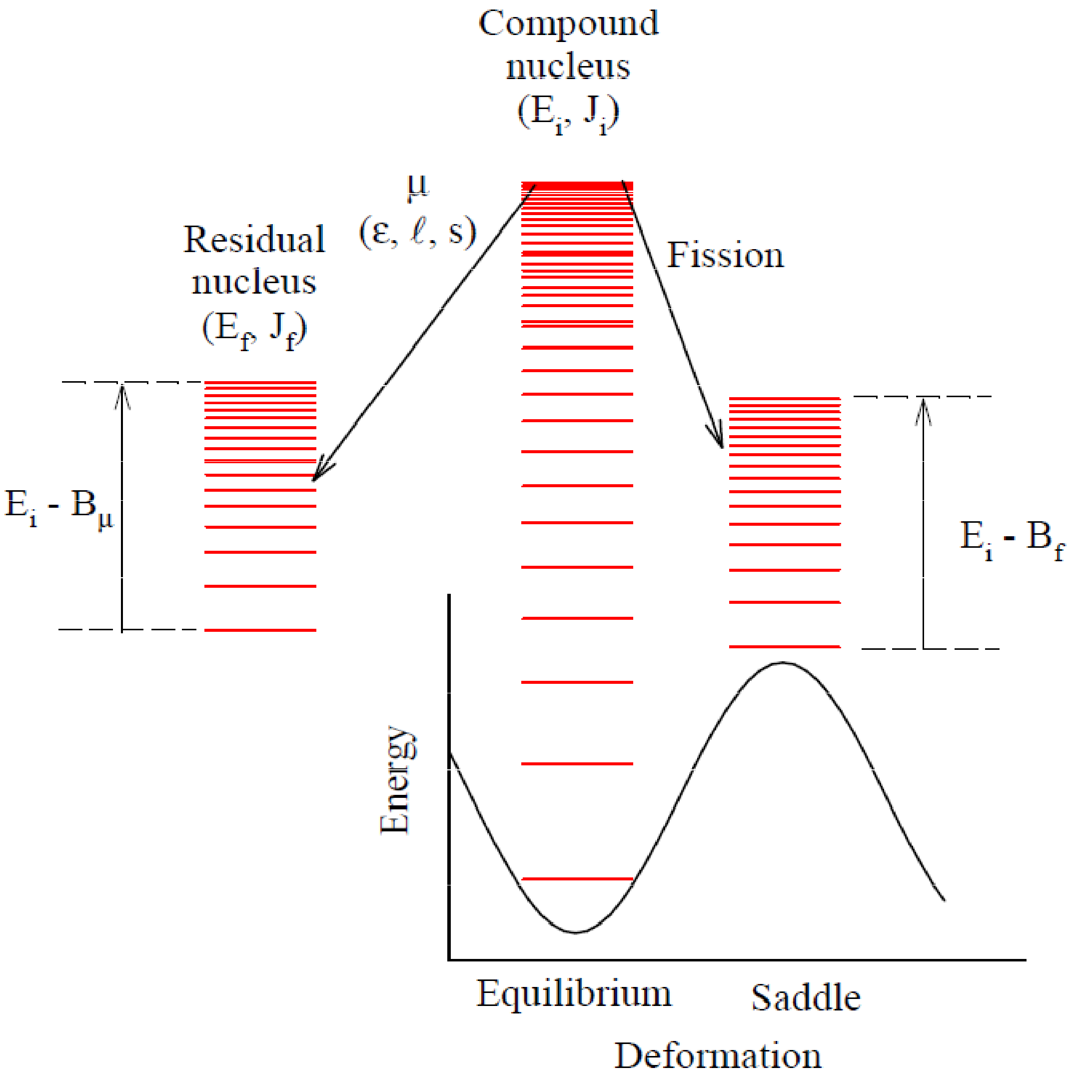

Figure 1.2: Schematic diagram showing compound nuclear fission as a statistical decay. Notation 'μ' refers to different types of particles such as neutron, proton, alpha particle, etc. and B_μ is the separation energy of the particle.

projectile and target nuclei can fuse to form a compound nucleus.

1.1 Classification of nuclear reactions

The two body simple nuclear reaction can be represented as

$$a + X \rightarrow Y + b \tag{1.1}$$

or, in more compact notation, X(a, b)Y. In this notation, X is the target nucleus, a is the projectile, b is generally light ejected particle, Y is the residual nucleus. Based on the Q-value, we can classify nuclear reactions into elastic and inelastic types. In case of elastic collision, Q = 0, so that the initial and final states of the colliding particles are the same. In all other processes where Q≠0 can be classified as inelastic scattering or nuclear reactions. In many reactions, there may be more than two particles in the exit channel. The different kind of collisions are as follows:

1.1.1 Elastic Scattering

In Elastic scattering, before and after the scattering the projectile and target remain in their ground states. Kinetic energy is the same before and after scattering in the center of mass system. Elastic scattering can be used to get information on the interaction radii, surface thickness (diffuseness), interaction potential (via the optical model potential calculations), grazing angular momentum, and reaction cross-sections. This is a peripheral collision in terms of impact parameter.

$$a + X \rightarrow X + a \tag{1.2}$$

1.1.2 Direct Reactions

1. Inelastic Scattering: In this type of scattering, interacting particles remain unchanged before and after scattering, but one or both of the interacting particles may be excited through a mutual excitation process with corresponding reduction in initial kinetic energy as in,

$$a + X \rightarrow X^{*} + a^{*} \tag{1.3}$$

   The cross section for such inelastic scattering provides information on the nuclear spin and parity of the excited states.

2. Transfer Reactions: In transfer reactions, when the projectile passes over the periphery of the target nucleus, one or more nucleons are transferred between the projectile and the target. When the projectile gains the nucleons from the target, then the transfer reaction is called “Pick up reaction”. When, projectile loses the nucleons to the target nucleus, then the transfer reaction is called “Stripping reaction”.

3. Knock-out reactions: In this kind of reactions, a nucleon or light nucleus gets ejected from the target nucleus in presence of the projectile. This will produce three particles in the final state. In this reaction the projectile remains free before knocking the target nucleon or light nucleus, in a process known as quasi-free scattering.

In the direct interaction process two nuclei make just glancing contact. For this reason these types of reactions are also known as peripheral reactions. It is assumed that in this kind of reactions nuclear particles enter or leave the target nucleus without disturbing other nucleon that are available in the nuclear shell. The time span for these kind of reactions are $\sim 10^{-21}$ sec. Direct reactions may proceed from initial to final partition without going through the intermediate state. Direct reactions are very suitable in providing information regarding the relation (overlap) between the ground state of target nucleus and a ground or a particular excited state of a residual nucleus.

1.1.3 Compound Nuclear Reactions

When both the target and projectile nuclei interact at very small impact parameter, they fuse together as a single equilibrated compound nucleus. It was proposed in 1936 by Niels Bohr [3, 4] to explain nuclear reactions as two stage process comprising the formation of relatively long lived intermediate nucleus and its subsequent decay. First a bombarding projectile loses all its energy to the target nucleus and becomes an integral part of a new, highly excited, unstable nucleus, called compound nucleus. The formation stage takes the time approximately equal to the time interval (Δt) for the bombarding particle to travel across the diameter (2R) of the target nucleus:

$$\Delta t \sim \frac{2R}{c} \sim 10^{-21} s. \tag{1.4}$$

The hot compound nucleus is highly excited and has a temperature depending on the bombarding energy of the projectile. It also carries angular momentum equal to the vector sum of the angular momentum of the relative motion in the entrance channel and the spins of the initial collision partners. The excitation energy and the angular momentum of the compound nucleus are eventually released via a decay process, into smaller fragments. For compound nucleus at excitation energies corresponding to incident laboratory energies E<10 MeV/A of the fused system, the decay can be categorized in two main schemes viz., evaporation residue formation and nuclear fission.

1.1.4 Heavy ion collisions

Due to the small De Broglie wave lengths, heavy-ion collisions can be approximately described by the semi-classical picture, where the trajectories of the collisions depend on initial conditions such as the impact parameter, relative velocity, Z and A of the colliding nuclei, as well as the long range Coulomb and short range nuclear forces acting between them. It is customary to use the impact parameter ‘b’ or the orbital angular momentum ‘l’ to distinguish between different reaction processes. The impact parameter is defined as the perpendicular distance between the path of a projectile and the target. At a given impact parameter ‘ b ’, the entrance channel orbital angular momentum is $\vec{l} = \vec{b} \times \vec{p}$, where $\vec{p}$ is the momentum of the incident projectile in center of mass frame. Fig. 1.3 shows the classification of different reaction processes as a function of impact parameter, ‘b’. For

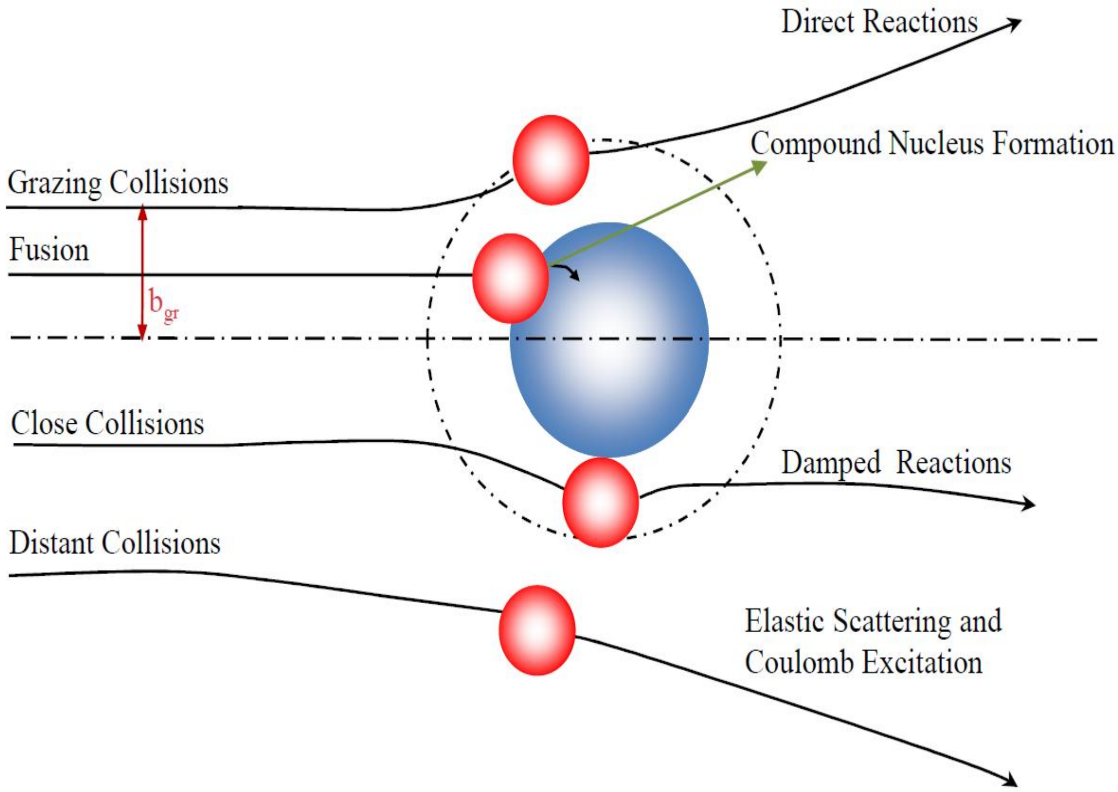

Figure 1.3: Schematic representation of different types of heavy-ion reactions as a function of impact parameter, ‘b’.

very large values of ‘b’, a negligible overlap of the colliding nuclei occurs, and interaction takes place mainly through the Coulomb field. These processes include Rutherford scattering or elastic scattering, and Coulomb excitation. The elastic scattering data have been extensively used to derive the internuclear potential by means of optical model analysis. In Coulomb excitation, the electromagnetic forces between the two interacting nuclei excite the low lying excitations. For grazing collisions, the most likely outcome is that the nuclei will scatter elastically, or the process may involve internal excitation to the intrinsic states of the interacting nuclei (inelastic scattering). For small overlapping encounters, nucleons may be exchanged, either in successive steps or as clusters resulting in both energy and angular momentum transfer from the relative motion into internal degrees of freedom (transfer reactions). For closer impacts, the two nuclei may partially coalesce for a short time before separating again. During these collisions, a noticeable dissipation of available kinetic energy and angular momentum takes place into the internal degrees of freedom of the reaction partners. The outgoing reaction partners have relatively good memory of the entrance channel parameters such as the mass, charge, etc. During these so called deep inelastic collisions, the composite system may undergo some amount of rotation before reaction partners (dominantly projectile and target like) reseparate. In case of more central collisions, the two nuclei fuse together, where the total excitation energy and angular momentum is equilibrated inside the compound nucleus.

For reactions with heavy targets, nuclear fission process is one of the dominant decay processes involving large scale collective nuclear motion. Heavy ion fusion-fission reaction paths are largely governed by the potential energy, impact parameter and the bombarding energy above the Coulomb barrier. The dynamical evolution of a nuclear many body system can be described theoretically in terms of suitable collective coordinates which are coupled to the intrinsic degress of freedom by means of dissipative processes. From the various investigations carried out since early eighties, it is now well recognized that there is large scale damping of collective modes in heavy ion induced fission reactions, which results in large dynamical delays in the fission decay. Study of the onset of nuclear damping signalling the transition from order to chaos in nuclear systems is very important from the point of understanding the behaviour of many body systems.

Compared to n/γ or light-ion induced fission, the use of heavier projectiles allows to study fission of nuclei further away from the β-stability line, especially on the proton-rich side and in the region of superheavy nuclei, in addition to spontaneous fission (SF)/beta delayed fission (βDF). The accessible nuclei are determined both by the projectile-target combination and also by the reaction type, e.g. fusion–fission, quasi-fission (QF) or

Multi-nucleon transfer induced fission (MNTF). For fusion-fission or compound nucleus fission (CNF), a compact configuration is formed after complete equilibration in mass, charge, energy and angular momentum degrees of freedom and the excited compound nucleus undergoes fission with the signatures of fusion-fission process. In some cases, the unstable elongated di-nucleus may also re-separate into two heavy fragments instead of diffusing to more compact stable equilibrated shapes and this premature separation of fission fragments (FFs) is called QF. The characteristic differences between fusion–fission/QF and MNTF reactions is that a full momentum transfer (FMT) happens in the former case, whereas, in case of MNTF, the momentum transfer is either less than FMT or more than FMT depending on the beam energy [9]. Hence, the recoil momenta (velocities) of the composite fissioning nuclei in two reactions are different. This, in turn, results in different folding angles (θ_{fold}) of fission fragments in the laboratory frame, where θ_{fold} is defined as the sum of the emission angles θ_1 and θ_2 of the fission fragments relative to the beam direction. As all the mechanisms can occur in a given reaction, the difference in the folding angle is often used in the follow-up data analysis to differentiate their relative contributions. The deviation of the experimental data of fission anisotropies and mass distribution when compared to the theoretical model predictions are explained as a consequence of an admixture of compound nucleus (CNF) and Non-Compound Nucleus (NCN) fission. These NCN events include fast fission, quasi-fission and pre-equilibrium fission.

1. Compound Nuclear Fission

   The compound nucleus (CN) which is formed by the fusion process is hot and highly excited and carries a large amount of angular momentum. Therefore, the survival probability of the CN is small and it will decay to ground state by different modes that is dependent on the mass of CN. In low mass region (A<200), the CN decays from the excited state after evaporating light particles and gamma rays depending upon the phase space available. The residual target-like nucleus is called the evaporation residue. A process in which the CN decays in this very asymmetric fashion is called fusion evaporation reaction. In the mass region, 200 < A_{CN} < 300, CN will decay by emitting light particles followed by fission process. In this process fusion-fission takes place and symmetrical mass distribution is favored.

2. Fast Fission

   The fast fission [10, 11, 13] is expected to take place for the composite system of larger fissilities when the angular-momentum-dependent fission barrier drops below the nuclear temperature. At this stage the shape may become triaxial. In view of the extremely small barrier close to zero, the composite system is unstable and fission-like events take place without full equilibration.

3. Quasi-fission

   The quasi-fission [5, 12, 13] takes place for composite system in which the unconditional saddle-point (fission barrier) shape is more compact than the entrance-channel contact configuration. This kind of mechanism where the two interacting ions reseparate without forming the compound nucleus is expected to take place more for systems involving moderately heavier projectiles (A > 20) but with fission barrier not as small as it was in the case of fast fission. Experimentally, the presence of quasi-fission is associated with the observation of not only large values of anisotropies, but also wider mass distributions and a correlation of mean fragment mass with angle [14, 15]. A clear picture of what are the most important entrance channel characteristics that either enhance or hinder QF is still a matter of discussion. QF appears as an elusive and multi-faceted process, which is strongly connected with the reaction entrance channel. Three criteria are widely used to identify the reaction mechanism (fusion or QF).

   - The reaction Coulomb factor Z_1Z_2 (charge product of reaction partners). This parameter relates to the Coulomb energy in the entrance channel. According to the calculations in the frame of macroscopic–microscopic model of Swiatecki [5] the threshold value of Z_1Z_2 for the appearance of QF is 1600.

- Entrance channel mass asymmetry $\alpha_0 = (A_T - A_P)/(A_P + A_T)$. Here A_P and A_T are projectile and target mass respectively. Unexpected fusion suppression observed in quite asymmetric combinations of colliding nuclei can be qualitatively explained in the framework of the liquid drop Businaro–Gallone picture, i.e., by an effect of the conditional barrier arising along the mass asymmetry coordinate on a path to the formation of a spherical CN. The fusion probability P_{CN}, as a measure of the fusion suppression effect, correlates with the entrance-channel mass asymmetry. According to this criterion, QF appears for systems with entrance channel mass asymmetry lower than the Businaro–Gallone mass asymmetry defined as [16]:

$$\alpha_{BG} = \begin{cases} 0, & \chi_{CN} < 0.396 \\ 1.12\sqrt{\frac{\chi_{CN}-0.396}{\chi_{CN}-0.156}}, & \chi_{CN} > 0.396 \end{cases} \tag{1.5}$$

where

$$\chi_{CN} = \frac{Z_{CN}^2/A_{CN}}{50.883(1-1.7826(\frac{N_{CN}-Z_{CN}}{A_{CN}})^2)} \tag{1.6}$$

Here χ_{CN} is the fissility parameter of the CN.

- Effective fissility parameter χ_{eff} connected with repulsive and attractive forces in the entrance channel [17]

$$\chi_{eff} = \frac{4Z_1Z_2/(\sqrt[3]{A_1}\sqrt[3]{A_2}(\sqrt[3]{A_1}+\sqrt[3]{A_2})}{50.83(1-1.7826(\frac{A_{CN}-2Z_{CN}}{A_{CN}})^2)} \tag{1.7}$$

A mean fissility parameter was proposed in the “extra–extra-push” model [18]. This parameter is defined as a linear combination between effective fissility parameter and true fissility parameter χ_{CN} reflecting the stability of CN with respect to fission. Recently, the following mean fissility parameter was proposed in [19]:

$$\chi_m = 0.75\chi_{eff} + 0.25\chi_{CN} \tag{1.8}$$

From the analysis of a large data set of mass-angle distributions of fission-like fragments obtained in the reaction with heavy ions it has been found that the QF takes place for reactions with $\chi_m > 0.68$ and becomes dominant at $\chi_m >$ 0.765.

These criteria, however, are not universal. For instance, they do not take into account the shapes of the interacting nuclei. The relative orientation of deformed nuclei changes the Coulomb barrier and the distance between the centers of the colliding nuclei and this leads to a change in the balance between repulsive and attractive forces. When two interacting nuclei touch each other by their lateral surfaces (near-side collisions), a high formation probability of a spherical CN is expected, whereas in the elongated configuration, when nuclei touch each other by their poles (near-tip collisions), a high QF probability is expected. The influence of nuclear orientation on QF (the so-called orientation effect) was observed experimentally for the first time at sub-barrier energies in the reactions with deformed nuclei ^{12}C $+^{232}$Th, ^{16}O $+^{238}$U [20–22] and extensively studied in the reactions ^{48}Ca $+^{144,154}$Sm [23, 24], ^{16}O + ^{238}U, ^{30}Si $+^{238}$U and ^{34}S $+^{238}$U [25–29]. The interaction energy is also a very important parameter for QF. The relative contribution of QF process decreases when the interaction energy increases. The question about the influence of angular momentum on the QF process is furthermore still open, and additional experimental data on QF fragments together with gamma-rays emission are needed to shed light on this point.

4. Pre-equilibrium fission

The pre-equilibrium (PEQ) fission [30] is a decay mode, which competes with the compound nucleus fission when the fission barrier height is comparable to its temperature. The PEQ events occur in a time scale comparable to the characteristic relaxation time of the K-degree (the projection of total angular momentum, I on the fission axis) of freedom. In the case of normal CN fission the final K distribution is broader and is influenced by the transition state, the saddle point [30]. However, in the case of PEQ fission, the final K distribution is expected to be very narrow, almost corresponding to the initial value of the composite system. In this sense the PEQ fission may have memory of the entrance channel. The PEQ process is expected even when the fission barrier is non-vanishing in contrast to the fast fission process and it takes place for all the projectiles unlike the quasi-fission phenomena limited to projectiles with A greater than typically 20.

During the nuclear shape evolution, the composite system relaxes in energy, mass, shape, which ultimately reaches the fully equilibrated compound nucleus. It also provides informations related to the diffusion process for the viscous nuclear fluid as it undergoes fission decay. To understand the fission dynamics, we need to have the information of the evolution of composite system from saddle to scission. Experimentally, we can learn about fission dynamics from the following studies: mass distribution of fission fragments, width of mass distribution of fission fragments, mass angle correlation of fission fragments, mass energy correlation of fission fragments, angular distribution of fission fragments, measurement of energies and angular distribution of charged particles emitted during various stages. From the fission fragment angular distribution studies, one can have idea about the shape of the fissioning nuclei at the transition state. It is also sensitive to the entrance channel dynamics of the nuclear reaction process. The mass angle correlations and mass ratio distribution measurements gives information about the occurrence of fission after complete equilibration or partial equilibration of the composite nucleus. At high excitation energy (~50 MeV) the influence of shell effects is negligible and the compound nucleus fission process is well described by the Liquid Drop Model (LDM). According to the LDM the fission into two symmetrical nuclei is energetically favorable. Further, the variance of mass distribution studied at sub and near barrier energies gives important information about the reaction dynamics.

In reactions with heavy-ion beam at energies around the Coulomb barrier (V_b), the relative probability of non-compound processes with respect to CNF depends on entrance channel parameters viz., mass asymmetry, N/Z ratio, the Coulomb factor $Z_P Z_T$ (where, Z_P and Z_T are the atomic number of the projectile and target), deformation, shell structure and orientation of the colliding nuclei. The asymmetric split of ^{180}Hg in β-delayed fission of ^{180}Tl is unsuspected for N/Z ratio of 1.25 of ^{180}Hg [31]. It gave rise to new kind of fission which is still a puzzle for both theoretician as well as experimentalist. Tripathi *et al.* [32], measured fission fragment mass distributions in ^{35}Cl + ^{144,154}Sm reactions populating compound nuclei around mass ~180 amu. The study shows that the mass distribution deviates from that expected on the basis of a pure liquid drop model in the mass region of ~180, indicating a contribution from asymmetric fission. This is consistent with the observation of an asymmetric component in the ^{40}Ca + ^{142}Nd reaction in a recent study [33]. Low-energy β-delayed fission of ^{194,196}At and ^{200,202}Fr was studied in detail at the mass separator ISOLDE at CERN [34]. The fission-fragment mass distributions of daughter nuclei ^{194,196}Po and ^{202}Rn indicate a triple-humped structure, marking the transition between asymmetric fission of ^{178,180}Hg and symmetric fission in the light Ra-Rn nuclei. Thomas *et al.* [35], while studying the entrance channel dependence of quasi-fission in reactions forming ^{220}Th found that the width of the mass distributions of the ^{50}Ti + ^{170}Er system increase with decreasing bombarding energies, in contrast with those of the ^{16}O+^{204}Pb and ^{34}S+^{186}W systems, which show a monotonic reduction in mass widths. The results were interpreted by considering the elongated contact configuration at sub-barrier energies. The influence of nuclear orientation on QF (the so-called orientation effect) was observed experimentally for the first time at sub-barrier energies in the reactions with deformed nuclei ^{12}C +^{232}Th, ^{16}O +^{238}U [21, 22, 36]. Hinde *et al.* [37], measured fission and quasifission mass and angular distribution for reactions with projectiles from C to S, bombarding Th and U target nuclei. It was found that mass-asymmetric quasi-fission occurring on a fast time scale, associated with collisions with the tips of the prolate actinide nuclei, shows a rapid increase in probability with increasing projectile charge, the transition being centered around projectile atomic number $Z_P = 14$.

Prasad *et al.* [38], found strong mass angle correlation of fission fragments for reactions ^{40}Ca+^{186}W and ^{40}C+^{192}Os, populating ^{226}Pu and ^{232}Cm respectively. It was concluded that a compact shape is not achieved for deformation aligned collisions with lower capture barriers for above reactions. In another experiment [39] for reaction ^{34}S + ^{232}Th forming ^{266}Sg, it was found that the mass-asymmetric quasi-fission component, predominantly originating from tip (axial) collisions with the prolate deformed ^{232}Th, is found to be peaked near A = 200 at all energies and center-of-mass angles. Khuyagbaatar *et al.* [40], investigated how the competition between quasifission and fusion-fission evolves with small changes in entrance-channel properties associated mainly with the nuclear structure. Analysis of mass-distribution widths of strongly mass-angle correlated fission fragments within the framework of the compound-nucleus fission theory demonstrates significant differences in quasi-fission (and therefore fusion) probabilities among the four reactions (^{48}Ti + ^{204,208}Pb and ^{50}Ti + ^{206,208}Pb). Itkis *et al.* [41] , studied the entrance channel dependency in formation of Hs nuclei. In the case of the reaction ^{22}Ne+^{249}Cf the mass-energy distributions are in good agreement with Liquid Drop Model (LDM) predictions at energies well below and above the Coulomb barrier, while for the ^{26}Mg+^{248}Cm and ^{36}S+^{238}U reactions some discrepancies (increasing intensities of asymmetric component) between measured and (LDM) predicted mass distributions were observed, especially in the asymmetric mass region. These discrepancies are connected with the QF process, whose contribution increases for the more symmetric ^{36}S+^{238}U reaction. The mass-energy distribution for the ^{58}Fe+^{208}Pb reaction has a wide U shape because QF and not CNF is the dominant process at all measured energies. Chaudhuri *et al.* [42], measured fission fragment mass distribution for reactions ^{16}O+^{184}W and ^{19}F+^{181}Ta, populating the same compound nucleus ^{200}Pb at similar excitation energies. The width of mass distribution for both the reactions was found to be increasing monotonically with excitation energy confirming the absence of quasi-fission for both the reactions. These results were contrary to results predicted on the basis of suppression of Evaporation residue cross section. Chaudhuri *et al.* [43] also measured mass distributions of the fragments in the fission of ^{206}Po and the N = 126 neutron shell closed nucleus ^{210}Po. No significant deviation of mass distributions has been found between ^{206}Po and ^{210}Po, indicating the absence of shell correction at the saddle point in both the nuclei, contrary to the reported angular anisotropy and pre-scission neutron multiplicity results. This result provides benchmark data to test the new fission dynamical models to study the effect of shell correction on the potential energy surface at saddle point. The mass-angle distribution has been reported recently for ^{50}Cr + ^{208}Pb, ^{52}Cr + ^{206,208}Pb, ^{54}Cr + ^{204,208}Pb reactions by Mohanto *et al.* [44]. Two components were observed in the measured fragment mass angle distribution, a fast mass-asymmetric quasi-fission and a slow mass-symmetric component does not have significant mass-angle correlation. The ratio of these components was found to depend on spherical closed shells in the entrance channel nuclei and the magnitude of the N/Z mismatch between the two reaction partners, as well as the beam energy. Recently, Banerjee *et al.* [45], measured fission fragment mass distriubtion in the reactions ^{11}B + ^{232}Th and ^{11}B + ^{243}Am at energies around the barrier. No sudden change in the width of the mass distribution as a function of center-of-mass energy was observed at near-barrier energies, indicating no quasi-fission transition in the near-barrier energies. Interestingly, the previous measurements of fission fragment angular anisotropies for the same systems showed significant departure from the statistical saddle-point model predictions at near-barrier energies, indicating the presence of non-equilibrium fission processes.

1.2 Fission reactions with weakly bound projectiles

The reaction mechanisms involving weakly bound stable projectiles (^{6}Li, ^{7}Li, ^{9}Be etc.) is different from the tightly bound stable projectiles. Large amount of work has been carried out to study the fusion/fusion–fission process and/or breakup using these projectiles in reactions with several heavy targets [46, 47]. The recent experimental results on reactions involving weakly bound projectiles with low breakup threshold energies have shown that either there is enhancement of the fusion cross sections due to the coupling of the breakup channels to fusion or there is fusion hindrance due to the loss of incident flux because of breakup. The mass distribution in ^{6}Li, ^{7}Li + ^{238}U [46] was found to be asymmetric. The Peak to Valley ratio (P/V) was relatively sharply increasing with decreasing energy for ^{6}Li + ^{238}U reaction as compared to ^{7}Li + ^{238}U reaction. This is because of low breakup threshold of ^{6}Li as compared with ^{7}Li. This low breakup threshold leads to increase in contribution of incomplete fusion to the total fusion. More recently Pal *et al.* [48], studied the mass distributions of fission fragments (FFs) from fissioning nuclei ^{241,242,243,244}Pu and ^{240,241}Np populated in multi-nucleon transfer or incomplete fusion (ICF) reactions on ^{6,7}Li + ^{238}U systems. Fissioning nuclei was identified and excitation energies was determined by finding the details of the outgoing projectile-like fragments detected in coincidence with both the fission fragments on an event-by-event basis. It was found that the shell correction for symmetric fission channels plays an important role in describing the experimental mass distribution. In another recent measurement, Sen et al. [49], found the persistence of shell effects at excitation energy of ~31 MeV in mass distribution of fission fragments for reaction α + ^{206}Pb populating ^{210}Po compound nuclei. The small breakup threshold energy of ^{9}Be into ^{8}Be + ^{1}n(1.67 MeV) or into ^{5}He + ^{4}He (2.55 MeV) makes it interesting to study the effect of breakup on fission fragment mass distribution.

Nuclear fission is a complex dynamical process and it is quite evident that that fission fragment mass distribution is very important tool in the understanding of fission dynamics. There are several methods for studying the fission fragment mass distribution; from the coincident measurement of kinetic energies of both the fragments (2E) [50], simultaneous measurement of fragment energy and velocity (E-V) or correlated velocity of both the fission fragments (2V) [51]. In the present thesis work, we have studied the understanding of fission dynamics from fragment mass distribution studies employing 2V technique using a pair of Multi-wire Proportional Counter (MWPC) detectors for simultaneous measurement of time of flight (TOF) of the FFs.

1.3 Probes to study fusion-fission dynamics

The fusion-fission dynamics can be probed experimentally by different kinds of measurements, like detection of particles emitted (n,p,α), evaporation residues, fission fragments, giant dipole resonance γ's which characterize the fission process. By choosing different projectile-target combinations one can study the entrance channel effects. All the above mentioned probes are discussed in detail below.

1.3.1 Fission fragment angular distributions

The fission fragment angular distribution measurements around the coulomb barrier provides rich source of information about the fusion-fission process. From angular distribution studies one can have idea about the shape of the fissioning nuclei at the transition state. It is also possible to have information about the evolution of the composite system formed during the interaction of two heavy nuclei as it relaxes in energy, angular momentum, mass and shape degrees of freedom and ultimately it reaches to fully equilibrium compound nuclear phase. It is sensitive to the entrance channel dynamics of the nuclear reaction process. The failure of statistical model to reproduce the experimental data has been interpreted as the signature of non compound nucleus (NCN) fission. The distribution of K is used to differentiate between the CN and NCN fission.

1.3.2 Fission fragment mass angle correlations

The fission fragment mass and energy distributions also gives valuable information about the fusion-fission reaction dynamics. The mass angle correlations and mass ratio distributions provide information about the occurrence of fission after complete equilibration or partial equilibration of the fissioning nucleus. For compound nuclear fission at excitation energies above 50 MeV, the mass ratio distributions will be centered around 0.5 and mass ratio distributions is normally single peaked in Gaussian shape representing the symmetric fission of the compound system. Further the variance of mass distribution studied at sub and near barrier energies gives important information about the reaction dynamics. If there is any component of non-compound nucleus fission present in the reaction experimental mass distributions will have wings or additional gaussians due to mass asymmetric fission.

1.3.3 Evaporation residue measurements

Highly viscous nature of the fission process can also be observed by measuring the evaporation residue (ER). These measurements give information about fusion-fission dynamics in the pre-saddle region. By comparing the measured ER cross sections with statistical model predictions one can say about the reaction dynamics that fission is taking place through compound nuclear phase or not. However, if fission is dominating there will be a reduction in the ER cross sections. The damped motion of the fission process will be reflected in the enhanced yield of evaporation residue cross section as compared to statistical model predictions. There are several ER measurements in literature showing fission hindrance.

1.3.4 Charged particle measurements

Since charged particles are emitted continously at compound nuclear formation, presaddle, saddle to scission, scission and fission fragment acceleration stages, the charged particle detection can be used to understand the dynamics of the fusion-fission process. It also provides answers to the diffusion process of the viscous nuclear fluid as it undergoes to fission. It is also possible to estimate the time scales of fusion-fission process from the charged particle detection. The contribution of different particles at different stages are expected to have their own significant characteristics, which depends on the reaction dynamics and one can measure the relative contributions at every stage by suitable choice of entrance channel and compound nuclear parameters.

1.3.5 GDR γ rays

One can infer the fusion-fission reaction dynamics by measuring the giant dipole γ rays. The experimentally obtained GDR γ strengths are compared with statistical model calculations by including the nuclear dissipation strengths. It is found that the nuclear dissipation widths depends on the temperature of the fissioning nucleus and the target projectile combinations. It is also found that different dissipation strengths are required to reproduce the experimental data inside and outside the saddle points. We can also extract nuclear fission time scales by measuring the GDR γ rays.

1.4 Motivation of the thesis

Although considerable progress has been made during last eight decades, the fission dynamics is not yet fully understood. To optimize the exploration of the superheavy element landscape, it is important to find out the competition between non-compound and compound nuclear fission. At sub-barrier energies, the deformation and orientation of the heavy reaction partner in the quasifission reactions play an important role [36]. It is still debatable how the entrance channel parameters, particularly, mass asymmetry of the colliding heavy nuclei influence the QF process. In order to study the entrance channel effects on fission dynamics further investigations are required to understand the role of QF process in fission fragment mass distribution.

There are several measurements on mass distributions for fission fragments in different target-projectile combinations, showing anomalous behaviour at near and sub-barrier energies [9, 36, 56]. In earlier experimental studies with ^{19}F on ^{209}Bi show anomalous peak-like structure in mass distribution, but there is no anomalous behaviour with ^{16}O projectile [50, 52]. To understand the role of the entrance channel on fission fragment mass distribution, we have measured the fission fragment mass distribution for the ^{28}Si + ^{197}Au system by populating the same compound nuclear mass (A_{CN} = 225) as in the case of the ^{16}O + ^{209}Bi reaction. In order to investigate the role of weakly bound nucleus on fission fragment, we have carried out another experiment to study the fission fragment mass distribution for ^{9}Be + ^{232}Th,^{209}Bi reactions.

System studied	V_B (MeV)	Z_pZ_t	α	α_{BG}	χ_{CN}
^{28}Si + ^{197}Au	144.5	1106	0.751	0.874	0.798
^{9}Be + ^{232}Th	43.87	360	0.925	0.869	0.788
^{9}Be + ^{209}Bi	41.38	332	0.917	0.842	0.736

Table 1.1: Table of parameters for the present studied systems.

Table 1.1 summarises the parameters of the reactions studied in the present thesis work. In case of ^{28}Si + ^{197}Au reaction, the projectile is stable and oblate deformed. Moreover, the system has entrance channel mass asymmetry less than the critical Businaro Gallone mass asymmetry, which means that the mass will flow from target nucleus to projectile nucleus. In this reaction, we expect to see negligibly small transfer induced fission cross section as the fission barrier of the target is relatively high. On the other extreme, in ^{9}Be + ^{232}Th and ^{9}Be + ^{209}Bi systems, the the projectile is weakly bound and prolate deformed. In these systems, the entrance channel mass asymmetry is larger than the critical Businaro Gallone mass asymmetry, which implies that mass will flow from projectile to target nucleus. As the fission barrier is low for ^{232}Th as compared to ^{209}Bi, we expect to see the consequences of weakly bound projectile such as transfer induced fission reaction, incomplete fusion fission, breakup of projectile and capture of breakup fragment followed by fission etc. In ^{9}Be + ^{209}Bi system, the complete fusion fission is expected with symmetric mass distribution at the energies studied in the present work.

To study the fission fragment mass distribution employing double velocity method, it is very crucial to use two fast timing detectors for the coincidence time of flight (TOF) measurement of the correlated fission fragments. For this purpose we have developed two Multi-wire Proportional Counter (MWPC) detectors and their performance characteristics has been studied using fission fragments from ^{252}Cf source. The details of the development of the MWPC detectors, experimental methods, data analysis and theoretical interpretations are presented in this thesis work.

1.5 Structure of the thesis

The thesis has been grouped into six chapters. Chapter 1, gives the brief introduction about the heavy ion induced reaction processes, related to different kinds of fission mechanisms for projectile energies around the Coulomb barrier. The details of the accelerator/detector facilities that were used in the experimental work of the present thesis is described in Chapter 2. Mainly three different types of detectors viz., silicon detector, BaF_2 and large area 2-dimensional MWPCs were used in the experimental work of the present thesis work, which are described in next chapter.

Two large area position sensitive MWPCs have been indigenously developed for the detection of Fission Fragments (FFs). The detectors were characterized using FFs from ^{252}Cf source to obtain position information by employing delay-line read out method. The velocity distribution of the FFs produced from spontaneous fission of ^{252}Cf has been measured employing a time-of-flight (TOF) technique, using a barium fluoride (BaF_2) as start and a MWPC as stop detector [53]. The energy dependence of fragment velocity distribution was also studied after degrading the fragments by using Mylar foils. It is observed that the width of the distribution for the heavy fission fragments decreases with the reduction in the energies, but for light fragments it does not show any significant dependence on the energy. The above measurements are described in chapter 3.

Fission fragment mass distribution has been measured in ^{28}Si+^{197}Au reaction at bombarding energies 135.4 to 180 MeV [54]. Both the projectile (^{28}Si) and the target (^{197}Au) are oblate deformed. The mass asymmetry of the ^{28}Si+^{197}Au is less than the Businaro Gallone Critical mass asymmetry. The Z_PZ_T of the system is 1106. As the target is not fissile, the transfer induced fission is not expected to be significant in this system. This system provides an opportunity to look in to the presence/absence of quasi-fission at low Coulomb factor Z_PZ_T. For the same mass number composite system formed in reaction ^{16}O + ^{209}Bi, the quasi-fission was found to be absent [52]. The experimental variance of the mass distribution for the present system shows a sudden change from monotonic decrease to a saturation at energies close to the Coulomb barrier (E_{lab}=144 MeV) and again a decreasing trend at sub-barrier energies. The variance of the mass distribution was also obtained from dynamical and statistical model calculations for the fission of a fully equilibrated compound nucleus. Both of the theoretical calculations show a monotonic change of the mass variance around the Coulomb barrier. The anomalous dependence of fission fragment mass width at energies around the barrier, may be due to the dominance of quasi-fission process as compared to compound nuclear fission.

In another experiment, we have studied the role of projectile breakup in fission fragment mass distribution in case of ^{9}Be + ^{232}Th, ^{209}Bi reactions for beam energies near the Coulomb barrier. The experimental setup is similar to that used for ^{28}Si+^{197}Au reaction. The ^{9}Be projectile is a weakly-bound, with breakup thresholds as follows:1.67 MeV for breakup into ^{8}Be +^{1}n and 2.55 MeV for breakup into ^{5}He + ^{4}He. The mass distribution obtained for ^{9}Be + ^{232}Th is found to be asymmetric. The peak-to-valley (P:V) ratio shows an increasing behaviour with decreasing energies. This mass distribution was obtained for total fission events. The experimental details and data analysis are given in Chapter 4.

The results and their theoretical explanation have been presented in Chapter 5.

The summary, conclusion and future outlook is discussed in chapter 6.

Chapter 2

Accelerators and detectors for the experimental work

2.1 Introduction

The detectors and associated electronics, target, projectile beam, and scattering chambers and associated vacuum pumps are used in many nuclear physics experiment. The kind of detector to be used depends on the type of particle, its energy and its mean free path with in the material of detector. The associated electronics for the detector depends on detector properties like its rise time, its energy resolution, and its signal to noise ratio. For nuclear experiments using heavy-ion beam different types of accelerators are used to obtain beams of the required energy.

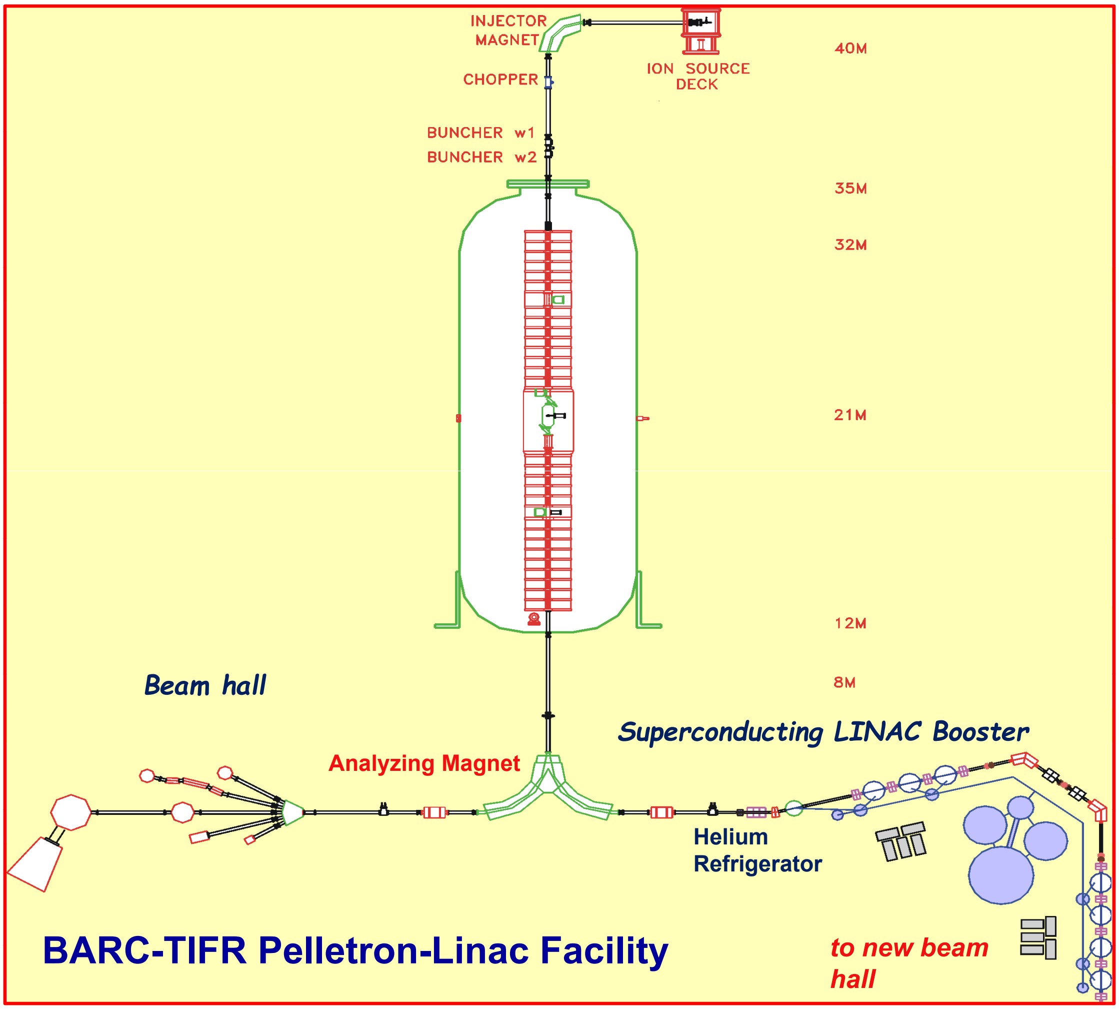

Figure 2.1: Schematic drawing of the BARC-TIFR Pelletron accelerator facility.

2.1.1 Accelerator facility

2.1.1.1 The pelletron accelerator

Fig. 2.1 shows the schematic diagram of the 14UD BARC-TIFR pelletron accelerator facility at TIFR, Mumbai. The ion source named 'SNICS' (Source of negative ions by Cesium Sputtering), situated at the top of the accelerator tower generates negative ions which are initially accelerated to low energies (150-250 keV) in short horizontal section. These low energy negative ions are then mass analyzed using a 90 degree magnet (injector magnet) before entry into the vertical accelerator column. These injected ions get accelerated towards the positively charged high voltage terminal situated in the middle.

Due to this acceleration, singly charged ions gains an energy of V_T MeV, where V_T is the terminal voltage in MV (million volts). This high electric potential at the terminal is achieved by means of the chain of steel pellets separated by insulators and hence the name Pelletron accelerator. This method leads to more uniform charging compared to moving charging belt and hence less ripple on the HV terminal. Inside the terminal, the ions pass through a thin carbon foil (~5 μg/cm^2) or a small volume of a gas, where they are stripped of several electrons resulting in distribution of positively charged ions. This distribution depends on the type and velocity of the ions. These positively charged ions at the terminal are repelled by the positive voltage at the terminal and are therefore accelerated to the ground potential. This results in a energy gain of qV_T MeV for a ion with charge q. Thus, the total energy gain of the ions becomes;

$$E = (q + 1) * V_T \ MeV \tag{2.1}$$

At the end of the accelerating tube, an analyzing magnet is placed which serves the purpose of charge and energy selection of the ion. The energy of the analyzed ions of mass number A and charge state q in this accelerator is given by the relation.

$$\mathrm{B} = 720.76\frac{\sqrt{\mathrm{AE}}}{\mathrm{q}}. \tag{2.2}$$

Where B is the magnetic field in Gauss and E is the energy in MeV. This analyzed beam of ions is then transported to the experimental setup with the help of a switching magnet. The beam is further accelerated to higher energies by using the superconducting linac booster comprised of eight modules (each module accomodates four resonators).

There are four beam lines in the accelerator facility for utilization of the pelletron beam as listed below:-

1. 30° North, used for irradiation of nuclear targets and other samples for radiochemical, material and biological studies. Also used for AMS measurements.

2. 15° North, used for gamma-ray, neutron and charged particle spectra measurements.

3. 0°, consists of a general purpose scattering chamber (used to measure cross-sections and angular distributions for various nuclear reactions). This is further extended to house one small scattering chamber with a large position sensitive deep ionization chamber(used for fission study).

4. 30° South, used for gamma-ray, charge particle and atomic physics measurements.

   For the LINAC utilization, there are 3 beam lines in hall-1 as listed below:

5. 30° General purpose scattering chamber where the experiments were carried out by mounting the MWPC detectors. This beam line was used for carrying out experiments for the present thesis work.

6. 15° used for irradiation of nuclear targets and other samples for radioachemical, material and biological studies.

7. 45° used for gamma-ray, neutron multiplicity measurements.

   Again, there are 2 beam lines in hall-2 as listed below:

8. 15° Indian National Gamma Array for gamma spectroscopy studies.

9. 45° Dedicated beam line for charged particle detector array comprising of ΔE_{Si-Pad} and E_{CsI} for heavy ion reaction studies from light charged particle measurement.

2.1.2 Types of detectors

2.1.2.1 Gas detectors

Historically gas detectors were the first electrical devices, developed for their use in nuclear physics experiments as radiation detectors. They are economically cheap, simple to operate and cost effective for regular maintenance. These detectors exhibit several advantages over the existing solid state and scintillation detectors in respect of versatility of construction, large area coverage, immunity to radiation damage and less pulse height defect etc. Moreover, the flexibility in changing the detector thickness by varying the gas pressure is very useful to detect different charged particles produced in nuclear reactions. Over last few decades, a variety of gas detectors have been developed at BARC for the detection of various reaction products produced in heavy-ion induced nuclear physics experiments. Fig. 2.2 shows the pulse amplitude as a function of the applied field, displaying

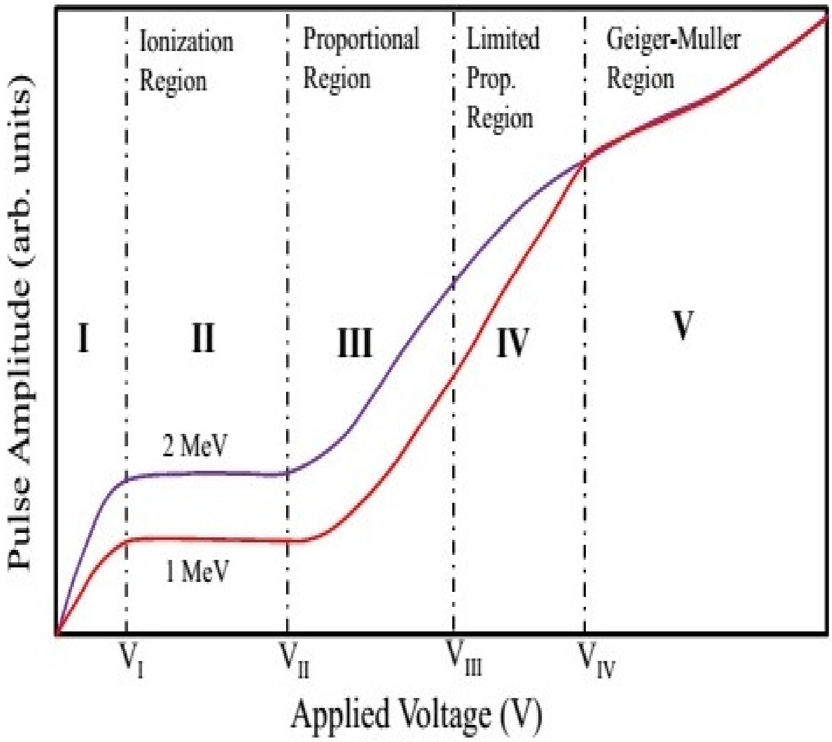

Figure 2.2: The different regions of operation of a pulse mode gas detector. The pulse amplitude is plotted for two different energies of the radiation.

the different regions of the gas detector operation such as, Ionization, Proportional, Limited Proportional, and the Geiger-Mueller (GM) region. The pulse amplitude is plotted for two different energies of the radiaition. For incident radiation of energy 1 MeV, the pulse amplitude in region-I is smaller than that of radiation of energy 2 MeV. This is because greater number of electron ion pairs being created by radiation of 2 MeV energy. Although the recombination of electron ions is similar for both the incident radiations, the number of electron-ion pairs getting separated with the application of field is more for radiation of 2 MeV, so is the pulse amplitude. As the field is increased further, region-II is reached where all electron-ion pairs formed by the radiations are getting separated and recombination reduces to insignificant level. In region-II, the slope of pulse amplitude with electric field is nearly zero. As the field is increased further, region-III is reached where the net ionization is proportional to the primary ionization because of multiplication of initial electron-ion pairs take place with field in this region. Increasing the field still further causes the primary ionization to increase in non linear fashion in region-IV . This is caused by slow movement of positive ions created in secondary ionization towards the cathode. Therefore, each pulse creates a cloud of positive ions, which if sufficiently large can distort the shape of the field within the detector. In this condition, net ionization increases with the field but in non linear fashion. If the field is increased further so that region-V is reached, the space charge created by positive ions become completely dominant in determining the subsequent history of the pulse. Here the same number of final electron-ion pairs are formed irrespective of primary ionization and the pulses formed are of same amplitude at same field values. For this reason the two curves in region-V is having same amplitude irrespective of their energies.

Multi-Wire Proportional Counter (MWPC)

In comparison to the gas ionization chambers, the proportional counters provide fast timing signals and are found to be suitable in the high counting rate experiments. Since the invention of the MWPC by Charpak *et al.*, these detectors are extensively used in high energy physics experiments for particle localization [62, 63]. The MWPC detector has very good timing characteristics and is commonly used for particle tracking and velocity measurement. Because of the good position resolution and detector efficiency, multi-wire proportional detectors have also been used for nuclear physics experiments in different sizes and geometries [64–67], in particular for studying heavy-ion induced fission reactions. In these experiments, the velocity of the fission fragment is determined by combining accurate measurement of the path length and the TOF measured by using two MWPC detectors [68, 69].

Timing characteristics of the signals from MWPC

For the detection of fission fragments (FFs), we have developed two-dimensional position sensitive MWPC detectors, having an active area of 17.5 cm × 7.0 cm for heavy ion induced fission reaction studies at Pelletron-LINAC facility, Mumbai. The MWPC consists of one anode (A) wire plane, two sense wire planes (X and Y) for position information and two cathode (C) wire planes. The schematic sketch of the cathode, anode, X and Y sense wire planes and their geometric separations are shown in Fig. 2.3. Appropriate Printed Circuit Board (PCB) spacers were introduced between the wire planes for maintaining constant distance between the planes and hence providing uniformity in the applied electric field inside the detector region. The separation between the anode wire plane and X (or Y) planes are 2 mm, while the separation between X (or Y) and the cathode plane is 4.8 mm. The wires were fixed on PCB board of thickness 1.6 mm. The main body of the MWPC is made of aluminum to mount all the wire planes inside it. The mounting arrangement of the wire planes and the electronic connectors inside the detector main body is shown in Fig. 2.4. The anode wire plane is placed between the two cathode planes. Each wire is essentially independent and behaves like a proportional counter. The anode plane consists of gold plated tungsten (Au-W) wires having 10 μm diameter and the separation between two adjacent wires is 2 mm. Both the cathode, X and Y sense wire planes were made of Au-W wires having 50 μm diameter and fixed at a separation of 2 mm. The orientation of the X and Y sense wire planes is orthogonal to each other. Stretched Mylar foil of thickness ~ 1 μm and of size 17.5 cm × 7.0 cm was used as entrance window of the detector. The window foil was supported by stainless steel wires of diameter 0.5 mm by fixing on a PCB frame at a separation of 10 mm in both X as well as Y directions. Two gas feed-throughs were connected to the detector for operating the MWPC in gas-flow mode. The flow of the gas was maintained at a constant low pressure (2-3 Torr) by using an automatically controlled gas-flow system supplied by M/s Alpha Pneumatics, Thane, India.

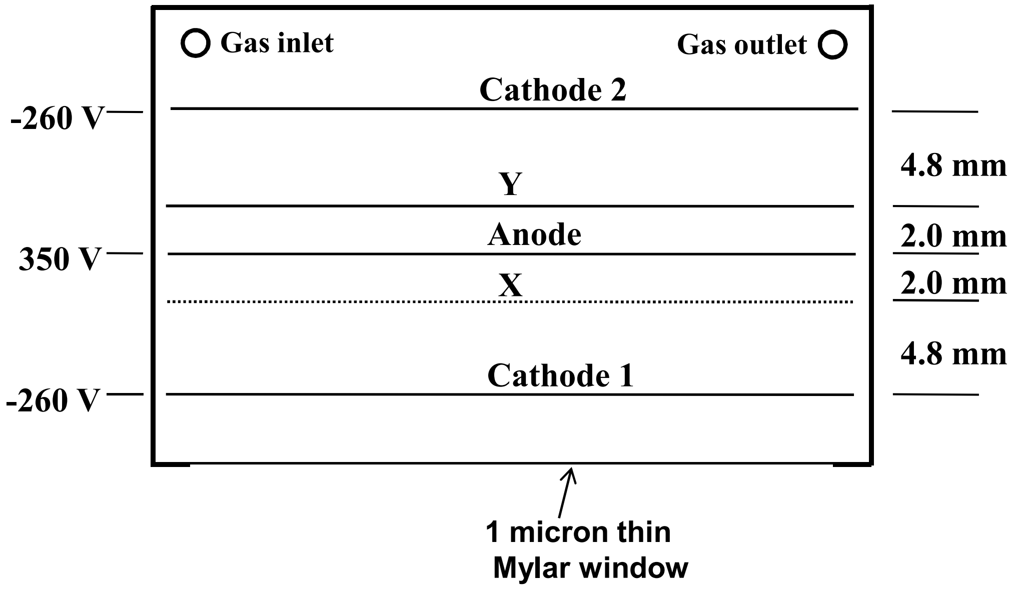

Figure 2.3: Schematic drawing of the vertical cross-sectional view of MWPC showing 5 wire planes. The separation and typical voltages applied to the cathodes and anode are also shown in the figure.

The X-sense wire plane has 100 wires with a pitch of 2 mm, while 40 wires of 2 mm pitch are used for Y-sense wires. We have employed the delay-line read out method for deriving X and Y position information of the detector. The delay between the successive X-sense wires is 2 ns, while that between the Y-sense wire is 5 ns. Using the anode signal as a “Start” and X-signal as “Stop”, the time difference between these two signals gives the X-position of the detector. Similarly, the time difference between the anode and Y-signal defines the Y-position.

The detector was tested in the laboratory with ^{252}Cf source for the uniformity of the position readouts, and also for checking correlation between the timing of anode pulse and position (X,Y) delay-line signals. The anode and the cathode wire planes were biased at +350 V and -260 V respectively, whereas the X and Y sense wire planes were not given any bias voltage and grounded through delay-lines. The MWPC detector has been operated with isobutene gas at a pressure of 3 Torr. The E/p ratio, where E is the electric field between the cathode and anode wire planes, and p is the gas pressure, was high enough (~ 300 V cm^{-1} Torr^{-1}) to produce secondary multiplication of the primary electrons produced in the region between the cathodes and the sense wires. The secondary electrons

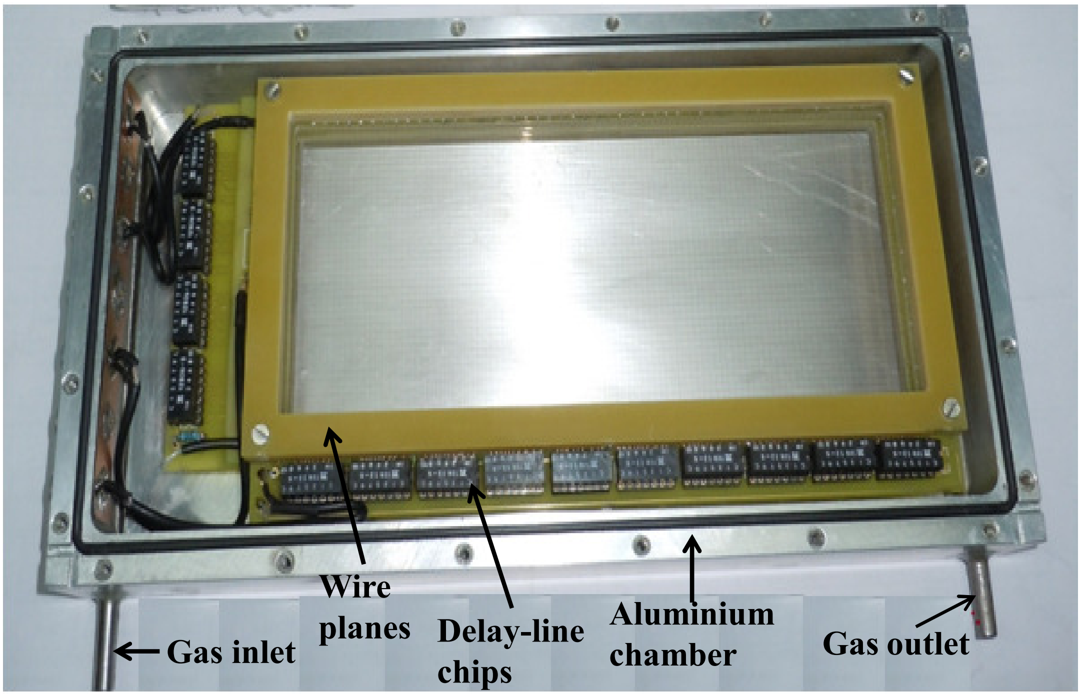

Figure 2.4: Photograph showing mounting arrangement of the anode, 2 cathodes, X and Y sense wire planes of the MWPC inside an aluminum chamber. The delay-line chips (10 in X and 4 in Y) are also shown in the figure.

enter the region between the sense wires and the anode. Due to the large electric field near the anode wires, it causes a localized avalanche of electrons and ions in the vicinity of the anode, which produces a fast rising negative pulse at the anode and positive signals at the sense wires. A wide band ORTEC VT120A type fast timing pre-amplifier (Fast PA) was used to amplify the negative anode pulses. The X and Y sense wire signals have positive polarity and were amplified by two ORTEC VT120B type fast timing pre-amplifiers. We have measured the rise time of the signals with and without the timing filter amplifiers (TFA) as shown in Fig. 2.5 (a) and (b) respectively. The rise time of the anode, X and Y signals were ~ 6 ns immediately after the fast amplifier and it is about ~ 9 ns after the TFA, using suitable integration and differentiation time of about 10-20 ns.

Typical anode pulses from VT120A pre-amplifier with ^{252}Cf source were 500 mV for FFs and less than 5 mV for alpha particles. Since the anode signal is primarily used for the timing measurement of fission fragments, its output from fast pre-amplifier is directly fed to Constant Fraction Discriminator (CFD) for further processing. The timing outputs

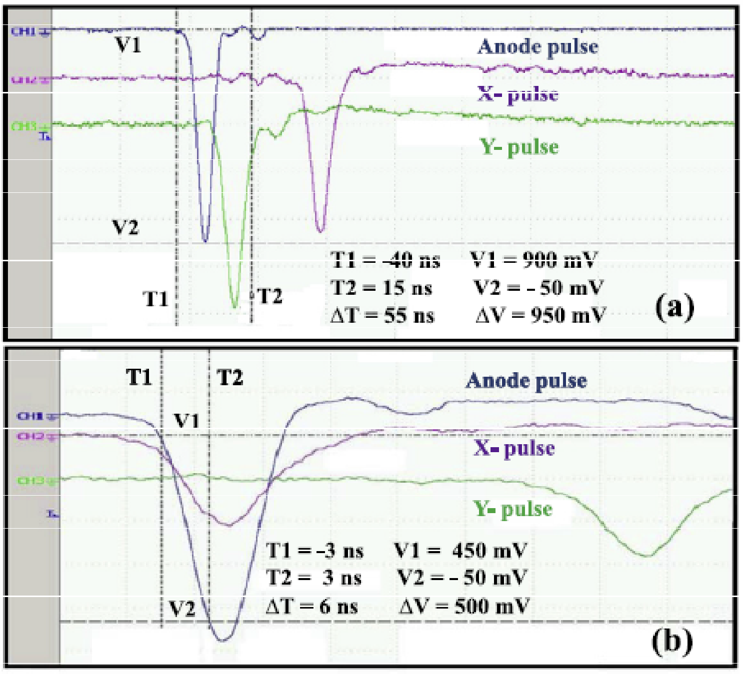

Figure 2.5: (a) The pulses taken by a digital oscilloscope from the fast pre-amplifier of the anode, X and Y planes after shaping with suitable integration and differentiation using TFA. (b) Pulse shapes of the signals immediately after the fast pre-amplifier (without using TFA).

of the sense wire signals (X and Y) were about 150 mV, which were filtered through timing filter amplifiers (TFAs) and fed to CFD. After the TFA, the pulse height of the signals were about 950 mV. The output signal of the anode CFD becomes the "Start" pulse for two Time-to-Amplitude Converters (TACs) that are used for X and Y position measurements. It was also used for generating master gate pulse through a Gate & Delay Generator (GDG). The output of the CFDs of the X and Y sense wires are suitably delayed and used as "Stop" pulses for obtaining position information from the corresponding TAC modules. The output pulse heights of both the TAC's are proportional to the delay between the anode and sense wire signals, which translate the position information of the detector in two dimensions.

The linearity of the position signal has been checked by putting a mask on the face of the detector. There were 11 holes in X direction of the mask with 1.0 mm diameter

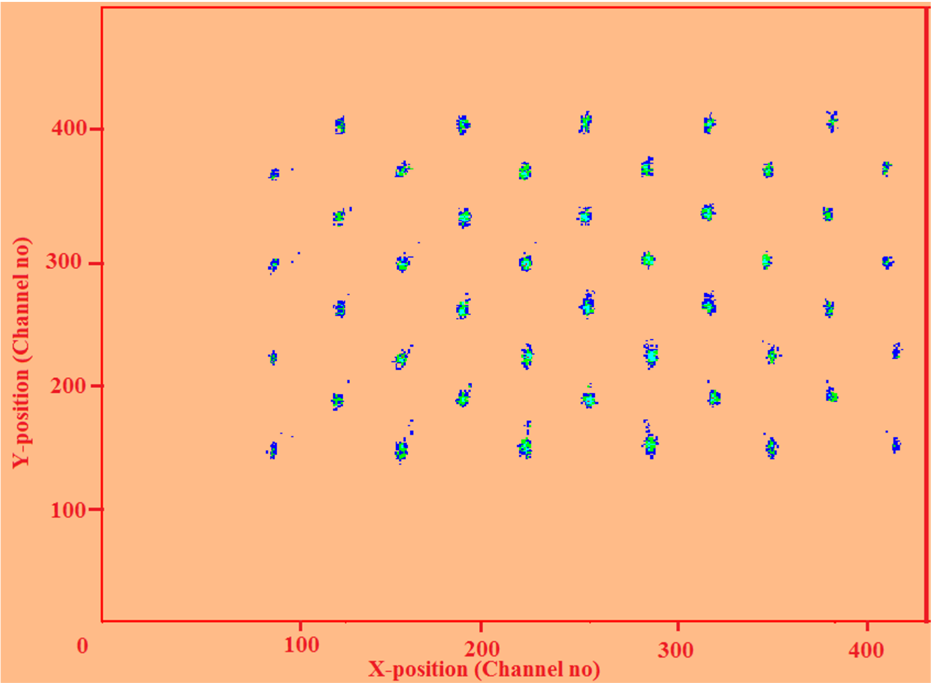

Figure 2.6: Two dimensional spectrum of coordinates X and Y obtained by keeping a mask with row of 8 holes of 1 mm diameter and column of 11 holes of 1 mm diameter placed in front of the detector. The holes in row were separated by 5 mm and the holes in column were separated by 10 mm.

and the separation between the center of the two adjacent holes was 10 mm. In the Y-direction 8 holes of 1.0 mm diameter, with a separation of 5 mm were used. The image of 2D Mask as produced by MWPC is shown in fig 2.6. The peaks corresponding to X and Y directions are obtained by taking the projection on the axes of 2D image (fig 2.6) corresponding to all columns and rows is shown in Fig. 2.7 (a) and (b) respectively. The mean peak position and width have been obtained by fitting the distribution with a Gaussian function. The peak channel number corresponding to the center of each opening hole, has been plotted as a function of hole position (in mm), also shown in the same figure (right Y-axis). The error in the Gaussian fitting of the intensity profile and hence in the position measurement is within the size of the circle. It is observed that the position peak channels show linear behavior with the peak position. The position resolution (FWHM) both in X and Y directions are obtained from the fitting of the peaks and are found to be about 1.04 ± 0.03 mm and 1.06 ± 0.04 mm respectively.

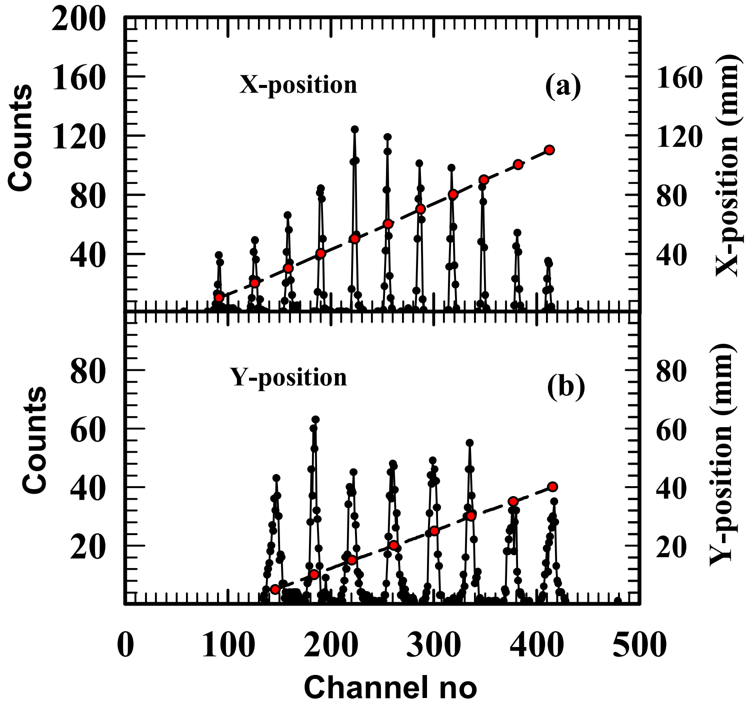

Figure 2.7: (a) Position spectrum in X direction as obtained by keeping a mask in front of the detector, having 11 holes of 1 mm diameter and separated by 10 mm. (b) In Y-direction, the position spectrum for 8 holes of 1 mm diameter in the mask and separated by 5 mm.

The position sensitivity of the detector in two dimensions has also been tested with FFs from a ^{252}Cf fission source and by putting a mask of “BARC" (acronym of Bhabha Atomic Research Centre) in front of the detector. Each letter of the mask “BARC" was realized in a dot matrix format by drilling small holes of 1.0 mm diameter. The center to center distance of the holes for straight portion of each letter is 5 mm and for the curved portions it is 2.5 mm. The 2D position spectrum as shown in Fig. 2.8, gives a clear image of the acronym “BARC", demonstrating very good performance of the detector for position measurement in two dimensions.

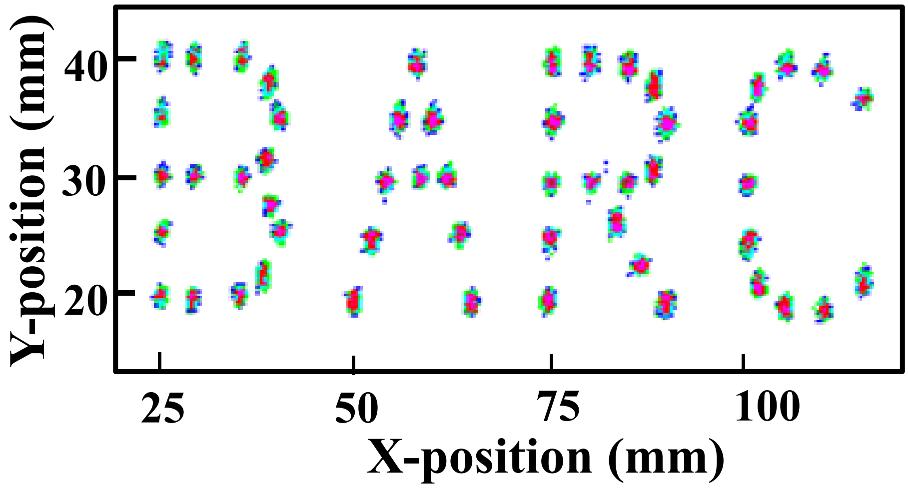

Figure 2.8: Two dimensional spectrum of coordinates X and Y obtained by keeping a mask with acronym “BARC" having 1 mm diameter holes placed in front of the detector.

2.1.2.2 Scintillator detectors

The scintillation detector is undoubtedly one of the most often and widely used radiation detection devices in nuclear and particle physics today. It makes use of the fact that certain materials when struck by a nuclear particle or radiation emit a small flash of light, i.e. scintillation. When coupled to an amplifying device such as photomultiplier, these scintillations can be converted into electrical pulses which then can be analyzed and counted electrically to give information concerning the incident radiation. Scintillation materials produce three different types of emission.

- The prompt emission of visible radiation from a substance following its excitation by some means is fluorescence.
- Phosphorescence is again normally within the visible spectrum but has a longer wavelength and characteristic decay time.
- Delayed fluorescence as the name implies, results in emissions much like fluorescence but with a longer characteristic decay time.

For a material to be considered a good scintillator it must convert a large fraction of incident radiation into prompt fluorescence. In a scintillation detector the photons emitted by the scintillation crystals have to be converted into an electrical pulse for counting. This is done by means of a photomultiplier tube. The emitted photon pulses are weak and are directed from the crystal to the photocathode of the PMT by means of a light guide or optical window. Once the pulse reaches the photocathode a proportional number of electrons are emitted. The emitted electron pulse is then amplified by a series of dynodes within the tube. Therefore, for each electron emitted at the photocathode, 10^6 – 10^8 electrons arrive at the anode located at the tubes base. The PMT is comprised of two components. The first is the photocathode, which is a layer of photosensitive material that will emit electrons when exposed to the optical pulses from the scintillation crystal. The second is an arrangement of positively charged dynodes required to increase the number of electrons in the pulse produced by the photocathode. This is necessary as the initial pulse of electrons is fairly small and cannot easily be measured. The size of pulse received at the anode is typically about 10^{10} electrons.

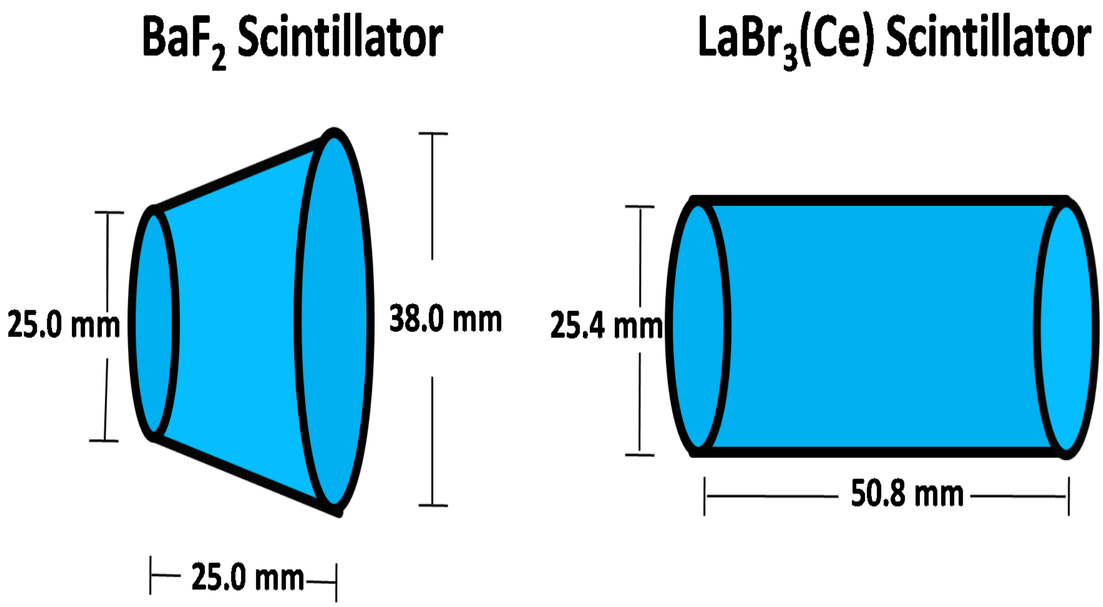

Figure 2.9: The BaF_2 and $LaBr_3(Ce)$ crystals.

1. **Barium Fluoride (BaF_2)**

Barium fluoride has the distinction of being the first inorganic crystal discovered to have a very fast component in its scintillation decay. It is the only presently known scintillator with high atomic number with scintillation components that has a decay time of less than 1 ns. This combination of properties therefore makes the material attractive for scintillation detectors in which both high detection efficiency per unit volume and a fast response are required. Unactivated BaF_2 has been known as a scintillation material since the early 1970s. The total light yield in BaF_2 is only about 20% of that observed in NaI(Tl), so the attainable energy resolution is considerably poorer. The light yield in the fast component is quite small, only about 1400 photons per MeV. BaF_2 is not hygroscopic, but condensing moisture can pit its surface. It is relatively radiation hard. Radiation doses of 105 Gray do not cause any severe damage to its scintillation characteristics. In the present experiment, the BaF_2 crystal used is conical in shape. It is 25 mm in length. The tapered side is 25 mm in diameter and the other side is 38 mm in diameter as shown in Fig. 2.9.

Timing characteristics of the BaF_2 detector for γ rays

The BaF_2 detector was of length 25 mm, with conical shape having 25 mm diameter in the front and 38 mm in the back face, which was coupled with a photomultiplier tube. The light output pulse from the de-excitation of BaF_2 has two components: one with decay time of 630 ns and other with decay time of 0.6 ns. The fast component only accounts for 20% of the total light output of BaF_2, the remaining 80% consists of by the slow component [75]. The time resolution of the BaF_2 detector has been obtained by using two identical detectors (as shown in 2.10) and measuring the two coincidence γ rays of energies 1.173 and 1.332 MeV, emitted from a ^{60}Co source. Positive bias voltages (+1700 V) were applied in both the detectors using two independent HV supplies. The γ ray energies were measured after amplifying the signals using a shaping amplifier. The output pulses from the anode of the BaF_2 detectors were found to be sharp in timing having rise time of ~ 3.2 ns and in amplitude around 500 mV. The pulses were directly fed to CFD without

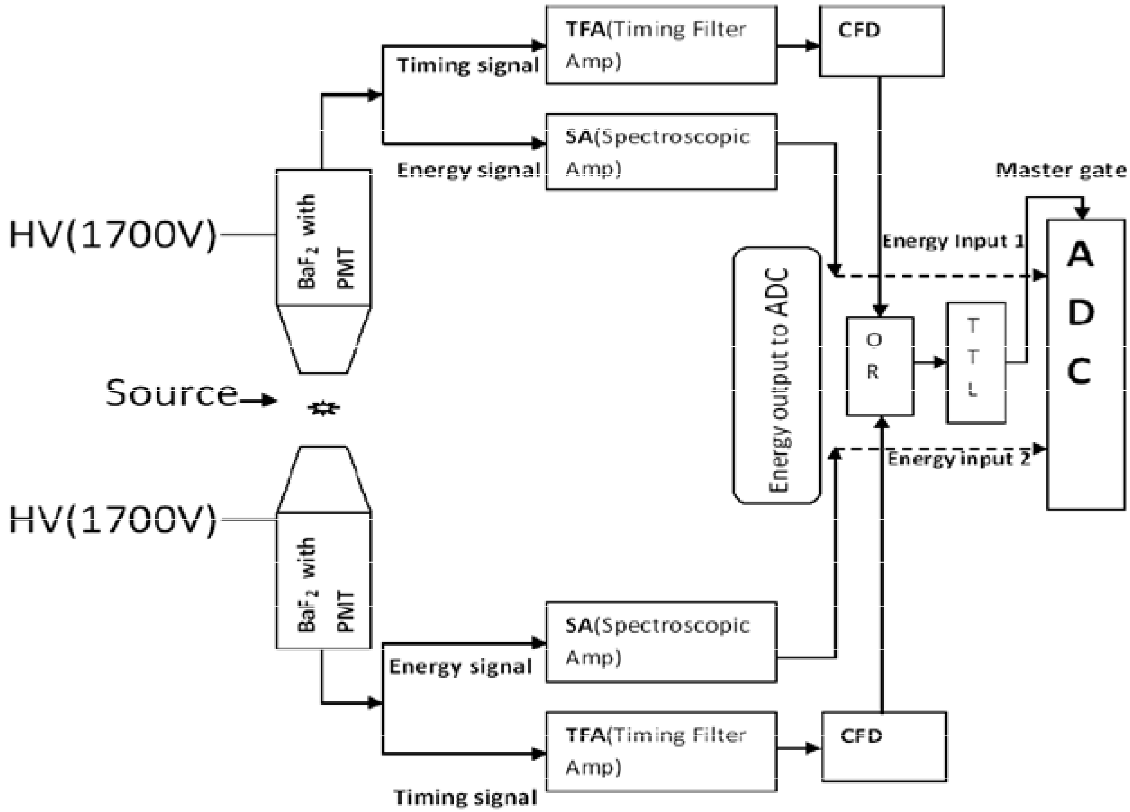

Figure 2.10: Schematic diagram of the experimental setup along with the associated electronics.

any shaping or amplification. The output pulse from the CFD of one BaF_2 was fed to the “Start” of the TAC and the pulse from the CFD of other BaF_2 was delayed through a delay box and eventually given to the “Stop” of the TAC. The time resolution (FWHM) obtained for the BaF_2-BaF_2 detector system from this experiment is about 233 ± 6 ps

2. **Cerium doped Lanthanum Bromide ($LaBr_3$(Ce)**

   Cerium doped Lanthanum Bromide is a better alternative to NaI(Tl). It is denser, more efficient and much faster (having a decay time about ~20 ns). It also offers a superior energy resolution. The improved resolution relative to sodium iodide is due to a higher light yield. Moreover, the light output is very stable and quite high over a very wide range of temperatures, making it particularly attractive for high temperature applications. Depending on the application, the intrinsic activity of

^{138}La can be a disadvantage. $LaBr_3(Ce)$ crystal is very hygroscopic. In the present experiment, the $LaBr_3(Ce)$ crystal used is cylindrical in shape. It is 25.4 mm in diameter and 50.8 mm in length as shown in Fig. 2.9.

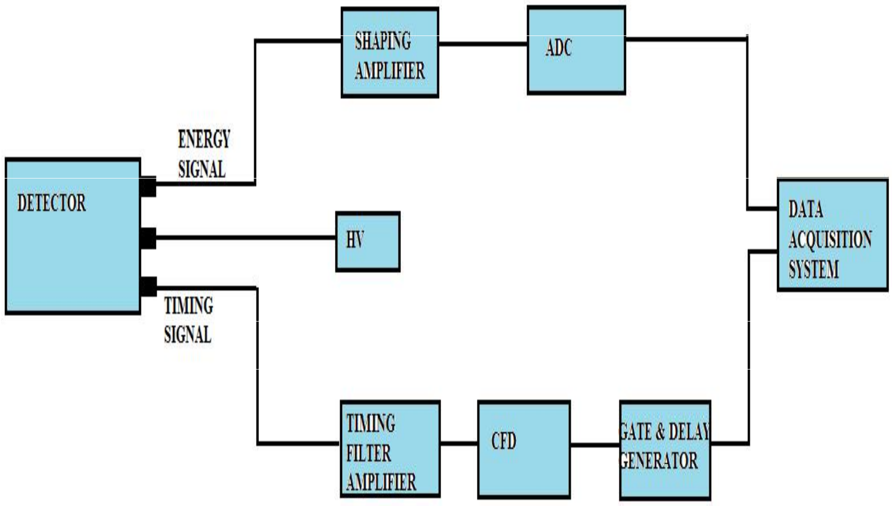

Figure 2.11: Block diagram of the experimenatal set-up.

We carried out an experiment to study the performance characteristics of BaF_2 as well as $LaBr_3(Ce)$ detectors. In this experiment (block diagram as shown in Fig. 2.11), the energy signal from the detector was directly fed to the shaping amplifier (SA) followed by an Analog to Digital Converter (ADC) and then directly to the Data Acquisition System (DAS). Since the PMT output signal is already strong, it does not need a preamplifier (PA). The timing signal was fed to the Timing Filter Amplifier (TFA), followed by the Constant Fraction discriminator (CFD) and then to the Gate and Delay Generator (GDG) which generates the trigger signal for the data acquisition system. The data was collected in the Data Acquisition system and was plotted in ROOT software. The count rate from each detector was obtained for different bias voltages and then looking at the variation, the corresponding operating voltage was obtained. A Gaussian fit was done on the energy peaks and the corresponding parameters (FWHM, peak position etc.) were calculated. Using these parameters, the energy resolution of the detector was calculated for ^{60}Co and ^{137}Cs gamma rays.

Table 2.1: Enumeration of the various parameters obtained for BaF_2 and $LaBr_3(Ce)$ detectors.

Sr. No.	Detector	Operating Voltage (V)	Count Rate (at operating voltage) (s^{-1})	Energy Resolution with ^{137}Cs	Energy Resolution with ^{60}Co	
				662 keV	1.17 MeV	1.33 MeV
1	BaF_2	1450	390	72.03keV (11.32%)	83.44keV (7.43%)	86.86keV (6.77%)
2	$LaBr_3(Ce)$	1900	264	45.70keV (5.10%)	45.89keV (3.34%)	46.06keV (3.01%)

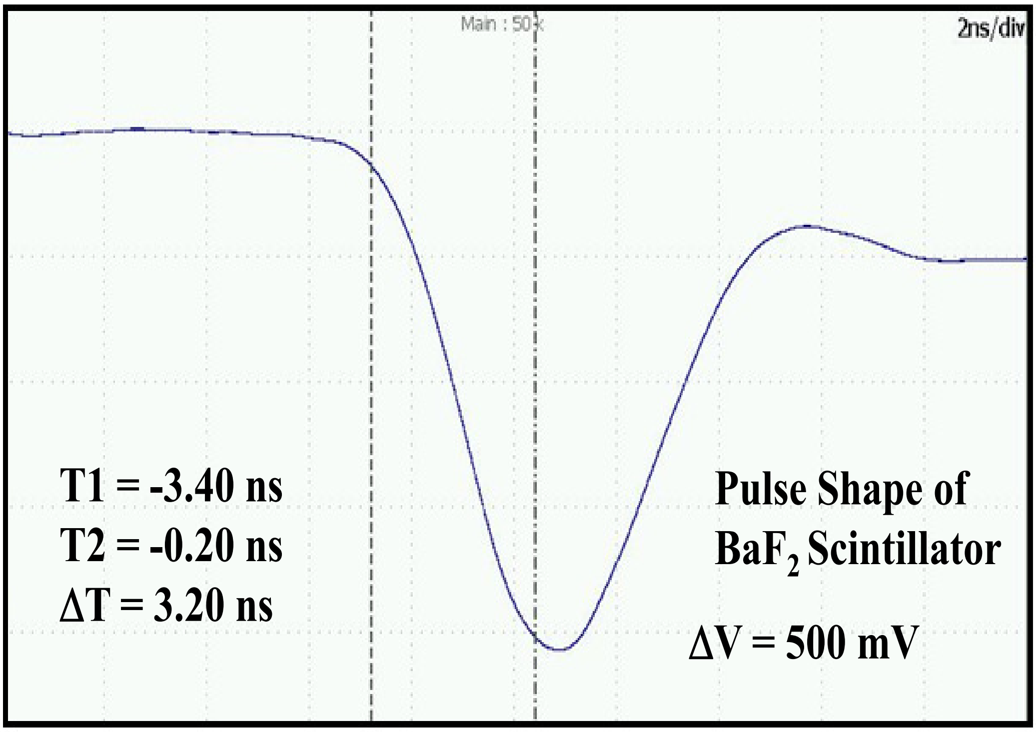

Figure 2.12: The output pulse of BaF_2 scintillator detector showing very small rise time (~ 3 ns).

Conclusion:

The energy spectra for BaF_2 and $LaBr_3(Ce)$ are shown in Fig. 2.14 (a) and (b) respectively. The rise time of BaF_2 detector signal is ~ 3 ns as shown in Fig. 2.12 and it is ~ 8 ns for $LaBr_3(Ce)$ as shown in Fig. 2.13. From the present experimental studies, it is observed

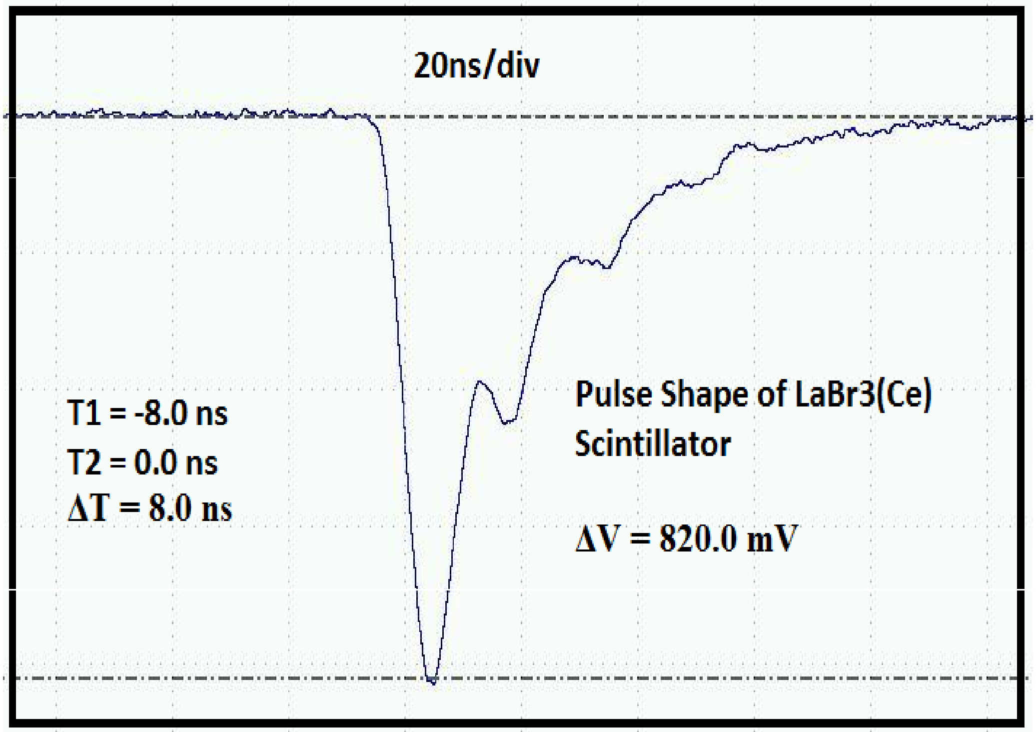

Figure 2.13: The output pulse of $LaBr_3$(Ce) scintillator detector showing very small rise time (~ 8 ns).

that the energy resolution of the BaF_2 is 7-11% and for $LaBr_3$(Ce), it is 3-5%. Thus the energy resolution of the $LaBr_3$(Ce) detector is better than the BaF_2 . However, the BaF_2 Scintillator gives a much faster signal in comparison to $LaBr_3$(Ce), thus BaF_2 Scintillators are more suitable for fast timing experiments.

2.1.2.3 Silicon surface barrier detectors for charged particle detection

For the spectroscopy of charged particles, the semiconductor detectors have been extensively used due to the following advantages:

1. Semiconductors have a very small band gap energy of ($\sim 1eV$). Thus the number of information carriers (electron hole pair) generated by incident radiation are greater than that (electron ion pairs) produced in gas detectors, used for charged particle measurements.

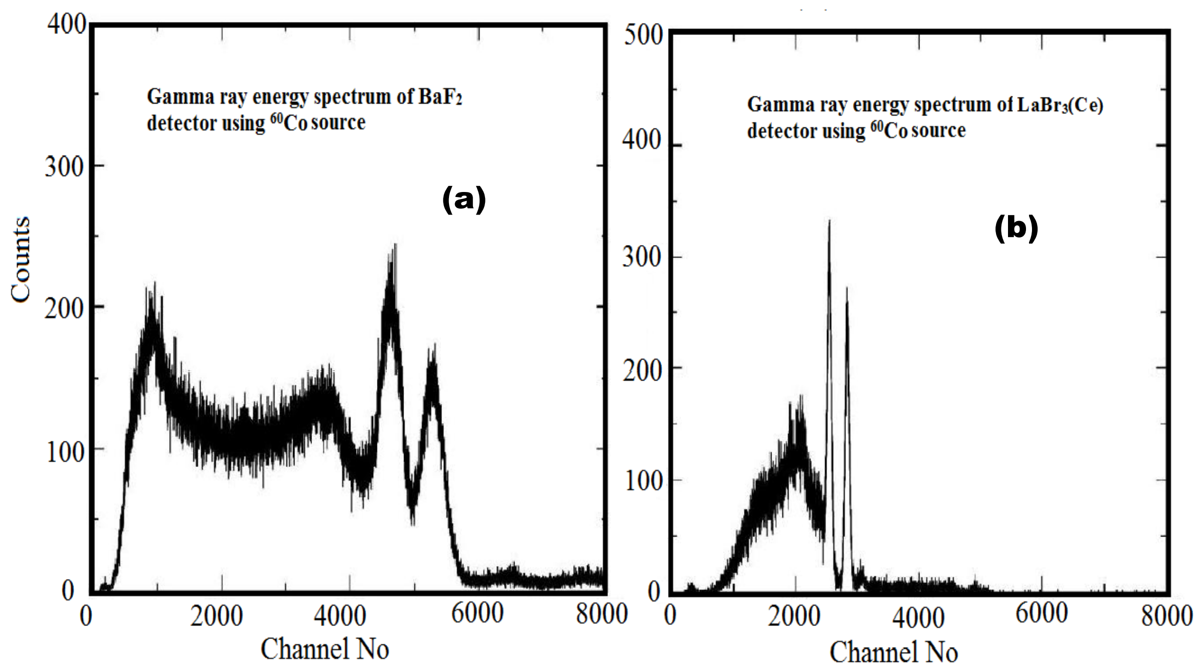

Figure 2.14: The energy spectrum of BaF_2 and $LaBr_3$(Ce) for gamma rays from ^{60}Co source.

2. The time required for the electrons and holes to be collected at the respective terminals is considerably less, due to their high drift velocities, as compared to the time required for the electrons and ions to be collected. This enables the use of semiconductor detectors to give better timing characteristics than ionization chamber and their use in experiments requiring fast timing.

3. Their larger detector material density allow for generation of more electron-hole pairs as opposed to ionization chambers and have greater stopping power.

4. Semiconductor detectors are compact in size.

5. Semiconductor detectors can have variable thickness of (active volume) depletion region based on applied voltage.

The basic working principle of a semiconductor detector is as follows:

These detectors are basically p-n junction diodes, which are operated in the reverse biased condition. This is because, for a reverse biased p-n junction, the depletion region is heavily exhausted of majority charge carriers. Thus, any radiation impinging on the detector will create ionization, generating the electron-hole pairs and thus giving an electrical signal. The amplitude of the signal increases with the energy deposited by the incident particle in the detector, and the time required for collection of such events gives the time information.

For charged particle detection silicon (Si) is the most widely used material due to its slightly higher band gap energy of $\sim$ 1.1 eV as compared to germanium (Ge) having a band gap energy of $\sim$ 0.7 eV. Thus, it can be used even at room temperature. The silicon surface barrier (SSB) detectors are the widely used detectors for charged particle measurements. In these detectors, a p-n junction is formed between a semiconductor and a metal, usually n-type silicon with gold or p-type silicon with aluminum. Due to the different Fermi levels of these materials, a contact emf arises when the two are put together. This leads to lowering of the band levels in the semiconductor region and thus extension of the depletion region entirely into the semiconductor region. Such junctions are also called Schottky barriers and possess many of the characteristics of the p-n junction. These detectors are fabricated at room temperature by first etching the silicon surface and then depositing a thin layer ($\sim$ 40 μg/cm^2) of gold by evaporation. The surface is also allowed to oxidize before the deposition. The junction is then mounted in an insulating ring with metalized surfaces for electrical contacts. SSBs can be fabricated with varying thickness and depletion region. For fully depleted detector, in which the depletion region extends entirely into the thickness of the silicon wafer, serves as a transmission detector for measuring the energy deposition of a passing particle. Increasing the bias of such detectors helps in faster charge collection and thus a fast signal rise time. Commercially available SSB detectors have thickness between a few tens of μm to few mm.

In the present thesis work, we have used silicon surface barrier detectors for beam monitoring and data normalization.

Chapter 3

Measurement of fission fragment velocity distribution using time of flight technique

3.1 Introduction

The velocity distribution measurement of the fission fragments is important in the context of measuring the mass distributions. Fission fragment mass distribution can be measured by employing several methods:

1) From the coincident measurement of kinetic energies of both the fragments ($2E$)

2) Simultaneous measurement of fragment energy and velocity (E-V) or correlated velocity of both the fission fragments ($2V$) [51, 56–58].

In the past silicon detector and gas ionization chambers have been used for fission fragment energy and mass distribution measurements by employing 2E method [50, 55]. In case of semiconductor detectors, the correction for the pulse height defect is required for the energy measurement [59]. Although gas ionization chambers provide stable operation, the corrections due to the energy loss in the entrance window, causes uncertainty in mass measurements [60, 61]. The timing signals from ionization chamber are slow, having rise time $\sim$ 100-200 ns and these detectors are rarely used for TOF measurements using E-V or 2V methods. In addition, these detectors cannot handle high count rates at forward angles in nuclear physics experiments.

The precise measurement of the fragment velocity is very crucial for obtaining the fission fragment mass distribution. The fragment velocity distribution for ^{252}Cf fission, has been measured earlier from the coincident TOF using a pair of detectors having fast timing response [70]. The accuracy of the time intervals of the signals of the detectors separated by a flight distance is important for the velocity measurement and the uncertainty in the time measurement can be minimized by using two detectors having fast timing response. Since the neutron emission is isotropic in the rest frame of fragment, the data analysis in TOF method is much simpler [71]. The effect of neutron emission on the velocity distribution of the fragments will be minimal and, thus, the mass measurement by employing the TOF technique using MWPC is relatively more accurate in compared to the 2E measurement [72]. Various fragment nuclei are produced in nuclear fission having varying velocities/energies. In contrast to light-ions, the enegy loss mechanism in radiation detectors for FFs is a complex process. There is a strong variation of the specific energy loss with the fragment energy or velocity [73].

In the present work, the energy dependence of the width of velocity distribution has been studied for the first time by degrading the fragment's energy using Mylar foils of different thickness. Here, we have used a novel technique for measuring the velocity distribution of fission fragments produced from the spontaneous fission of ^{252}Cf, by employing the TOF method. A BaF_2 scintillator was used for the detection of prompt gamma rays emitted from the fragment nuclei, that was used as the "Start Signal" in the TOF setup. The fast anode signal from MWPC due to the fission fragments was used as "Stop Signal". The timing characteristics of MWPC have been investigated in detail in order to use this detector for the measurement of the velocity of the fission fragments produced in spontaneous fission and heavy-ion induced reactions.

3.2 Experimental details

The TOF measurements were carried out using a BaF_2 scintillator and a MWPC detector. The schematic diagram of the experimental set up is shown in Fig. 3.1. A ^{252}Cf source was mounted on a flange inside a scattering chamber, which was evacuated to a vacuum of $\leq 10^{-3}$ Torr. For the detection of FFs, the MWPC detector was mounted on a platform inside the vacuum chamber at two distances 54.5 cm and 85.5 cm from the source in two different measurements. The BaF_2 detector was mounted outside the flange of the vacuum chamber at a distance of 1.0 cm from the source. In spontaneous fission of ^{252}Cf about 10 prompt γ-rays are also emitted along with the fission fragments [74]. The gamma rays are detected by the BaF_2 detector, which gives a fast signal and was used as "Start Signal" for the TOF experiment. After traveling the flight path in vacuum, the fission fragments reach the MWPC and lose energy in the gaseous medium. It gives a fast timing signal from the anode that was used as "Stop Signal" in the experiment.

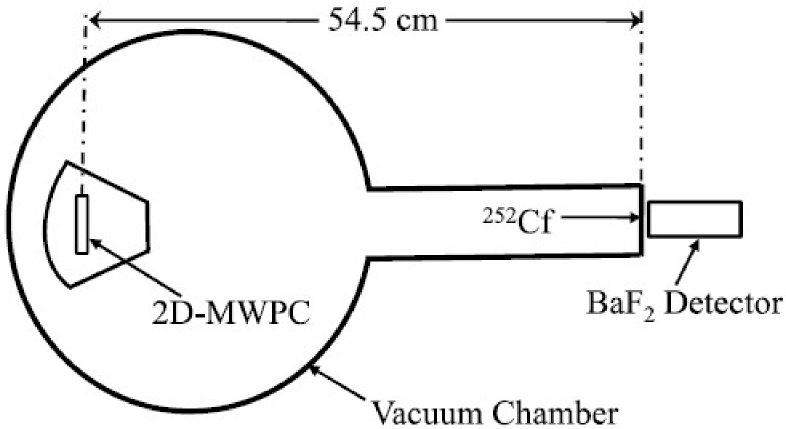

Figure 3.1: Schematic diagram of the experimental TOF setup using a BaF_2 detector and MWPC mounted inside a vacuum chamber.

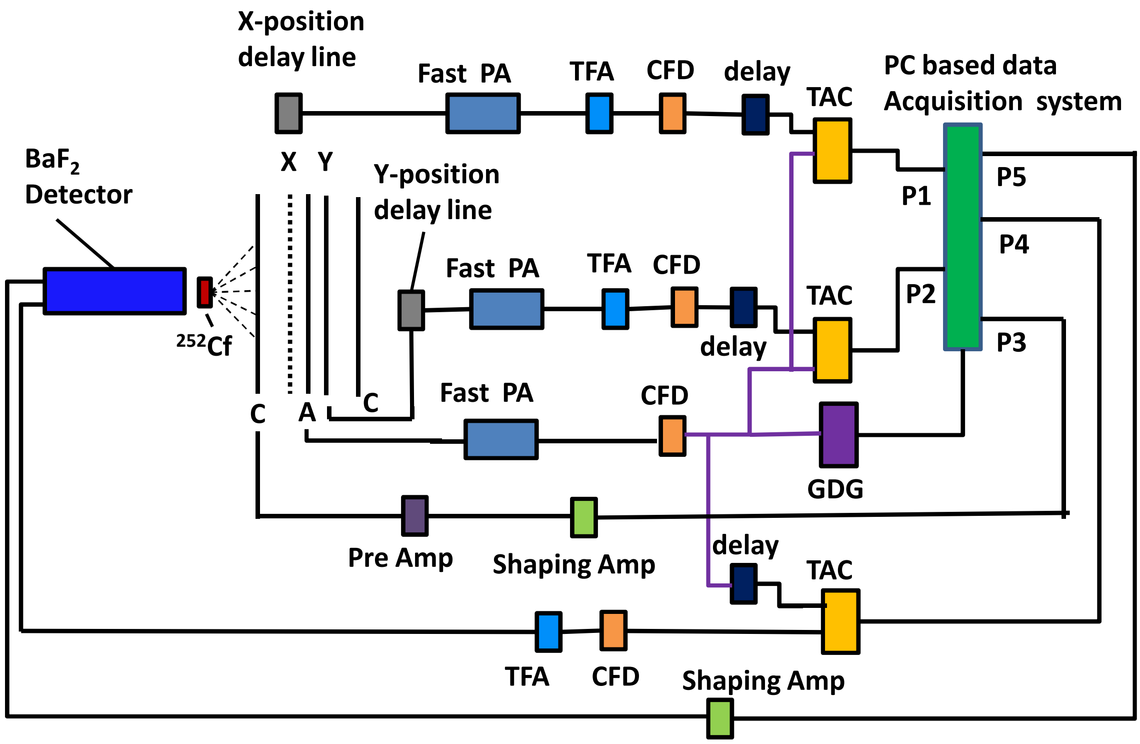

Figure 3.2: Electronic block diagram of the setup used for the TOF measurement.

3.3 Measurement of the velocity distribution for fission fragments from ^{252}Cf

For the velocity distribution measurement, the fission fragments were detected by using the MWPC, mounted at a distance of 54.5 cm from the source. The prompt γ rays emitted from the fission fragments were measured by using a BaF_2 scintillation detector in coincidence with the signals from the MWPC. The TAC spectrum was obtained by using the "Start Signal" from the BaF_2 and "Stop Signal" from the anode of the MWPC detector. The measurement was repeated by extending the flight path to 85.5 cm, using a stainless steel tube of known length of 31 cm. From the known path length and measured TOF, the velocity (V) was obtained after processing the event by event list mode data. The partial energy loss (ΔE) in the MWPC has been measured from one of the cathodes, by amplifying the signal using a charge sensitive preamplifier (PA) followed by a shaping amplifier. Fig. 3.3 shows the 2D-plot of ΔE vs TOF of the fission fragments (without any degrader foil) for the flight path of 54.5 cm. As the light fragments have larger velocities than the heavy fragments, it is seen from the 2D spectrum that the two fission fragment groups are clearly separated. The TOF distribution spectra obtained by taking the x-projection of the 2-dimensional plot, shown in Fig. 3.3. By using double Gaussian fit to the timing spectrum, we have obtained the width of the TOF distribution. It is observed that the time spread for the heavy fragments is larger than the lighter ones due to the velocity dispersion. The velocity distributions obtained from the present measurement for two distances are consistent. The mean centroid of the velocity distributions were obtained by taking the average of the peak velocities measured for both the distances. The centroids for heavy and light fragments are, $V_H = 1.035 \pm 0.003$ and $V_L = 1.378 \pm 0.004$ cm/ns respectively. Here, the errors in V_L and V_H are calculated from the fitted uncertainties in the TOF and assuming the error in flight path measurement to be 0.05 cm.

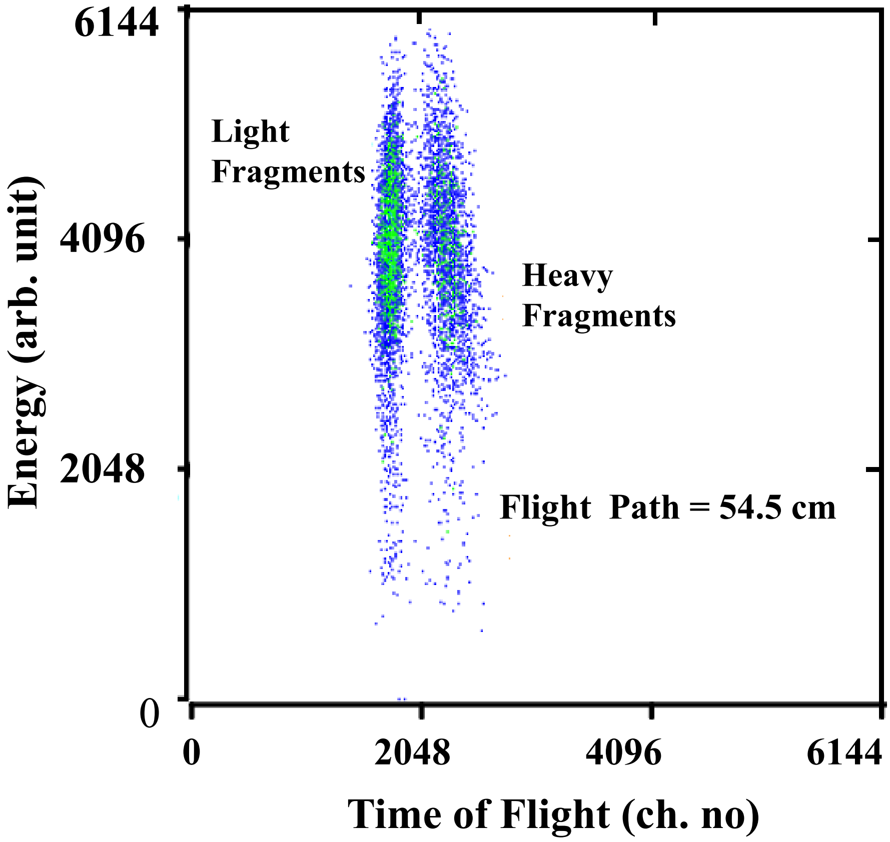

Figure 3.3: Two dimensional plot of Energy (ΔE) vs TOF, showing clear separation for light and heavy fission fragment groups produced from ^{252}Cf.

The energy dependence of the TOF distribution for the light and heavy fragment groups have been measured after degrading the fragment energies by keeping a Mylar foil of thickness 2.5 μm very near to the ^{252}Cf source. Thus the fragments will lose energy in the foil and hence the TOF will increase due to reduction of the fragment velocities. The experiment was repeated for 2, 3 and 4 layers of Mylar foils each of 2.5 μm thick. After each degrader foil, the ΔE spectra (shown in Fig. 3.4) were obtained by putting independent banana gates for both heavy and light fragments in ΔE vs TOF two-dimensional plot (e.g., Fig. 3.3, without any foil) and taking the y-projection. Without any Mylar foil, the energy loss in the gaseous medium due to the heavy and light fragment groups are similar as shown in Fig. 3.4 (a). In case of fission fragments, the specific energy loss is

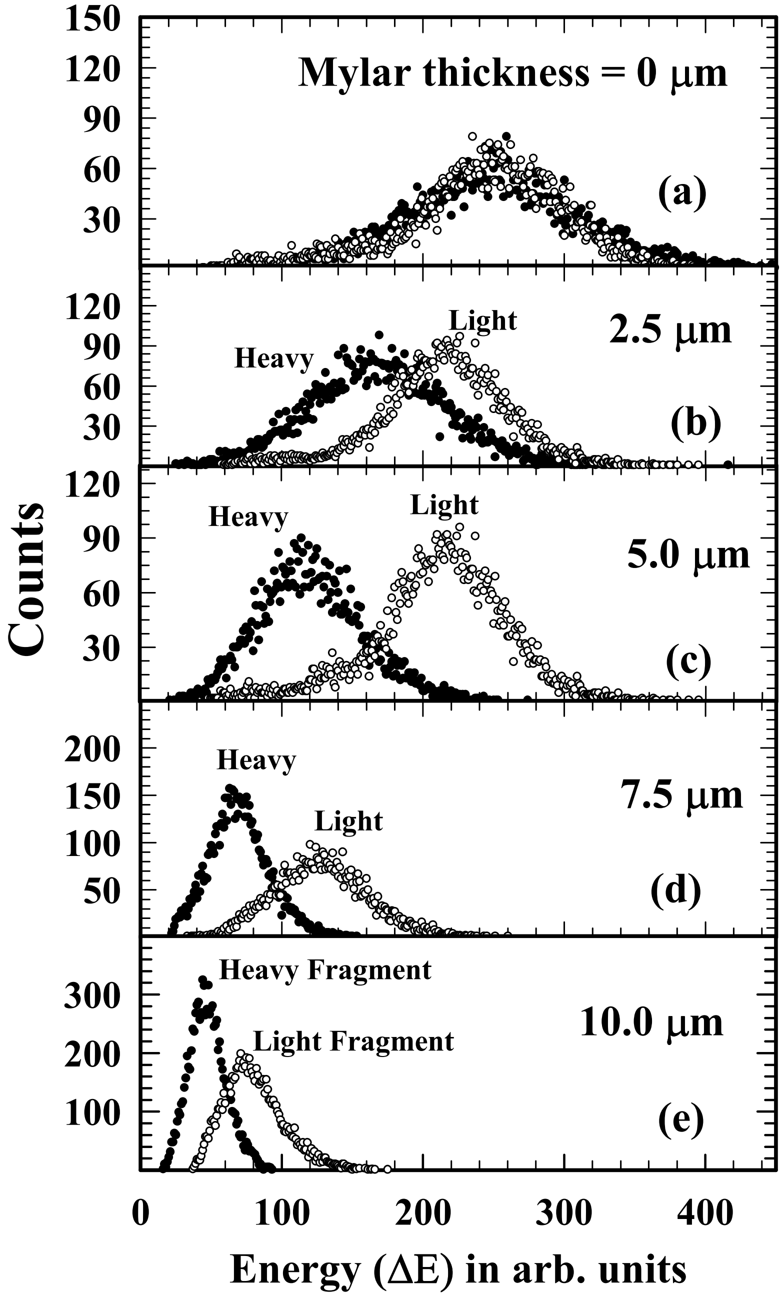

Figure 3.4: The energy (ΔE) spectra in MWPC for the FFs from ^{252}Cf after degradation with different thicknesses of Mylar foils. Each ΔE spectrum is obtained by taking the "Y-projection" of the 2D plot for ΔE vs TOF.

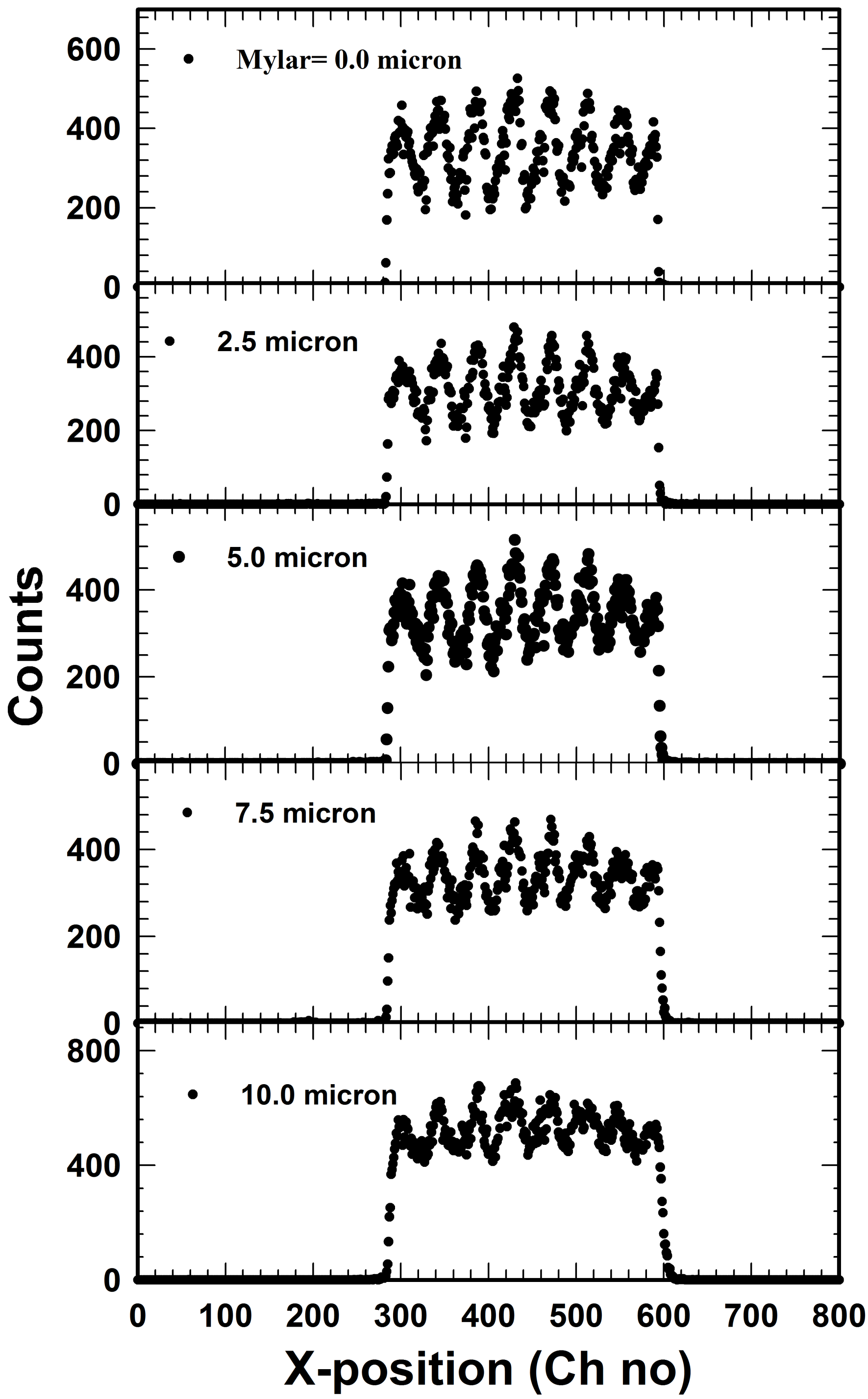

Figure 3.5: X-position spectrum in MWPC for the FFs from ^{252}Cf after degradation with different thicknesses of Mylar foils.

almost equal for both light and heavy fragment groups in the beginning of the range [73]. However, as the fragments pass through the degrader foil, the fragment energy is reduced and hence the energy loss in the detector is also reduced. Thus, the lighter fragments having higher energies will lose more energy in the gaseous medium as compared to the heavier fragments. The specific energy loss of fission fragments depend on the Bragg curve and the energy loss behavior have been discussed in [53]. It is seen from Fig. 3.4 that for heavy fragment group, the width of the ΔE spectrum reduces significantly after passing through the foil as compared to the light fragments. It is also observed that the energy spectra are better separated for the two fragment groups after energy degradation of the fragments passing through Mylar foils of thickness 5 μm, as shown in Fig. 3.4 (c). In Fig. 3.5 we have plotted the X-position of MWPC for all degrader foils without any mask in front of the detector. It is observed that the position resolution is worsened after the fragments pass through the degrader foils. This is due to the scattering of the fission fragments along the track in the Mylar foil. However, even after passing through 10 μm thick mylar foil, the image of the supporting wires are present as shown in Fig. 3.5.

The TOF spectrum has been obtained by taking the x-projection of the ΔE vs TOF plot, as shown in left panel of Fig. 3.6. It is seen that with the decrease in the energy of the fission fragments, the peaks are broadened due to the energy straggling in the Mylar foil and also become slightly asymmetric. By using double Gaussian fits to the timing spectrum, we have obtained the mean TOF and the width of the peaks in the distributions corresponding to light (T_L) and heavy (T_H) fragments. The measured TOF distributions of the fragments were transformed to the velocity distributions by analyzing event by event list mode data. The velocity distributions thus obtained for both the fragment groups are plotted in right panel in Fig. 3.6. We have obtained the centroid as well as the width of the distribution (FWHM) from the velocity spectra, by fitting with two Gaussian distributions for the heavy and light fragment groups as shown by solid lines in Fig. 3.6.

The velocity distributions obtained from the present measurement for two distances are

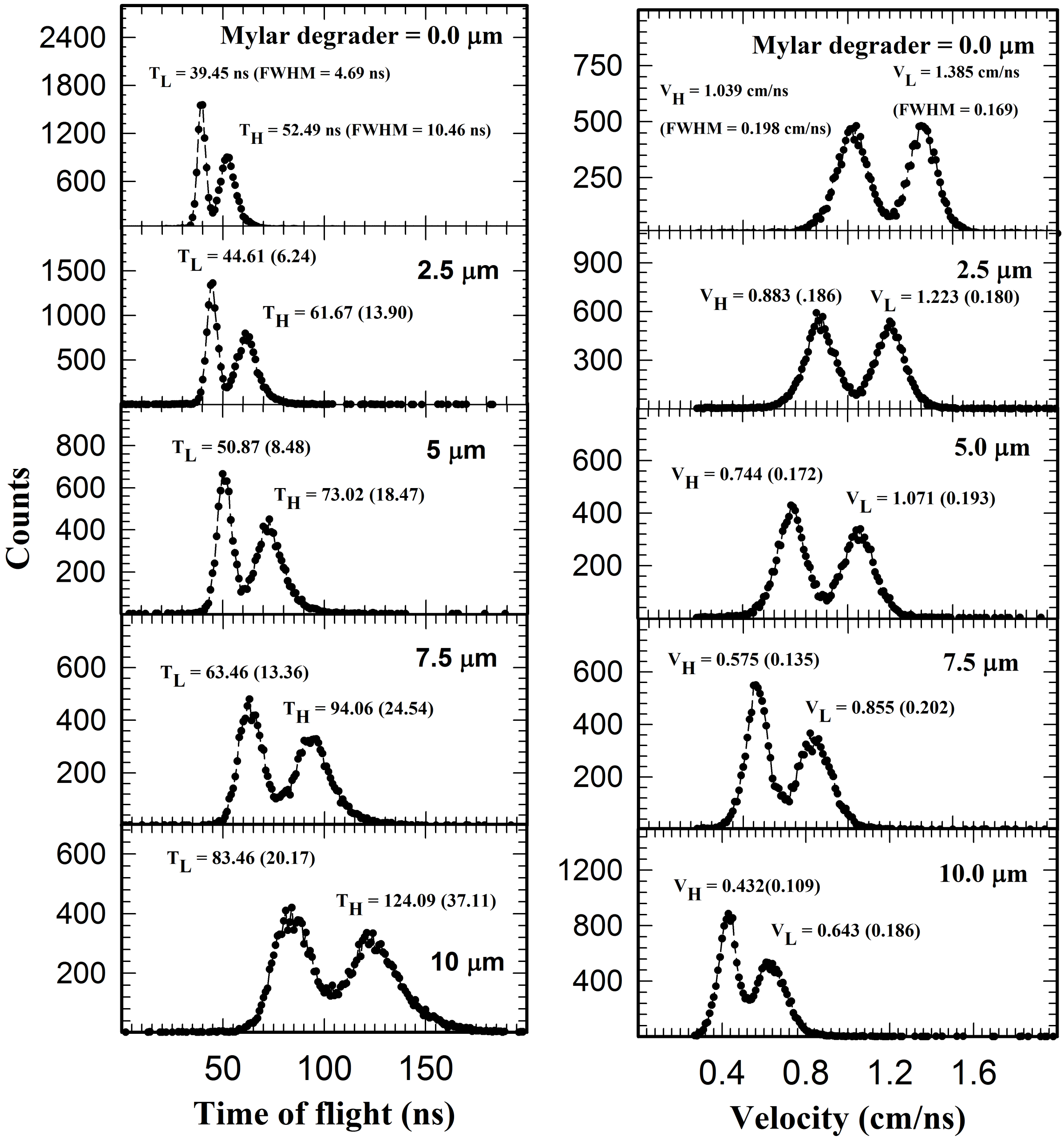

Figure 3.6: The TOF (flight path = 54.5 cm) and velocity distribution spectra for the FFs from ^{252}Cf after energy degradation with different thicknesses of Mylar layer. Solid line in each panel is the double Gaussian fit for heavy and light fragments.

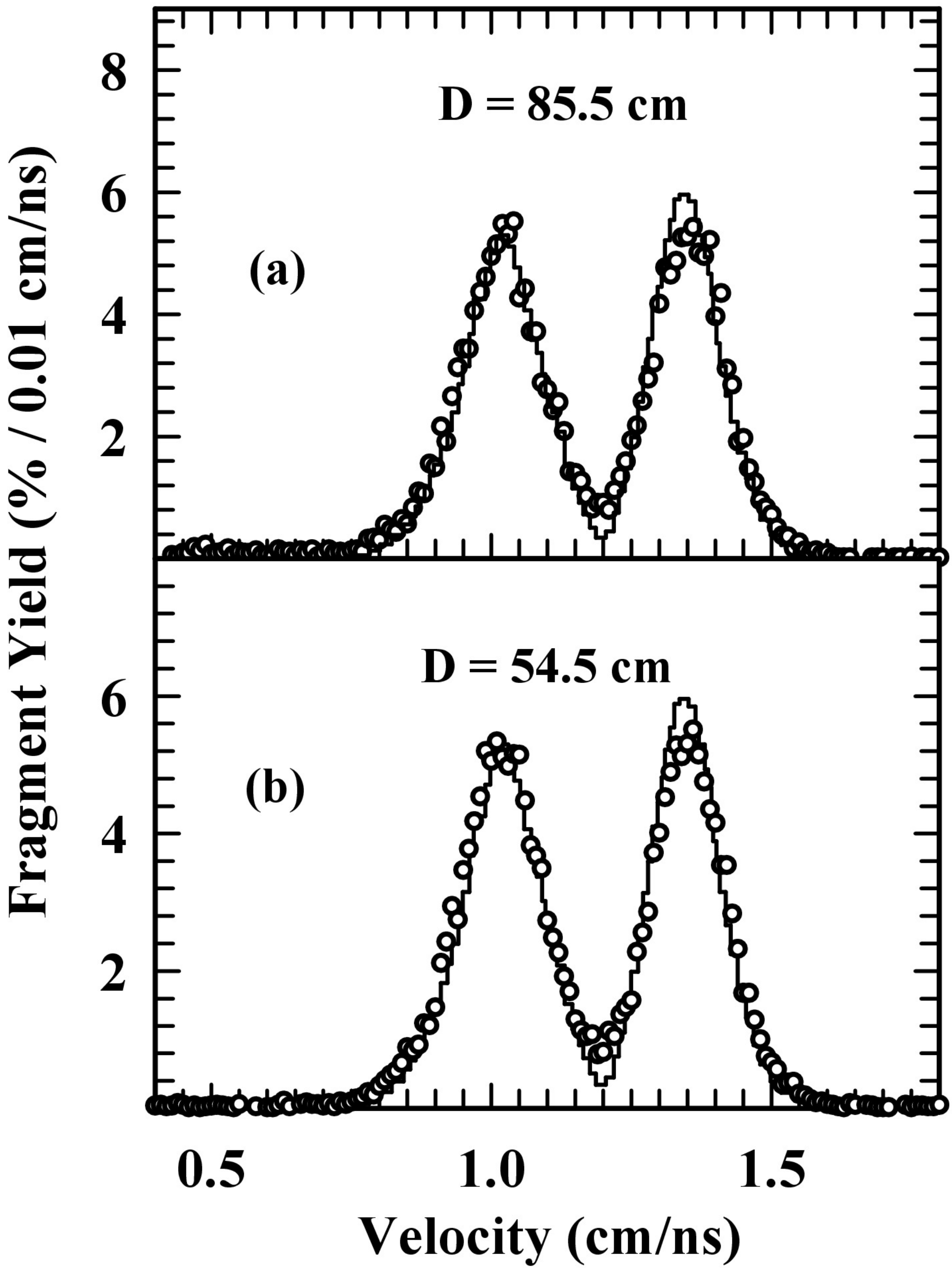

Figure 3.7: Velocity distribution spectra for two flight distances for the FFs from ^{252}Cf. For comparison the data taken from Ref. [70] are also plotted as solid lines.

consistent as shown in Fig. 3.7. For comparison, we have also plotted in Fig. 3.7 the data of the velocity distributions taken from Ref. [70]. The experimental TOF and the mean value of the centroid of heavy and light fragments after passing through each Mylar foil are listed in Table-3.1. The width (FWHM) of the velocity distributions for both the light and heavy fragment groups have been plotted in Fig. 3.8 for various fragment energies. From the measured peak values of the velocity distributions (V_L and V_H) after passing through 0, 1, 2, 3, 4 layers of Mylar foils and known values of the most probable light as well as heavy fragment masses (A_L = 108.39, A_H = 143.61) [70], the residual energies (E_L and E_H) of the most probable FFs were obtained by using the expression, $E = \frac{1}{2}AV^2$. We have also calculated the residual energies of the fragments after passing through each Mylar foil by using SRIM code [76] for light (Z = 42, A = 108) and heavy (Z = 56, A = 144) fragments and compared with the measured values. The experimental values of the residual energies for most probable light and heavy fragments are listed in Table-3.1 along with SRIM calculations. The experimental data for residual energies agree quite well with the simulated values in the beginning of the range as shown in Table-3.1. However, the SRIM calculations overpredict the experimental residual energies after passing through large thickness of the foils. As the fission fragments lose large amount of energy in the foils, the straggling effect becomes significant and improved theoretical calculations are required to explain the energy loss mechanism.

It is observed that for the heavy fission fragments, the width of the velocity peak decreases with the reduction in the fragment energies, but for light fragments the width does not show significant energy dependence. This behavior of energy dependence might be explained from Fig. 3.4, where, it is seen that for heavy fragments, there is a significant reduction in the width of the energy spectra as the fragments traverse through the foils. However it is observed that the change in the energy width is relatively small for lighter fragments. These differences in energy spectral shapes of light and heavy fragments reflect in velocity distribution width. The present results will provide very useful information in understanding the fragment velocity dependence of energy loss mechanism in nuclear fission.

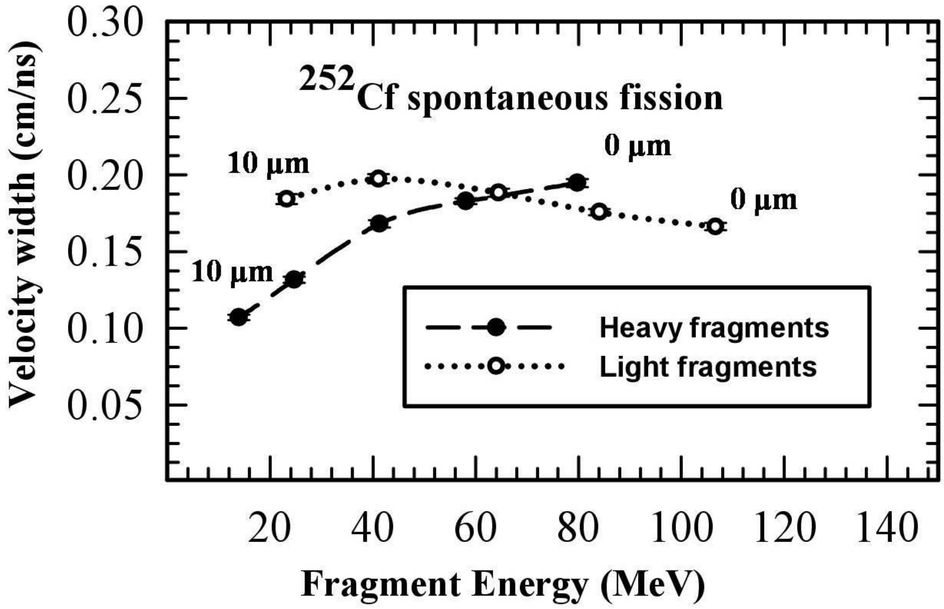

Figure 3.8: The velocity width (FWHM) plotted with fission fragment energies after degradation with Mylar foils of different thicknesses. Dotted and dashed lines are shown to guide the eye.

3.4 Measurement of the velocity distribution for fission fragments in ^{28}Si+^{197}Au reaction

For the measurement of fission fragment mass distribution employing the double velocity ($2V$) method, two identical MWPC detectors as described above were used in an in-beam experiment at BARC-TIFR Pelletron-LINAC accelerator facility, Mumbai. Pulsed beam of ^{28}Si having 154.6 MeV energy with 1.5 ns width and a period of 107.3 ns was used in this measurement. The fission fragments produced in ^{28}Si+^{197}Au reaction, were detected in coincidence by using two position-sensitive MWPC detectors mounted inside a general purpose scattering chamber of diameter 1.5 meter, on two movable arms as shown in Fig. 3.9. The anode plane was normal to the particle trajectories passing though the center of the detectors. The target was $\sim 250\,\mu$g/cm^2 self supporting gold foil. One of the detectors was placed at a distance of 55.0 cm (MWPC1) from the target ladder, while the other was kept at a distance of 27.5 cm (MWPC2). This will ensure the detection of the more

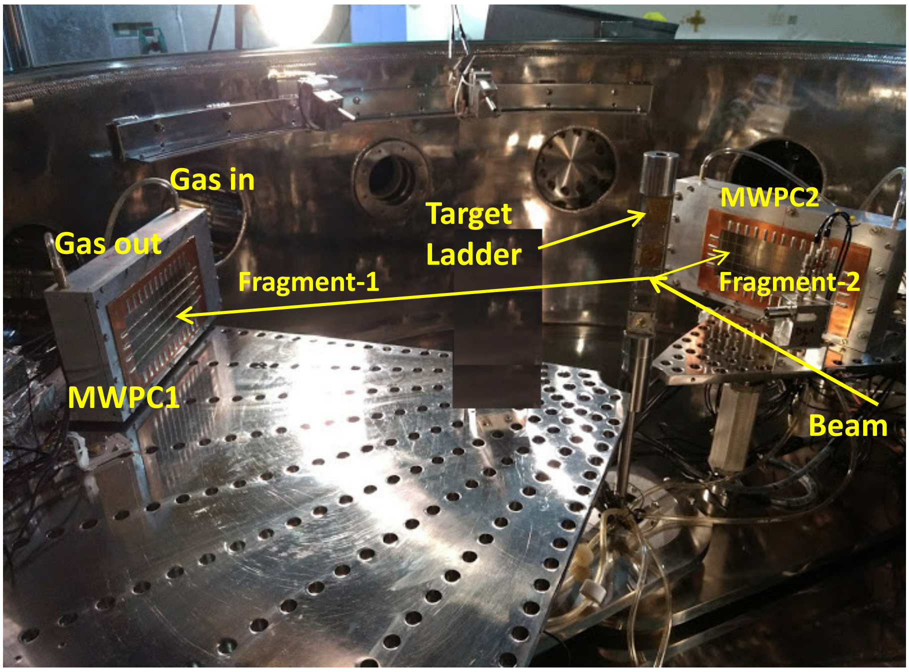

Figure 3.9: Photograph of the experimental setup showing two MWPC detectors mounted inside a general purpose scattering chamber at Pelletron-LINAC facility, for measuring fission fragment mass distribution from the fragment velocity measurement.

complementary fragments in MWPC2 correlated with the fragment detected in MWPC1, covering relatively larger solid angle. The in-plane angular coverage of the MWPC1 and MWPC2 were around 18.0° and 35.3°, respectively. The folding angle for ^{28}Si+^{197}Au reaction at a beam energy of 154.6 MeV for MWPC1 at θ_1 = 72° is 144°.

For the detection of fission fragments, MWPCs were operated with isobutene gas at a pressure of 3.0 Torr in continous flow mode. The X,Y positions, the energy loss in each of the detectors, the time difference between the arrivals of the coincident fragments at the detectors and individual TOF of the fragments with respect to RF beam bunching signal were recorded event by event. The position calibration of the detectors were carried out using the known positions of the edges of the detectors, when the events were collected in singles mode using ^{252}Cf source. The velocities were reconstructed from the timing and position information obtained in X and Y directions. V_{lab} was measured from the known distance and TOF. The conversion of V_{lab} to V_{cm} is given in section 3.8. In Fig. 3.10 we have plotted V_{1cm} and V_{2cm}, along with velocities measured by MWPC1 and MWPC2 in lab frame as V_{1lab} and V_{2lab} respectively. It is observed that the velocity distribution as well as the mean velocities are similar for the fission fragments measured by both the MWPCs. In case of $^{28}Si+^{197}Au$ reaction at 154.6 MeV, the velocity distributions show single broad peak in both the MWPCs because of the symmetric fission in heavy-ion induced fission reactions at higher excitation energies. Whereas, for spontaneous fission of ^{252}Cf, we have observed two distinct peaks in the velocity distribution as seen Fig. 3.6, corresponding to light and heavy fragment groups due to asymmetric fission.

The mass distribution for $^{28}Si+^{197}Au$ reaction was obtained from the measured velocity distribution of both the fission fragments by using the kinematic coincidence method [68]. Symmetric mass distribution was observed having peak position at around A/2 and details will be presented in Ref. [77]. We have estimated the fission fragment mass resolution for the present TOF setup and the details are discussed. The mass resolution obtained by this method was found to be 4.26% for $^{28}Si+^{197}Au$ reaction. The correlation plot between Total Kinetic Energy (TKE) in cm frame and Mass number at a beam energy of 145.0 MeV for ^{28}Si + ^{197}Au system is shown in 3.11. Here horizontal red line represents the value calculated by Viola's systematic. The vertical red line shows the mass centroid for symmetric fission. The TKE is calculated by using

$$TKE = \frac{1}{2}M_1V_{1cm}^2 + \frac{1}{2}M_2V_{2cm}^2 \tag{3.1}$$

. It can be seen that the experimental mean kinetic energy agrees with the value calculated using Viola's systematics [112]. Here the neutron correction has been taken in to account according to systematics given in [78] and references therein. Accordingly two neutrons have been assumed to be emitted from each fragment.

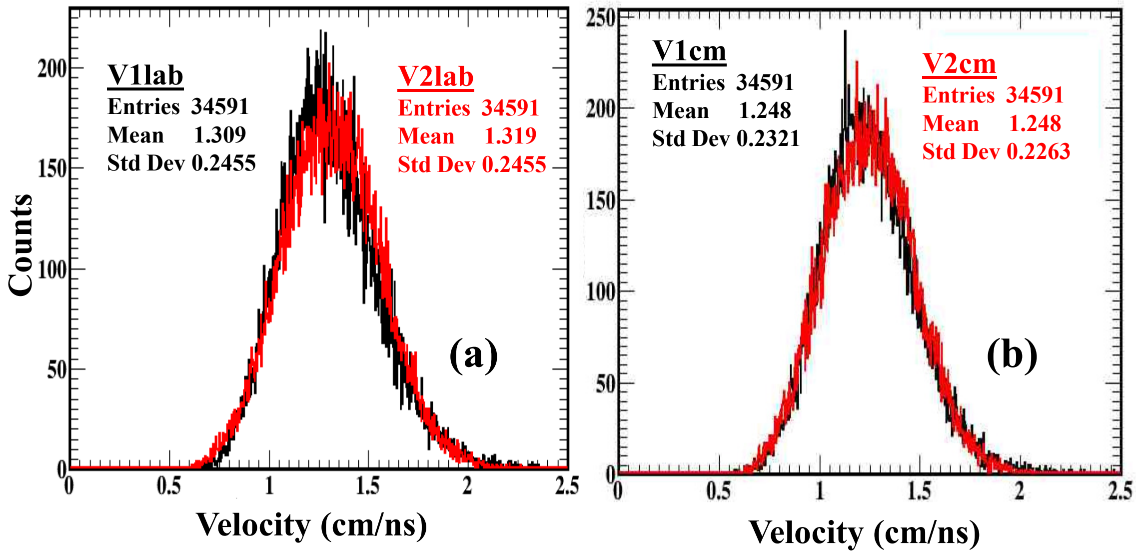

Figure 3.10: Velocity distribution of the fission fragments in lab frame and c.m. frame shown in panel (a) and (b) respectively for $^{28}Si+^{197}Au$ at a beam energy of 154.6 MeV. Black and red color represent fragments detected by MWPC1 and MWPC2 respectively.

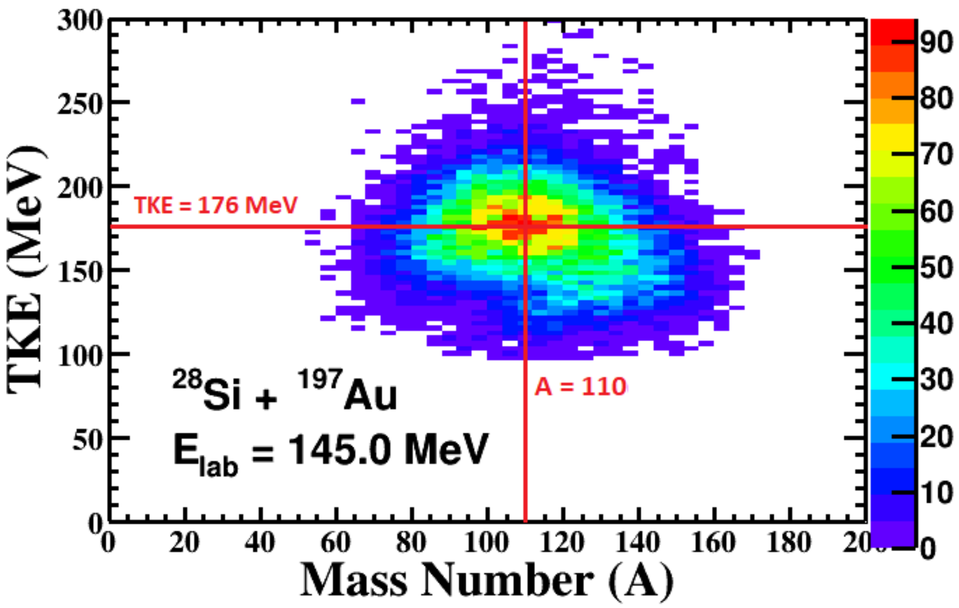

Figure 3.11: 2D correlation plot between Total Kinetic Energy (TKE) in cm frame and Mass number at a beam energy of 145.0 MeV for ^{28}Si + ^{197}Au system.

3.5 Kinematic details to obtain mass resolution in TOF measurement

The kinematic diagram for binary fission process is shown in Fig. 3.12. From the conservation of linear momentum it follows that:

$$\vec{V}_{cm} = \frac{M_P \vec{V}_P}{M_P + M_T} \tag{3.2}$$

$$M_1 \vec{V}_{1cm} = M_2 \vec{V}_{2cm} \tag{3.3}$$

where, $\vec{V}_{cm}$ is the velocity of the center of mass system, which is equal to the recoil velocity of the compound nucleus, by assuming full momentum transfer from projectile to target. M_P and $\vec{V}_P$ are the mass and velocity vector of the projectile. M_T is the target mass and $M_{1,2}$ are the masses of the FFs and $\vec{V}_{1,2cm}$ are the fragment velocities in the center-of-mass frame. From the velocity vectors shown in Fig. 3.12, we can write

$$\vec{V}_{1cm} = \vec{V}_{1lab} - \vec{V}_{cm} \tag{3.4}$$

$$\vec{V}_{2cm} = \vec{V}_{2lab} - \vec{V}_{cm} \tag{3.5}$$

Here, $\vec{V}_{1,2lab}$ are the velocity vectors of the fission fragments in the laboratory frame.

From the above equation, the magnitude of the fragment velocities in the c.m. frame are deduced as:

$$V_{1cm} = \sqrt{(V_{1lab}^2 + V_{cm}^2 - 2cos\theta_{1lab} V_{1lab} V_{cm})} \tag{3.6}$$

$$V_{2cm} = \sqrt{(V_{2lab}^2 + V_{cm}^2 - 2cos\theta_{2lab} V_{2lab} V_{cm})} \tag{3.7}$$

Here $\theta_{1,2lab}$ are the exit angles of the fission fragments with respect to the beam direction. Using these c.m. velocities of both the fragments and emplyoing the two-body kinematics

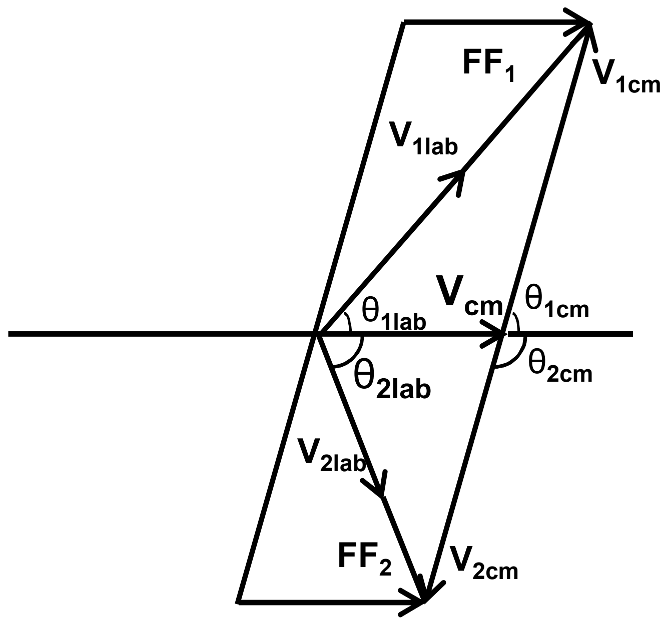

Figure 3.12: Kinematics of symmetric binary fission from compound nucleus.

for binary fission, the masses of the fragments are determined as follows;

$$M_1 = \frac{V_{2cm} M_{CN}}{V_{1cm} + V_{2cm}} \tag{3.8}$$

$$M_2 = \frac{V_{1cm} M_{CN}}{V_{1cm} + V_{2cm}} \tag{3.9}$$

where, M_{CN} is the mass of the compound nucleus. The deviations in the calculation will be due to the emission of light charged particles or neutrons. Using the above equations, the velocities of the fission fragments were calculated in the c.m. frame (V_{1cm} and V_{2cm}) and for ^{28}Si+^{197}Au reaction at a beam energy of 154.6 MeV.

By employing TOF method with two MWPCs, the fission fragment mass distribution is measured. We have obtained the total uncertainty in mass resolution by adding the velocity dispersion in quadrature.

From Eq. (7) we can write,

$$\delta M_1 = \frac{V_{1cm}V_{2cm}M_{CN}}{(V_{1cm}+V_{2cm})^2}\sqrt{\frac{\delta V_{1cm}^2}{V_{1cm}^2}+\frac{\delta V_{2cm}^2}{V_{2cm}^2}} \tag{3.10}$$

We have $M_{CN} = M_1 + M_2$ and replacing V_{2cm} in the above equation;

$$\delta M_1 = \frac{V_{1cm}^2 M_1(M_1+M_2)/M_2}{\left(V_{1cm}+V_{1cm}\frac{M_1}{M_2}\right)^2}\sqrt{\frac{\delta V_{1cm}^2}{V_{1cm}^2}+\frac{\delta V_{2cm}^2}{V_{2cm}^2}} \tag{3.11}$$

After solving we get,

$$\frac{\delta M_1}{M_1} = \frac{M_2}{M_1+M_2}\sqrt{\frac{\delta V_{1cm}^2}{V_{1cm}^2}+\frac{\delta V_{2cm}^2}{V_{2cm}^2}} \tag{3.12}$$

Assuming symmetric fission;

$$\frac{\delta M_1}{M_1} = \frac{1}{2}\sqrt{\frac{\delta V_{1cm}^2}{V_{1cm}^2}+\frac{\delta V_{2cm}^2}{V_{2cm}^2}} \tag{3.13}$$

In Eq. 3.4, V_{cm} is constant for a given target projectile combination and a fixed beam energy. Therefore, by differentiating the Eq. 3.4;

$$|\delta\vec{V}_{1cm}| = |\delta\vec{V}_{1lab}| \tag{3.14}$$

Let's consider only magnitude and divide above equation with V_{1cm};

$$\frac{\delta V_{1cm}}{V_{1cm}} = \left(\frac{V_{1lab}}{V_{1cm}}\right)\frac{\delta V_{1lab}}{V_{1lab}} \tag{3.15}$$

Uncertainty in the distance can be neglected, hence;

$$\frac{\delta V_{lab}}{V_{lab}} = \frac{\delta t}{t} \tag{3.16}$$

where t is the TOF. Using Eq. 3.16 into Eq. 3.15

$$\frac{\delta V_{1cm}}{V_{1cm}} = \frac{\delta t}{t_1}\left(\frac{V_{1lab}}{V_{1cm}}\right) \tag{3.17}$$

where, δt is the total uncertainty, which has two contributions: (i) from width of the RF which provides the start trigger, (ii) time resolution of the MWPC which gives stop trigger and (iii) target thickness can also result in poor mass resolution which can be minimized by choosing a sufficiently thin target. Therefore,

$$\delta t = \sqrt{\delta t_{RF}^2 + \delta t_{MWPC}^2} \tag{3.18}$$

The width of RF used in the present heavy-ion experiment is around 1.5 ns, which comes from the width of beam pulse. Time resolution for the MWPCs used in the present work is around 180 ps as measured in Ref. [79] for a MWPC having similar configuration. Therefore, time uncertainty for the RF and one MWPC would be 1.51 ns. For the mass resolution estimation purpose we can consider only peak values of the lab and center-of-mass velocities of the fission fragments. In the present work, we can see from Fig. 3.10 that the peak values of the velocities in the lab and center-of-mass frame are 1.32 cm/ns and 1.25 cm/ns respectively. In this measurement the MWPC1 and MWPC2 were kept at distances of 55 cm and 27.5 cm, respectively. Therefore,

$$\frac{\delta V_{1cm}}{V_{1cm}} = \frac{\delta t}{t_1}\left(\frac{V_{1lab}}{V_{1cm}}\right) = 0.0377 \tag{3.19}$$

Similarly,

$$\frac{\delta V_{2cm}}{V_{2cm}} = 0.0765 \tag{3.20}$$

Using Eq. 3.19 and 3.20 into Eq. 3.13 we get,

$$\frac{\delta M_1}{M_1} = 4.26\% \tag{3.21}$$

The mass resolution will be reduced slightly due to pre-scission and post-scission neutron evaporation, which has not been taken in to account in the above calculation. Also the target thickness can increase the mass width, which can be minimized by choosing a thin target.

Table 3.1: Measured TOF (T_L,T_H), mean velocities (V_L,V_H) and energies (E_L,E_H) for most probable light and heavy fragments are listed. The SRIM calculated values of residual energy are also presented for a light (Z_L = 42, A_L = 108) and a heavy (Z_H = 56, A_H = 144) fragment after passing through different foil thickness.

Mylar (μm)	T_L (ns)	T_H (ns)	V_L (cm/ns)	V_H (cm/ns)	E_L (MeV)	E_H (MeV)
0.0	39.45(6)	52.49(12)	1.378(1)	1.035(1)	106.65 (15)	79.73(15)
2.5	44.61(6)	61.67(13)	1.223(1)	0.883(1)	84.04(14)	58.06(13)
					85.94[1a]	60.94[1a]
5.0	50.87(8)	73.02(17)	1.071(1)	0.744(1)	64.39(12)	41.21(11)
					66.49[1a]	44.47[1a]
7.5	63.46(12)	94.06(21)	0.855(2)	0.575(1)	41.03(19)	24.63(09)
					48.80[1a]	30.68[1a]
10.0	83.46(20)	124.09(35)	0.643(2)	0.432(1)	23.20(14)	13.88(06)
					33.39[1a]	19.89[1a]

[1a] SRIM calculation

3.6 Summary and Conclusion

In summary, the velocity distribution of fission fragments from spontaneous fission of ^{252}Cf source has been measured by employing a new TOF method using a BaF_2 detector as "Start" and MWPC as "Stop" detector. Two position sensitive MWPC detectors have been developed for the detection of FFs and the timing characteristics have been investigated using a ^{252}Cf source. The position information has been obtained by using the delay-line method and the position resolution is about 1.0 mm in both X and Y directions. The velocity distribution for FFs from ^{252}Cf obtained from the measured TOF using two detectors (BaF_2 and MWPC) having fast timing signals and known travel path by the fission fragments is found to be very accurate. The width of the velocity distribution has been measured for various fragment energies by degrading them using Mylar foils of four different thickness (2.5-10 μm). It is observed that the width of the distribution decreases with the reduction in the fragment energies for the heavy fission fragments, but the light fragments show a weak dependence on energy. Since the anode pulses from the MWPC are very fast (rise time ~ 6 ns), two similar MWPCs have been found to be suitable for studying the fragment mass distribution in heavy-ion induced fission reactions providing a mass resolution of about 4.26%.

Chapter 4

Measurement of fission fragment mass distributions in ^{28}Si + ^{197}Au and ^{9}Be + ^{232}Th,^{209}Bi reactions

4.1 Introduction

In reactions with heavy-ion beams at energies around the Coulomb barrier (V_b), non-compound fission such as fast-fission, quasifission (QF) and pre-equilibrium fission are competitive processes with fully equilibrated compound nuclear fission (CNF) [80, 81].

The relative probability of non-compound processes with respect to CNF depends on entrance channel parameters viz., mass asymmetry, N/Z ratio, the Coulomb factor Z_pZ_t (where, Z_p and Z_t are the atomic number of the projectile and target), deformation, shell structure and orientation of the colliding nuclei [82–84]. When complete fusion is achieved after contact of two colliding heavy nuclei, the composite system evolves in the deformation space, governed by the potential energy surface (PES). For CNF, a compact configuration is formed after complete equilibration in mass, charge, energy and shape degrees of freedom and the excited compound nucleus undergoes fission with the signatures of fusion-fission process. In some cases, the unstable elongated di-nucleus may also reseparate into two heavy fragments instead of diffusing to more compact stable equilibrated shapes and this premature separation of fission fragments (FFs) is called QF [80, 85]. In the QF process, the unconditional saddle point shape is more compact than the entrance-channel contact configuration of the system. As the experimental observables have considerable overlap for CNF and QF processes, the main motivation in heavy ion fission reaction studies is to separate these reaction channels having very different lifetimes [86–88]. At energies around the barrier, understanding of the dynamics of QF reactions is vital to predict optimal reactions for future investigation of superheavy elements. The dominance of QF reactions mask the fusion-fission process, which implies a substantial reduction of the fusion cross section. Thus, the QF process is a major hurdle in forming very heavy or superheavy evaporation residues (ER) in these reactions. To optimize the exploration of the superheavy element landscape, the key challenge is to understand the competition between non-compound and compound nuclear fission.

From the mass-angle correlation studies, it was reported that both CNF and QF correspond to full momentum transfer [69, 89]. At sub-barrier energies, the cross section for compound nucleus formation decreases rapidly and identifying the yield of a small component of fusion-fission is thus problematic, where transfer induced fission can be significantly large [90–92]. It is possible to disentangle the contribution of fusion-fission and transfer fission from precise measurement of the linear momentum and folding angle distributions [93–98]. Measurements of fission fragment mass distributions is very important experimental tool, which helps to distinguish between the fully equilibrated CNF and QF processes. For QF reactions, there will be strong dependence of the fragment mass distribution on the excitation energy of the fissioning nucleus as well as the target/projectile masses. The onset of mass asymmetry or a sudden increase in width would be a strong signal of QF reaction. The presence of QF can be inferred from large angular anisotropies and/or wide fission fragment mass distributions which are inconsistent with fusion-fission reactions [80, 93–96, 99–104].

The energy dependence of fission fragment angular anisotropy and mass width show a sudden deviation from the systematic behavior of CNF for ^{16}O,^{19}F + ^{232}Th reactions at energies around the Coulomb barrier [52, 93–96, 99–101] as shown in Fig. 4.1. These anomalous results with the prolate deformed ^{232}Th target, were interpreted by assuming siginificant presence of orientation-dependent QF mechanism at these energies. More recently, Nishio *et al*. have carried out detailed studies on the effect of nuclear orientation on the mass distribution of fission fragments in ^{16}O,^{34,36}S+ ^{238}U reactions and suggest that the QF process is dominant in the sub-barrier region, where the interaction of the projectile is due to the tips of the prolate-deformed target [98, 105, 106]. The variance of mass distribution (σ_m^2) values are anomalously large at sub-barrier energies for ^{19}F + ^{209}Bi reaction, but for ^{16}O+ ^{209}Bi system, the observed mass width shows a smooth variation with beam energy, indicating the absence of QF for this reaction [107] as shown in Fig. 4.2. This has been recently confirmed by Dubey *et al.* [108]. It is not yet settled how the entrance channel parameters, particularly, the deformation and/or mass asymmetry of the colliding heavy nuclei influence the QF process. In order to further investigate the role of the entrance channel on fission fragment mass distribution, we have measured the fission fragment mass distribution for ^{28}Si + ^{197}Au system by populating the same compound nuclear mass (A_{CN} = 225) as in case of ^{16}O + ^{209}Bi reaction [100, 107]. In the present work, the mass distributions were obtained from the coincidence measurement of the velocity distribution of FFs, by employing two multi-wire proportional counters

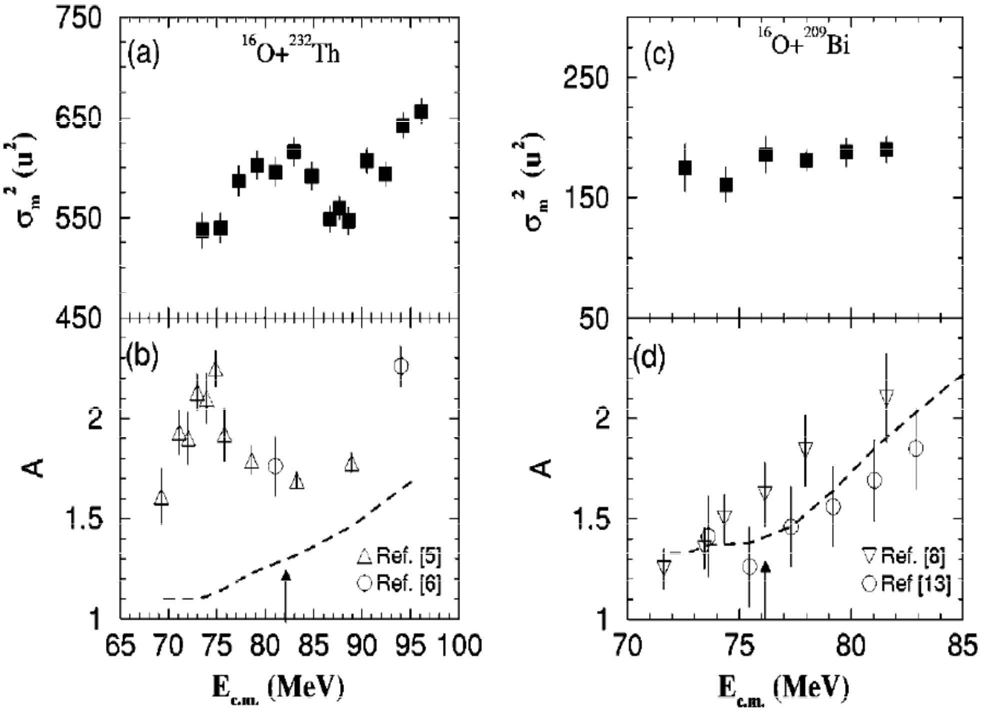

Figure 4.1: Square of mass width as a function of beam energy scaled with Coulomb barrier E$_{cm}$/V$_b$ for (a) ^{16}O+ ^{232}Th and (c) ^{16}O + ^{209}Bi reactions [100, 107].

(MWPCs) for beam energies 135.4 to 180.0 MeV. A sharp change in the σ_m^2 for beam energies around the V$_b$, indicate the importance of QF on FF mass distribution. The variation of σ_m^2 with energy has been compared with the theoretical calculations by solving the Langevin equation for fully equilibrated compound nuclear fission [109, 110].

The reaction mechanisms involved in reactions with weakly bound projectile is different from that involved in reactions with tightly bound projectiles. Enhancement of the fusion cross sections due to the coupling of the breakup channels to fusion or hindrance of fusion due to the loss of incident flux because of breakup are the observations noticed in recent experiments on reactions involving weakly bound projectiles with low breakup threshold energies.

In case of weakly bound projectile induced reactions, apart from complete fusion-fission (CFF), incomplete fusion fission (ICF) is competitive process and becomes dominating at sub-barrier energies. ICF corresponds to breakup of projectile followed by capture of one of the breakup fragments by target followed by fission. ICF also corresponds to transfer

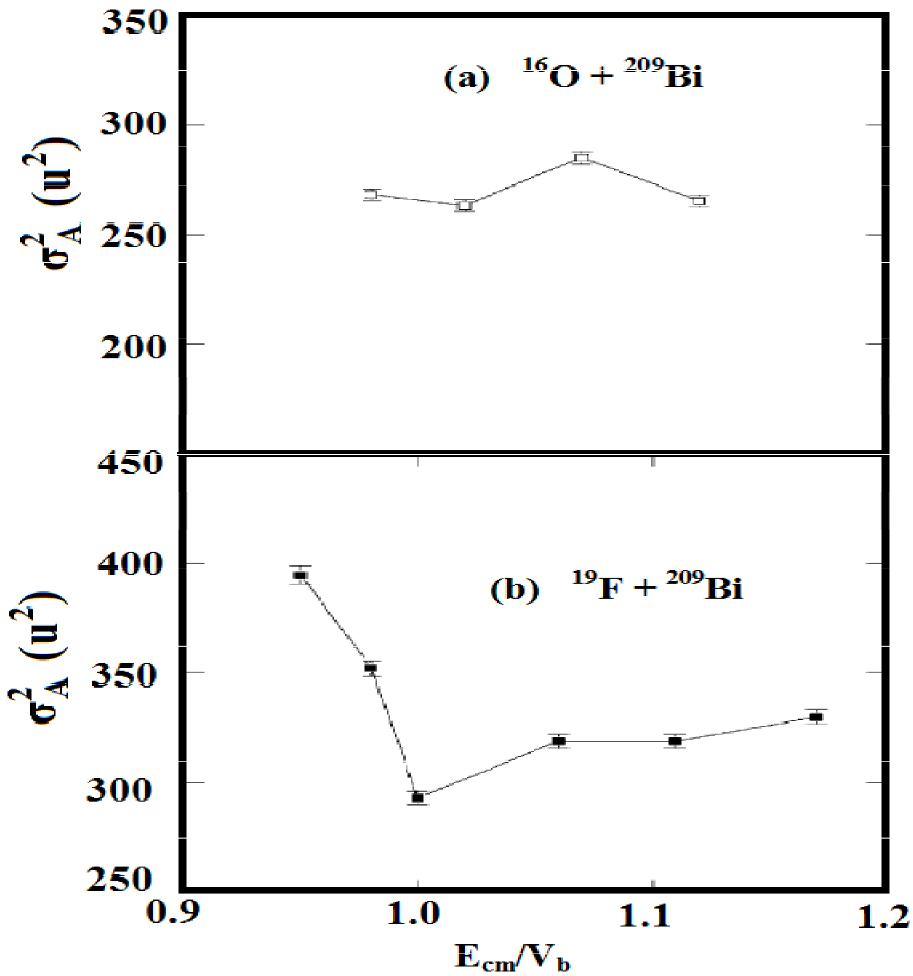

Figure 4.2: Square of mass width as a function of beam energy scaled with Coulomb barrier E_{cm}/V_b for (a) ^{16}O+ ^{209}Bi and (b) ^{19}F + ^{209}Bi reactions [107].

of nucleons between projectile and target. In ICF, the linear momentum transferred to the target is either less or more than the incident momentum of the projectile. At above barrier energies, the ejectiles are emitted in the forward direction carrying a part of the incident momentum, and the recoil momentum is less than the incident momentum. As a result, the folding angles are larger for ICF as compared to CFF at above barrier energies. At energies below Coulomb barrier, the ejectiles are emitted in backward direction and transfer more recoil to the target than incident momentum. The folding angles are smaller for ICF as compared to CFF at below barrier energies [9].

Itkis *et al.* [47] measured the fission fragment mass distribution for beam energies 62.5,

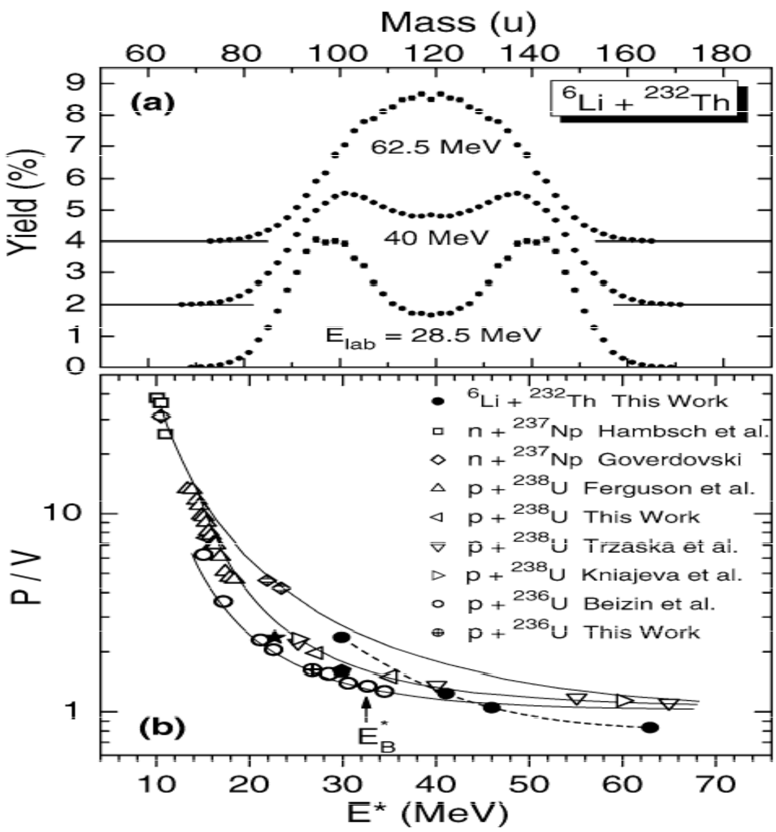

Figure 4.3: (a) Fission fragment mass distribution for different beam energies. (b) Peak to valley ratio vs excitation energy for several systems [47].

40 and 28.5 MeV (Fig. 4.3 (a)). It was observed that the asymmetry in the mass distribution increases with the decrease in beam energy. The P/V has been plotted for different systems as shown in Fig. 4.3 (b). The results show that the contribution of CFF to the total fusion-fission (FF) cross section for reaction ^{6}Li+^{232}Th is only 27% at ^{6}Li projectile energy of 28.5 MeV (2 MeV below Coulomb barrier). Again there is a sharp increase in the peak to valley (P:V) ratio of FF mass distribution with the decrease in bombarding energy observed by Santra *et al.* [46] for ^{6,7}Li + ^{238}U reactions as shown in Fig. 4.4. As the beam energy falls below the fusion barrier, the full width half maximum (FWHM) of the FF folding angle distribution is found to increase at sub-barrier energies, unlike the reactions involving tightly bound projectiles where a linear decrease in FWHM is expected. This has been explained due to the increasing contribution of ICF.

The small breakup threshold energy of ^{9}Be into ^{8}Be + ^{1}n(1.67 MeV) or into ^{5}He + ^{4}He

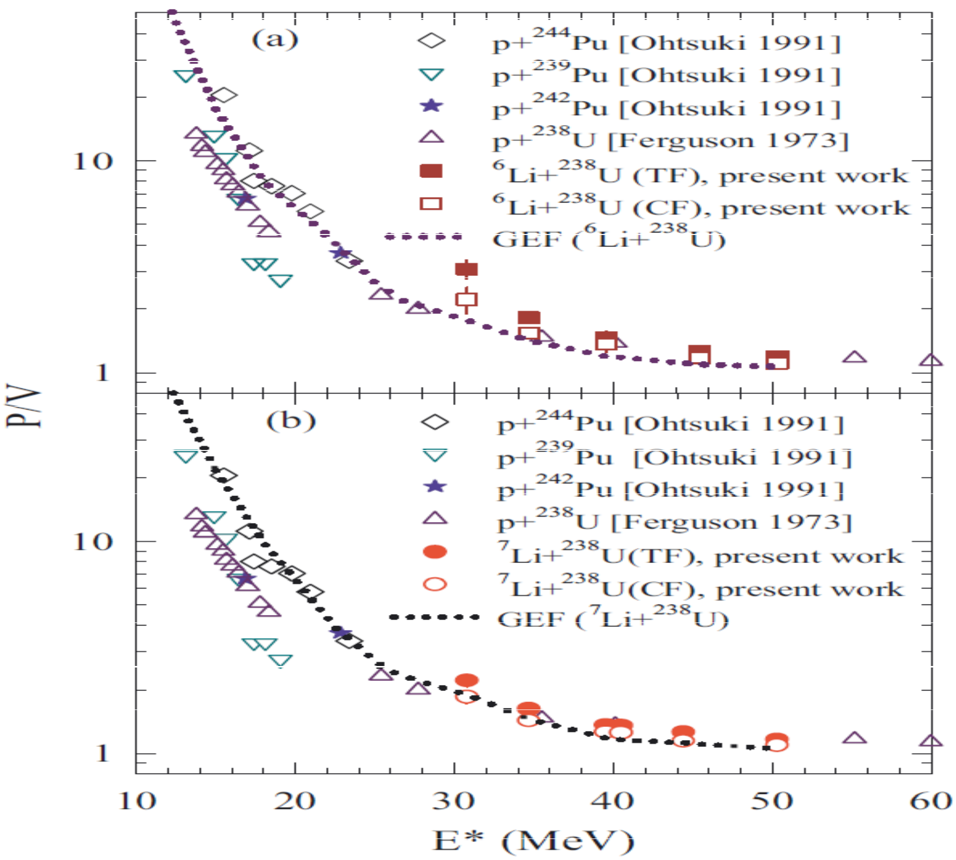

Figure 4.4: (a) Peak to valley ratio for various systems as a function of excitation energy compared with ^{6}Li + ^{238}U. (b) Peak to valley ratio as a function of excitation energy, compared with ^{7}Li + ^{238}U [46].

(2.55 MeV) makes it interesting to study the effect of breakup on fission fragment mass distribution.

4.2 Experimental method

The experiment was performed using pulsed ^{28}Si beam of ~ 1.5 ns width and a period of 107.3 ns from the Pelletron-LINAC facility at TIFR, Mumbai. A self-supporting ^{197}Au target of thickness 250 μg/cm^2 and oriented at 45° to the beam direction, was used in the experiment. Two monitor detectors with thickness of around 300 μm were mounted at 65 cm from the target with a collimator of 1 mm diameter. They were kept at fixed angles of ± 20° with respect to beam direction and were used to monitor the elastically scattered particles. Fission fragments were detected in coincidence by using two position-sensitive MWPCs mounted on two movable arms on the opposite sides of the beam axis inside a general purpose scattering chamber. The mounting arrangement of the MWPCs and other details of the experimental setup is given in Ref. [111]. Both the MWPCs used in the present experiment had window dimension of 17.5 cm × 7 cm. One of the detectors was placed at a distance of 55.0 cm (MWPC1) from the target ladder, while the other at a distance of 27.5 cm (MWPC2). Polar angular coverage of the detectors were about 18.0° and 35.3° for MWPC1 and MWPC2, respectively. The angular coverages of the detectors were verified with the help of Theodolite (A theodolite is a precision optical instrument for measuring angles between designated visible points in the horizontal and vertical planes). To verify the angular coverage of the detectors, each detector entrance window edge was brought in line with the cross-wire of the Theodolite. The angle of rotation of corresponding arm of the scattering chamber from one edge to the other edge of the entrance window gives the angular coverage of the detector. The angular coverage of the detector was verified theoretically using trignometric formulas and known distances from target ladder to the detector centres. The movable arms of the scattering chamber can be moved up and down to adjust the height of the detector to bring their centres in line with the beam collimator centre. The height of the detectors was adjusted and to avoid tilting of detectors, the spirit level was used. The arms of the scattering chamber can be moved inside the chamber to change the angles of the MWPCs with respect to beam axis. The azimuthal angular coverage of the MWPCs were 7.2° and 14.2°. Tygon tubes connected MWPC's feed throughs to two gas feed throughs attached to one of the side ports of the chamber. The pumping system was handled carefully while pumping down the chamber and detectors as the gas detector windows were very thin. While pumping, the targets were kept in such a way that they avoided any direct blast of air. After creating a rough vacuum (10^{-3} mbar), the chamber was isolated from the detectors and further pumped down to create vacuum of about 5×10^{-6} mbar. To create rough vacuum (10^{-3} mbar) two rotary vacuum pumps were used in roughing mode. After reaching (1×10^{-3} mbar), rotary pumps were put in backing of turbo vacuum pumps and the turbo vacuum pumps were switched on and turbo gate valves were opened. With turbo vacuum pumps, the chamber was evacuated to 5×10^{-6} mbar. The gas detectors were operated with a steady flow of isobutane gas at a low pressure of ($\approx$ 3.0 mbar). The energy of the projectile varied from 135.4 MeV to 180 MeV in the lab frame. The Coulomb barrier for the system ^{28}Si + ^{197}Au is 144.5 MeV in the lab frame of reference. The projectile energy varies from 0.94 of Coulomb barrier to 1.25 of Coulomb barrier. At this energy range fast-fission is not expected.

The detectors provided a position resolution of better than 1.0 mm. An 'OR' signal of the CFDs (constant fraction discriminator) of the two anode signals taken through fast timing pre-amplifiers of the two MWPC's with the Or of the CFDs of the monitor detector signals were used to generate a master trigger for the data acquisition system in these measurements. X(and Y) position measurement of each MWPC was carried out using a Time to Amplitude Converter (TAC), with the signal from CFD of respective anode as the start signal and the signal from CFD of X (and Y) after a suitable delay as the stop signal. A TAC signal was formed by taking the start signal from the CFD of anode from the back detector and the stop from the delayed signal from the CFD of anode from the front detector. TAC signals were also formed by taking the start signal from CFD of anode of the MWPC's and the stop signal from CFD of RF Pulse. The data were collected in event by event mode for offline analysis. The partial energy loss of the different particles in each of the detectors were collected from Cathode signal of the corresponding MWPC.

In another experiment, a similar set up has been used to study the mass distribution of fission fragments in ^{9}Be + ^{209}Bi,^{232}Th reactions. The self-supporting targets, ^{232}Th with a thickness of 850 μg/cm^2 and ^{209}Bi with a thickness of 350 μg/cm^2, were used.

4.2.1 Position Calibration of the Multi-wire proportional Counters (MWPC's)

The position calibration of the detectors was carried out using the known positions of the edges of the illuminated areas of the detectors, when the events were collected in singles mode using ^{252}Cf source. The calibrated X and Y positions from the two detectors were then converted to θ and ϕ respectively.

4.2.2 Time Calibration

The position signals X,Y and anode signals of the two MWPC's gives the timing information, which are collected by using Time to Amplitude Converters (TACs). The TAC used for X position signal was having a range of 500 nsec, while that used for Y position signal was having a range of 200 nsec. The other three TACs, namely between anode1 and anode2, between anode1 and RF signal, and between anode2 and RF signal were having a range of 500 nsec. It is needed to calibrate the TACs to know the linearity of the TACs. For calibrating the TAC we have used a time calibrator which generates a start and stop pulse having a definite time interval between them and a definite range. The start and stop signals from the time calibrator are connected to TAC. The master gate for calibrating TAC is generated from time calibrator start signal. The period between the start and stop pulses of the TAC were varied and a time spectrum was generated. The total range of the TAC in terms of channel number is 4K. All the seven TACs were calibrated one after the other in the same manner.

4.3 Data Analysis

In Fig. 4.5 (a) we have shown two dimensional plot between X positions of both the detectors at 180 MeV beam energy. We don't see a separate band of transfer induced

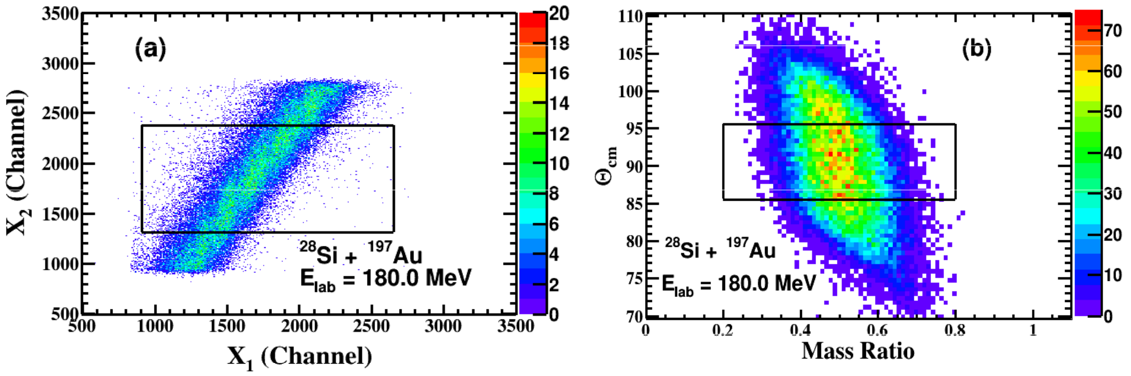

Figure 4.5: (a) Two-dimensional plot of X_1 position vs X_2 position of fragments in ^{28}Si + ^{197}Au reaction. (b) Mass ratio Vs polar angle in center of mass frame of fission fragments in MWPC1.

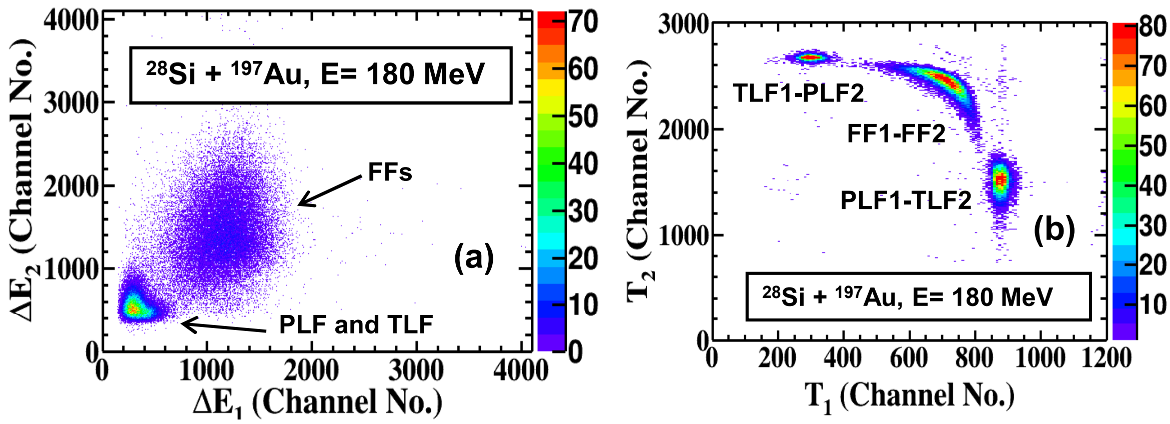

Figure 4.6: (a) Two-dimensional plot of ΔE_1 vs ΔE_2 showing the separation of fission fragments from PLF and TLF in ^{28}Si + ^{197}Au reaction. (b) Time correlation of fragment-1 detected by MWPC1 and fragment-2 detected by MWPC2 with reference to RF signal.

fission events in correlation plot between X positions of both the detectors. Thus we conclude that the contribution of transfer induced fission is negligibly small. At 180 MeV or 1.25 times of barrier energy, if transfer fission events were present, it would have linear momentum component smaller than the full momentum transfer and the folding angle will be greater than that for full momentum transfer events. But no such band is obsereved in the two dimensional plot. In Fig. 4.5 (b) Mass ratio Vs polar angle in center of mass correlation plot has been given.

The FFs passing through the MWPC1 and MWPC2 respectively provide signals having information on the energy deposition, ΔE_1 and ΔE_2. Fig. 4.6(a) shows the correlations between ΔE_1 and ΔE_2 of the complementary fragments in both the MWPCs for ^{28}Si + ^{197}Au reaction for projectile energy of 180.0 MeV. From this two dimensional plot, the FFs are separated from the projectile-like fragments (PLFs) and target-like fragments (TLFs). We have recorded the individual time of flight (TOF) with reference to the RF signal, T1 and T2 respectively for both the fragments detected by MWPC1 and MWPC2. The timing correlations of T1 and T2 at the highest beam energy has been plotted in Fig. 4.6(b), showing very clear separation of the FFs from PLFs and TLFs. There are three different possibilities of triggering the MWPC detectors: (i) target-like fragment (TLF1) detected by MWPC1 and projectile-like fragment (PLF2) detected by MWPC2, (ii) target-like fragment (TLF2) detected by MWPC2 and projectile-like fragment (PLF1) detected by MWPC1, (iii) fission fragments (FF1 and FF2) detected by both the MWPCs. The Time to Amplitude Conversion (TAC) spectrum was recorded with a start signal from MWPC1 and the stop signal from MWPC2. Fig. 4.7 shows the TAC spectrum of the time difference between the arrival of complementary fragments in the MWPCs for all energies. The time difference spectra show three clearly separated peaks corresponding to (TLF1-PLF2), (FF1-FF2) and (PLF1-TLF2) detected by MWPC1 and MWPC2 respectively at all energies.

For the mass distribution measurement, the MWPCs were kept at folding angle for symmetric fission, calculated from the Viola systematics [112]. The MWPC1 was mounted at a fixed angle (θ_{lab} = 71°) and MWPC2 was kept at an appropriate angle, which depends on the beam energy. The emission angle for each fragment was determined from the calibrated X and Y positions of the fragments on the MWPCs and then converting to θ and ϕ. The velocities were reconstructed from the timing and position information obtained in both X and Y directions after processing the list mode data. The fission events were separated by putting a gate to select the FF1-FF2 from the two dimensional plot of T1 vs T2 [Fig. 4.6(b)]. The velocity distribution as well as the mean velocities are similar for the fission fragments measured by both the MWPCs and the details are given in the recently

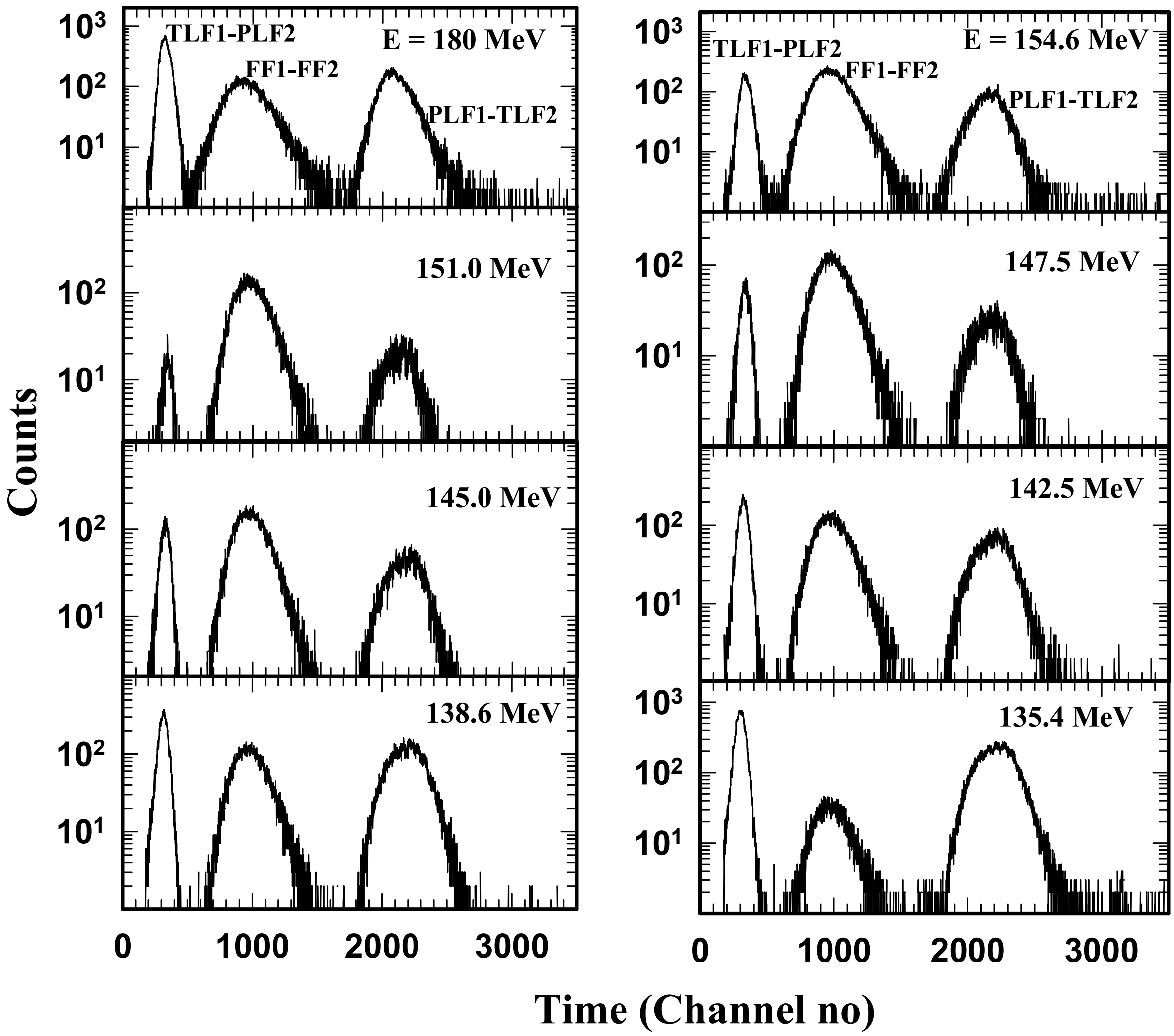

Figure 4.7: TAC spectrum for start signal from MWPC1 and stop signal from MWPC2 for various beam energies for ^{28}Si + ^{197}Au reaction.

published paper [111]. The fragment velocities (V_{1lab},V_{2lab}) in the laboratory frame were reconstructed using the time and position information. The fission fragments from full momentum transfer events (for FF and QF) were exclusively selected from the correlation of the velocity of the fissioning system ($V_{\|}$) in the beam direction relative to the recoil of the fused system and the velocity perpendicular to the reaction plane ($V_{\perp}$) as well as the correlation of the polar and azimuthal angles of the fragment (θ and ϕ respectively) with respect to the beam axis.

For ^{9}Be + ^{232}Th reaction, the conservation of momentum was used to obtain mass distribution. The criteria used to correct timing information was that the mass ratio distribution is reflection symmetric around θ_{cm}=90°. The Kinematic coincidence method [36] to separate transfer and elastic events from full momentum transfer fission events was used. Fig. 4.8 shows the TAC spectrum for the time difference between the arrival of coincident fragments at the two detectors for ^{9}Be + ^{232}Th at various energies. The peaks corresponding to coincidence between projectile like fragments(PLFs) and Target like fragments(TLFs) are not observed in the present spectrum. This is because of small stopping power of PLFs and they lose very small energy in the gaseous medium of MWPC as compared to fission fragments and TLFs. The TAC spectrum is broad at the 45 MeV beam energy. As we go down in energy the spectrum starts bifurcating in to two distinct peaks. This is because of increasing influence of incomplete fusion and/or relatively smaller excitation energy of fissioning nucleus. The TAC spectrum for ^{9}Be + ^{209}Bi system was single gaussian like peak. Fig. 4.9 shows the raw two dimensional position spectrum for MWPC1 as well as the coincidence between the X-positions of the two MWPCs for ^{9}Be + ^{232}Th. For in-beam experiment, the dips due to the supporting wire are not prominent due to the wandering of the beam on the target. Thus the position calibration has been taken from the 2D spectrum generated by using ^{252}Cf source and mounting it at the target position.

Fig. 4.10 shows the folding angle distribution in lab frame for ^{9}Be + ^{232}Th reaction. The folding distribution extends beyond 180°. The events which are around 180°and beyond correspond to "Stopped-Fission". The origin of these events is still debatable. The stopped-fission was also observed by Majumdar *et al.* [123, 126] and Hinde *et al.* [127]. Fig. 4.11 shows the folding angle distribution for ^{9}Be + ^{209}Bi reaction.

Fig. 4.12 shows the parallel component of the velocity of the fissioning nucleus with respect to beam direction as a function of mass ratio for ^{9}Be + ^{232}Th reaction. The ICF and complete fusion-fission are merged within each other. Thus, it is difficult to separate full momentum and partial momentum transfer events. Fig. 4.13 shows the correlation between parallel and perpendicular velocities of fissioning nucleus with respect to beam direction for ^{9}Be + ^{232}Th reaction. The corrections due to energy loss of projectile as

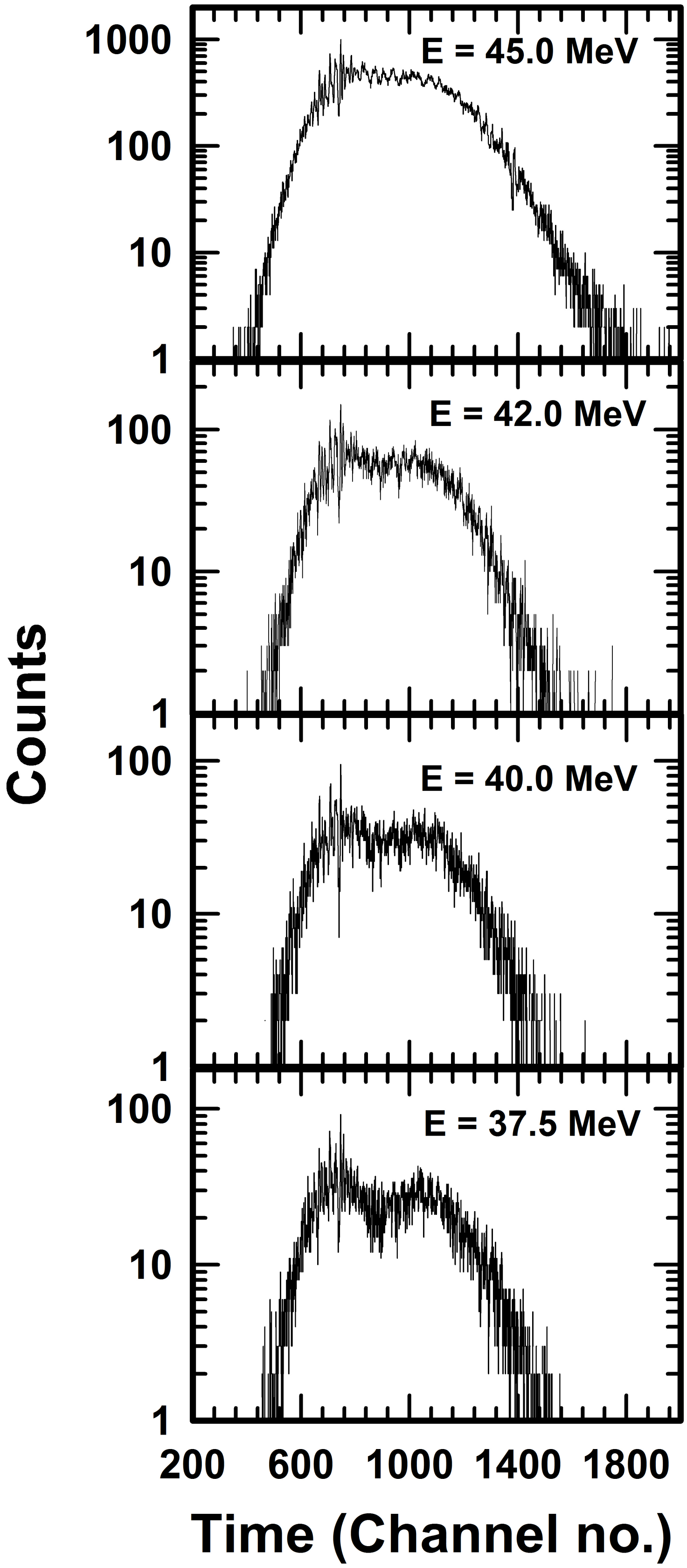

Figure 4.8: TAC spectrum for start signal from MWPC1 and stop signal from MWPC2 for various beam energies for ^{9}Be + ^{232}Th reaction.

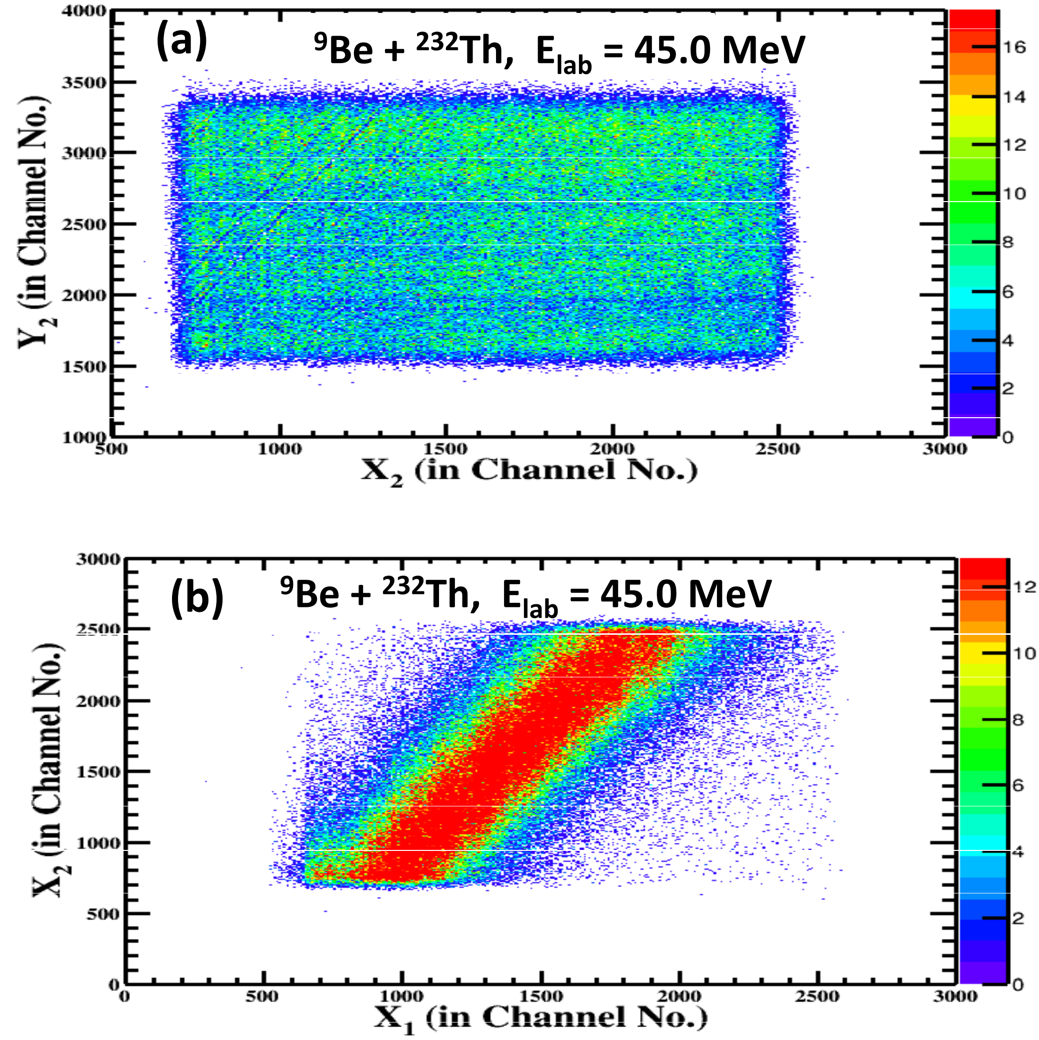

Figure 4.9: (a) Two dimensional plot between X and Y positions of MWPC1 for ^{9}Be + ^{232}Th reaction. (b) Two dimensional plot between X positions of two MWPCs for ^{9}Be + ^{232}Th reaction.

well as those of fission fragments in the target have been taken in to account. For heavy particles like fission fragments the small angle scattering can't significantly change their track from straight path as is evident by measurements shown in Fig. 3.5. The events for which $V_{\parallel}/V_{cm}$ is negative corresponds to stopped-fission as they are beyond 180° in folding angle distribution. It can be seen that incomplete fusion-fission events are merged in complete fusion-fission events. It is so because of a very small difference in mass units of projectile and breakup fragments as compared to fission fragments leading to negligible change in their velocities. Nevertheless, the intense small region around the center of correlation plot mostly correspond to complete fusion-fission events. To obtain

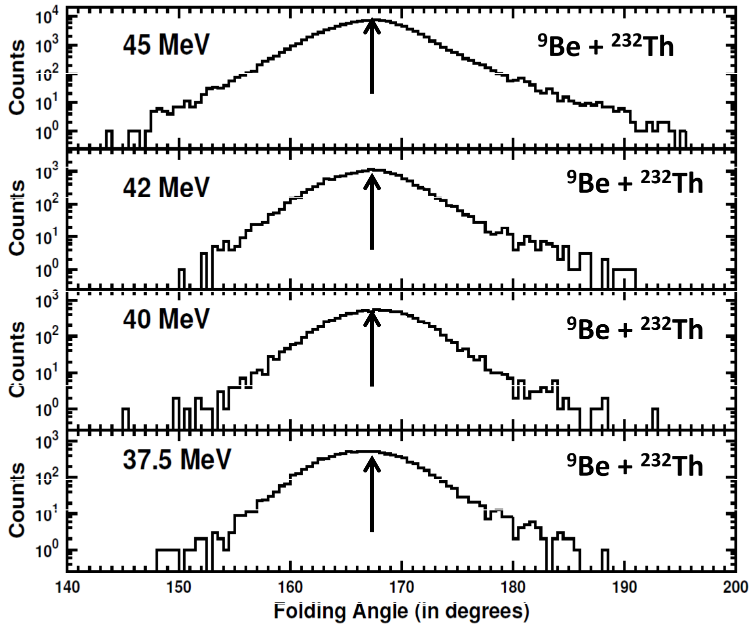

Figure 4.10: Folding angle distribution obtained at various energies for ^{9}Be + ^{232}Th reaction. The arrows indicate the theoretical folding angle calculated by using Viola's systematics.

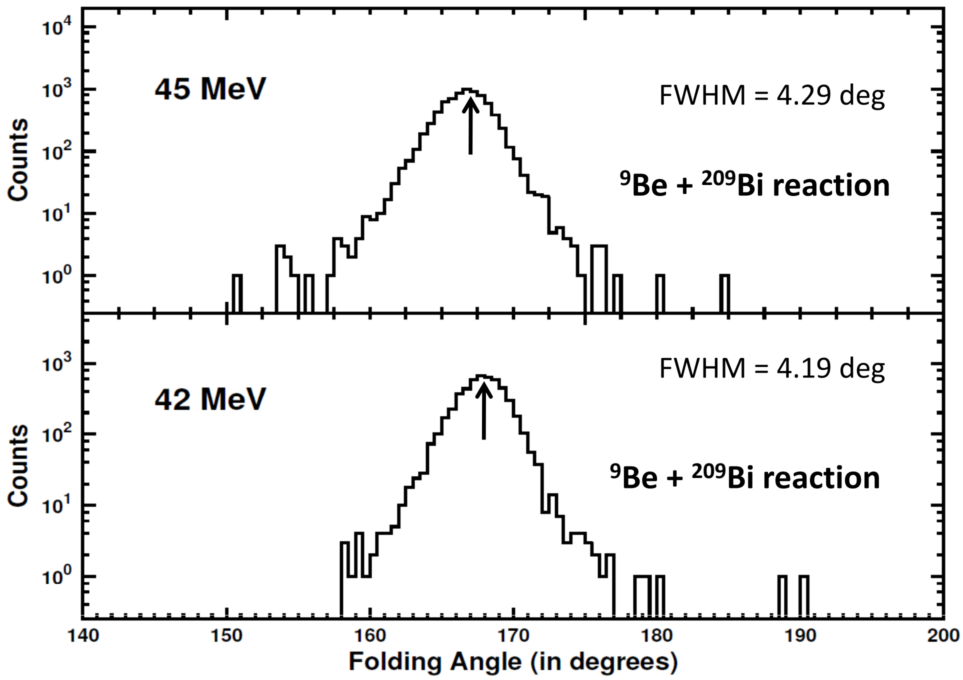

Figure 4.11: Folding angle distribution obtained at various energies for ^{9}Be + ^{209}Bi reaction. The arrows indicate the theoretical folding angle calculated by using Viola's systematics.

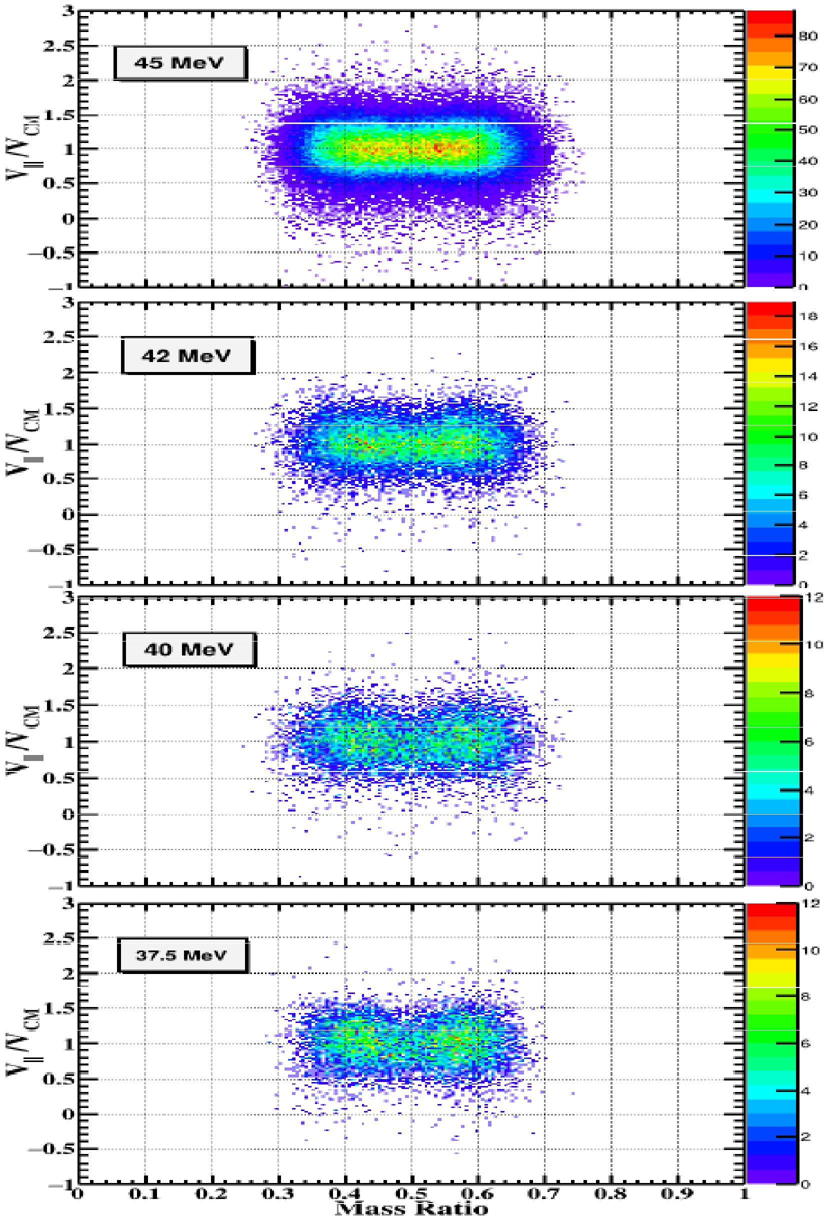

Figure 4.12: Two dimensional plot of mass ratio vs parallel component of velocity of fissioning nucleus with respect to beam direction for $^{9}Be + ^{232}Th$ reaction.

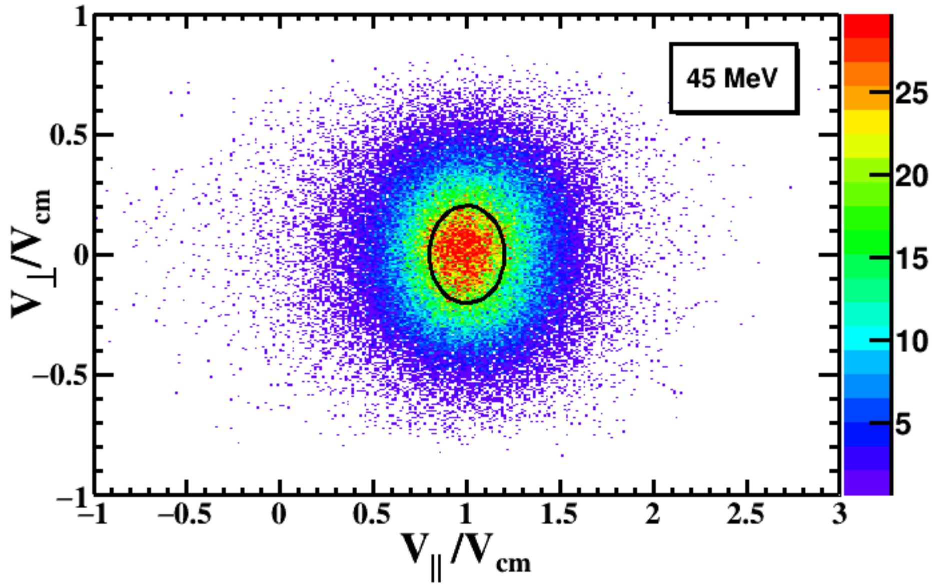

Figure 4.13: Correlation between parallel and perpendicular velocities of fissioning nucleus for ^{9}Be + ^{232}Th reaction.

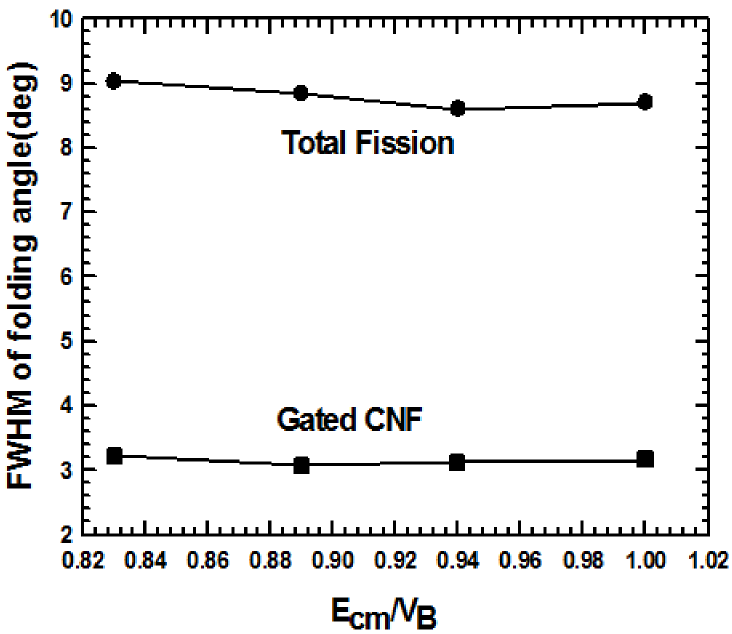

Figure 4.14: Full width at half maximum of folding angle distribution for ^{9}Be + ^{232}Th reaction.

mass distribution corresponding to complete fusion, a gate was put on the correlation between parallel and perpendicular velocities of fissioning nucleus. The gate corresponds to $[(V_{\|}/V_{cm} - 1)^2 + V_{\perp}/V_{cm}]^{1/2} < 0.2$ for ^{9}Be + ^{232}Th reaction. The radius of the applied gate can be smaller than 0.2, but in that case the statistics become quite low and the error becomes too large. The applied gate does not consist of only complete fusion events but a mix of complete and incomplete fusion events. Nevertheless, as the radius is made smaller the percentage of complete fusion events relative to total events will go higher. It was applied to show the effects that take place with increasing percentage of complete fusion events. This method was adopted earlier for selecting the complete fusion-fission events in ^{6,7}Li + ^{238}U reactions [46]. A similar gate was applied to ^{9}Be + ^{209}Bi reaction. The full width at half maximum (FWHM) of folding angle distribution for total fusion events are shown in Fig. 4.14 for ^{9}Be + ^{232}Th reaction. The above gate was also put on folding angle distribution for ^{9}Be + ^{232}Th reaction. The gated full width at half maximum (FWHM) of folding angle distribution are also shown in Fig. 4.14. It should be mentioned here that the broadening in the ungated folding angle distribution may also have contribution from small angle scattering of fragments while escaping the target.

4.3.1 Extracting mass distribution

For the mass distribution measurement, the MWPCs were kept at the folding angle for symmetric fission, calculated from the Viola systematics [112]. The MWPC1 was mounted at a fixed angle (θ_{lab} = 71°) and MWPC2 was kept at an appropriate angle, which depends on the beam energy. The fission events were separated by putting a gate to select the FF1-FF2 from the two dimensional plot of T1 vs T2 [Fig. 4.6(b)]. The velocity distribution as well as the mean velocities are similar for the fission fragments measured by both the MWPCs and the details are given in the recently published paper [111]. The fission fragments from full momentum transfer events (for FF and QF) were exclusively selected from the correlation of the velocity of the fissioning system ($V_{\|}$) in the beam direction

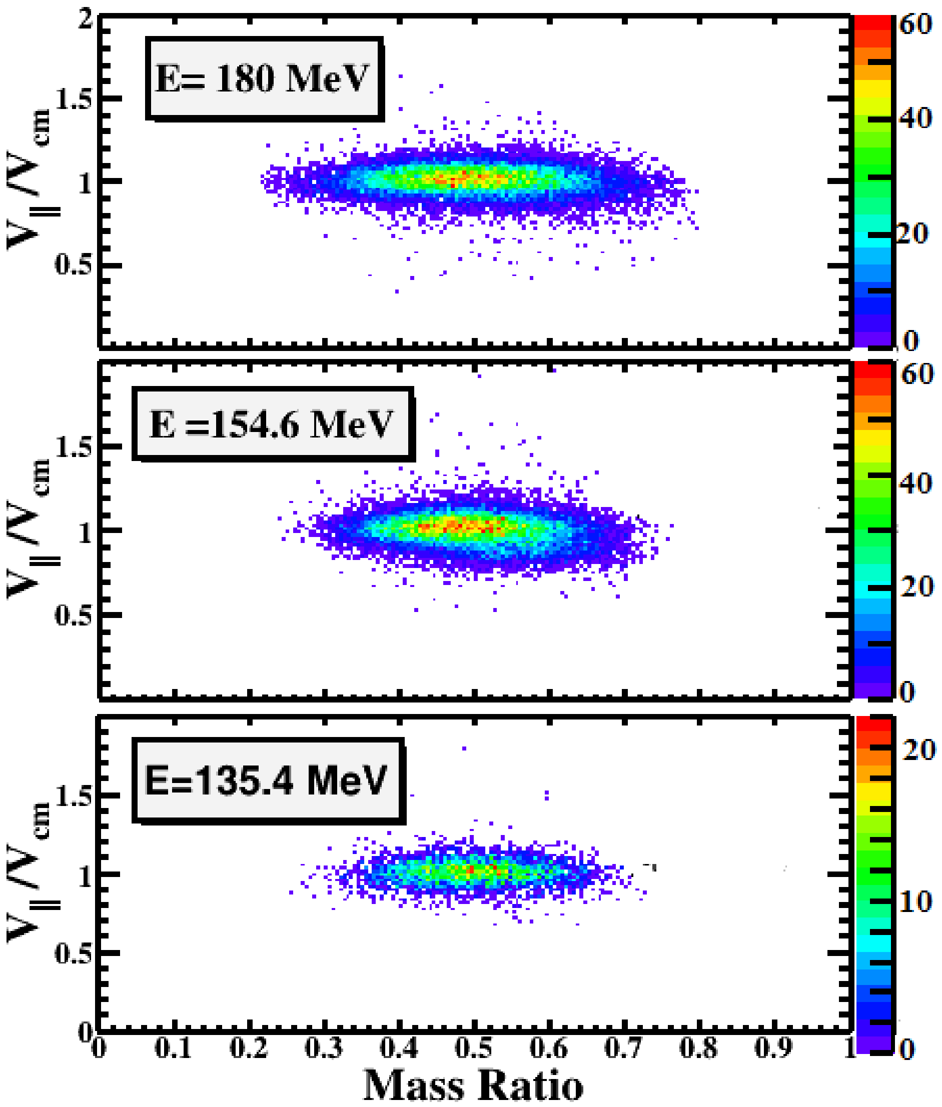

Figure 4.15: Distribution of ratio of parallel components with $V_{c.m.}$ plotted as a function of mass ratio at E = 180.0, 154.6, 135.4 MeV.

relative to the recoil of the fused system and the velocity perpendicular to the reaction plane ($V_{\perp}$) as well as the correlation of the polar and azimuthal angles of the fragment (θ and ϕ respectively) with respect to the beam axis. To obtain the mass distribution, the conservation of linear momentum was used for transforming the velocities to c.m. frame. After applying kinematic transformations, the center of mass velocities ($V_{1c.m.}$, $V_{2c.m.}$) of both the fragment masses, M_1 and M_2 were obtained. The mass ratio, $M_R = M_1/(M_1 + M_2)$ was determined from the ratio of the velocities in the center-of-mass frame (c.m.). In Fig. 4.15 we have plotted the ratio of parallel components of velocities with $V_{c.m.}$ as a function of mass ratio for 180.0, 154.6 and 135.4 MeV. It clearly shows that very negligible contribution of transfer induced fission corresponding to partial momentum transfer are present for this reaction.

Chapter 5

Results and discussion on fission fragment mass distributions for ^{28}Si + ^{197}Au, ^{9}Be + ^{232}Th,^{209}Bi reactions

5.1 Results and Discussion

The fragment masses were determined by applying the conservation law for momentum and mass, with the assumption that mass of the composite system is equal to the sum of the projectile and target masses. Since double velocity method was used to obtain mass distribution, the effect of neutron evaporation from fragments will broaden the mass distribution. In spite of neutron evaporation, the average velocity of fragments will remain the same since neutron emission is isotropic in rest frame of fragment. Fig. 5.1 shows the fragment mass distribution plots for various beam energies ranging from 134.5 to 180.0 MeV.

For all the beam energies, the distributions are symmetric Gaussian with a peak position at around $A_{CN}/2$. The variance of fission fragment mass distributions (σ_m^2) of the Gaussian

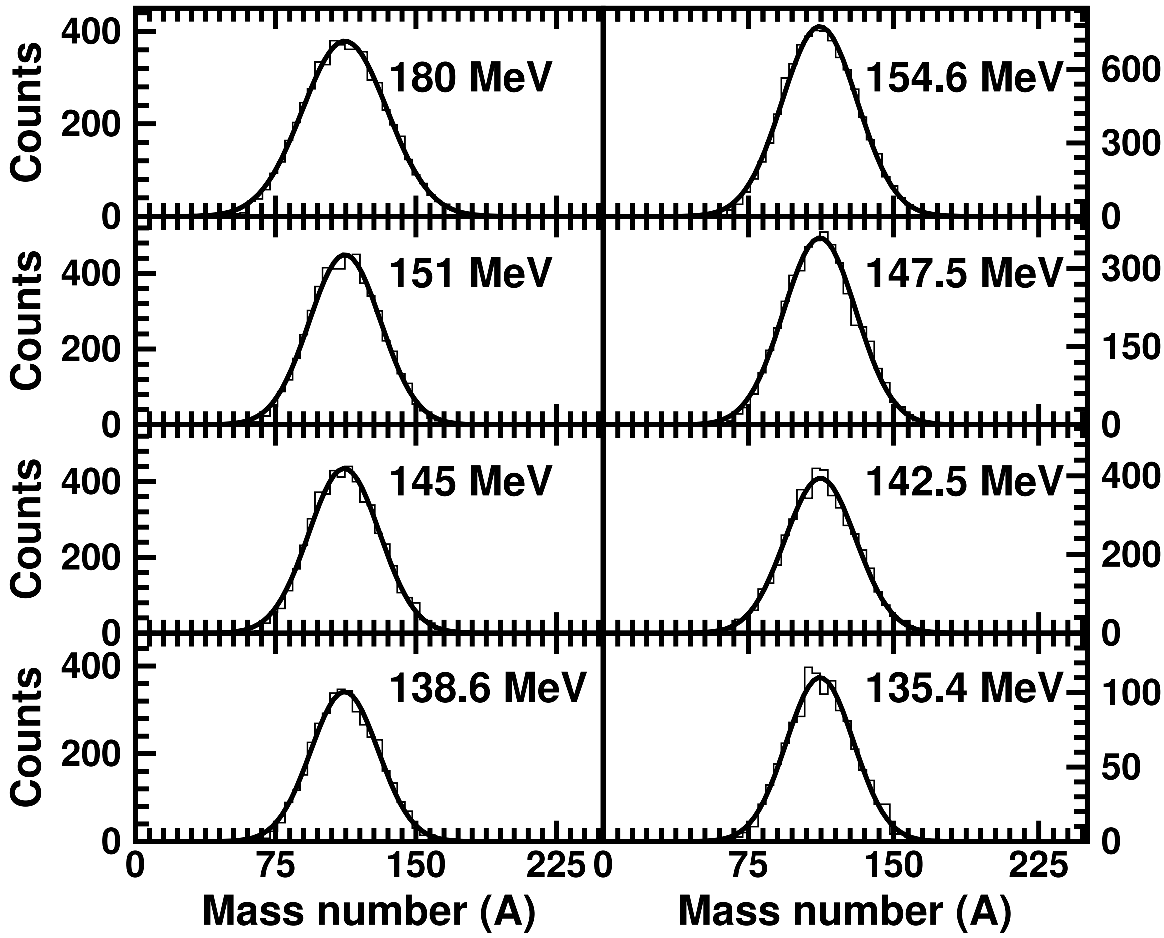

Figure 5.1: Measured mass distributions of fission fragments for ^{28}Si + ^{197}Au reaction at different beam energies along with fittings using single Gaussian are shown by solid lines.

fits to the mass ratio distributions are plotted as a function of the beam energy, as shown in Fig. 5.2. At energies above the V_b (shown by arrow in the figure), the experimental mass width shows a decreasing trend with the reduction of beam energies. However, it shows a sudden change from monotonic decrease to a saturation for energies close to the V_b. As the beam energy is further reduced, once again a decreasing trend has been observed. In the present system, ^{28}Si projectile is highly oblate deformed (β_2 = -0.478), which may contribute to orientation dependent fusion-fission process. Thus, the anomalous variation of mass width at energies near the barrier, are similar to the earlier reported results of target/projectile orientation dependent QF reactions [93–96, 99–102].

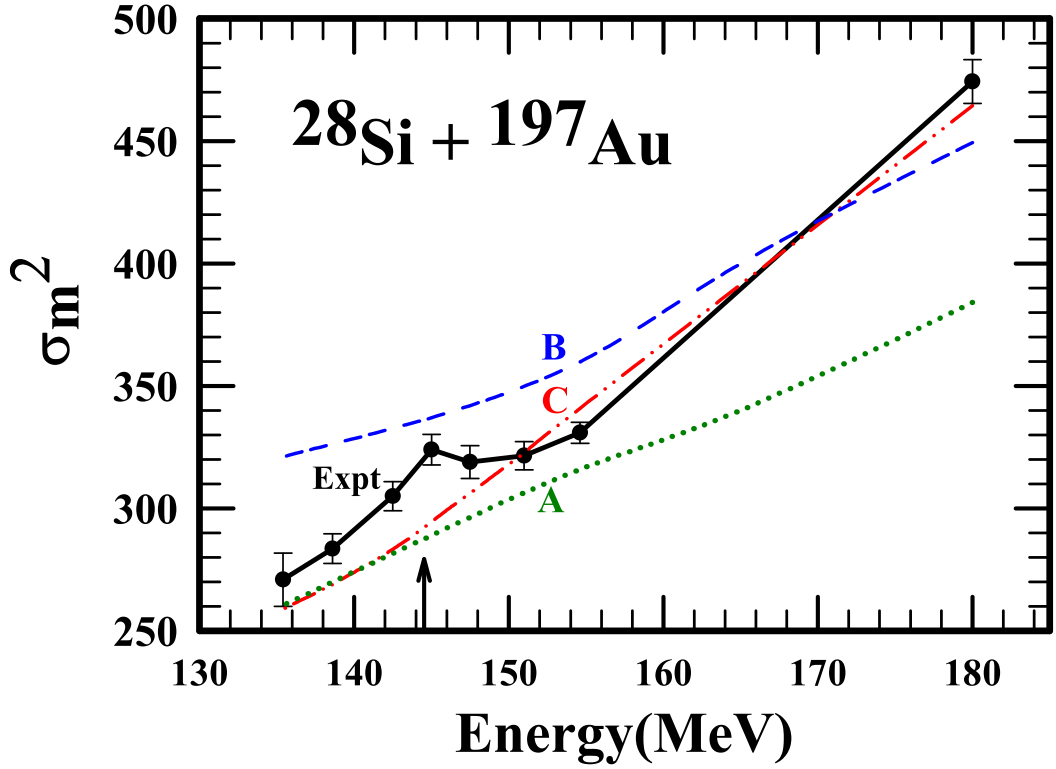

Figure 5.2: Dependence of the variance of the fission fragment mass distribution (σ_m^2) with beam energy. Dotted and dashed lines, marked with A (green) and B (blue) are dynamical calculations corresponding to wall-and-window dissipation and modified wall-and-window dissipation, respectively. Dash-dotted line, marked with C (red) is statistical model calculation. The arrow shows the Coulomb barrier (E_{Lab} = 144.5 MeV).

5.2 Theoretical Interpretation

To understand the anomalous behavior of the variation of the fragment mass width at near and sub-barrier energies, we have carried out a two-dimensional dynamical calculation that accounts only for the compound nuclear decay without any non-compound contribution. We numerically solve the Langevin equations for the collective coordinates c and α representing elongation and mass-asymmetry of the nucleus, respectively. The equations are given by [113]:

$$\begin{aligned}
\frac{dp_i}{dt} &= -\frac{p_j p_k}{2}\frac{\partial}{\partial x_i}(\mathcal{M}^{-1})_{jk} - \frac{\partial F}{\partial x_i} \\
&\quad - \eta_{ij}(\mathcal{M}^{-1})_{jk}p_k + g_{ij}\Gamma_j(t), \\
\frac{dq_i}{dt} &= (\mathcal{M}^{-1})_{ij}p_j,
\end{aligned} \tag{5.1}$$

where $(q_1, q_2) \equiv (c, \alpha)$ and p_i is the momentum conjugate to q_i. The dissipation tensor η_{ij} is calculated from the wall-and-window formula for nuclear dissipation [113–115]. The inertia tensor $\mathcal{M}_{ij}$ is obtained using the Werner-Wheeler approximation [116] to the nuclear fluid dynamics. The time-correlation property of the random force $(g_{ij}\Gamma_j(t))$ is assumed to follow the relation $\langle\Gamma_k(t)\Gamma_l(t')\rangle = 2\delta_{kl}\delta(t-t')$. The strength of the random force (g_{ij}) is related to the dissipation coefficients through the fluctuation-dissipation theorem: $\sum_k g_{ik}g_{jk} = \eta_{ij}T$, where the temperature T (in MeV) of the fissioning nucleus is given by $T = \sqrt{E^*/a}$. Here, a is the level density parameter calculated from Ignatyuk's prescription [117] and E^* represents the excitation energy of the fissioning system. The free energy F is calculated from the two-dimensional PES $V(c, \alpha)$ as: $F = V - (a - a_0)T^2$; a_0 being the value of a for spherical shape. The Yukawa-plus-exponential double-folding procedure [118] is used to obtain V. A typical PES for ^{225}Np, corrected with the rotational energy corresponding to the most-probable angular momentum at $E = 154.6$ MeV, is shown in Fig. 5.3. We have used the scission condition as described in [113].

The calculated σ_m^2 is plotted in Fig. 5.2 (marked as A). Although the experimental σ_m^2 is underestimated, specifically at a high excitation energy, it follows a monotonically decreasing trend at near and sub-barrier energies, in contrast to the experimental observation. Further, another calculation is performed with a modified η_{ij} where $\eta_{\alpha\alpha}$ is enhanced by a factor of two. As shown in Fig. 5.2 (marked as B), the corresponding value of σ_m^2 mostly overestimates the experimental values. It clearly indicates the necessity of an excitation energy dependence in η_{ij} to reproduce the experimental σ_m^2. A detailed analysis of this excitation-energy dependence will be presented in our future work. However, the nature of σ_m^2 around the Coulomb barrier energy, observed in the present experiment, can not be extracted with a single prescription for η_{ij}.

Next, we performed a statistical model estimation of σ_m^2 that assumes the decay of an equilibrated compound nucleus [119]. For this purpose, the saddle ridge on the PES is defined by connecting the locus of maxima along c-coordinate as shown in Fig. 5.3. Neglecting the contribution from saddle-to-scission dynamics, the statistical probability P of a particular mass fragmentation is assumed to be uniquely related to the α on the saddle ridge through the relation: $P(\alpha) = K \exp\{-F_B/T\}$, where the fission barrier F_B is obtained by subtracting the ground state potential from the potential on the saddle ridge. K is a normalization constant independent of α. The corresponding theoretical values of σ_m^2 underestimates the experimental values since the dynamical effects and the excitation energy dependence, as discussed in the previous paragraph, can not be included in this simple model. Therefore, to account for these effects, we scale the calculated σ_m and a constant multiplication factor of 1.25 is found to be sufficient to reproduce the appropriate energy dependence far away from V_b. The corresponding σ_m^2 is plotted in Fig. 5.2 (marked as C). As in the case of dynamical calculations,the experimentally observed behavior of σ_m^2 around V_b can not be explained within this statistical model approach. Thus, the theoretical calculations based on the compound nuclear decay could not explain the anomalous change in mass distribution width near the Coulomb barrier energy.

It is to be mentioned that the variation of the width of the mass distributions for the same CN nucleus having same mass, produced in ^{16}O+^{209}Bi reaction [99, 107] showed a monotonic increase with excitation energy near the V_b, without any anomaly. In heavy systems if the value of $Z_pZ_t > 1600$, the compactness of the exit channel configuration prevent the formation of a mono-nucleus and thus QF occurs. However, in Si-induced reaction, even system with much lower Z_pZ_t value (~800) QF was reported [120]. Our results indicate that the system ^{28}Si + ^{197}Au having Z_pZ_t (= 1106) is also prone to undergo the QF process. The system under investigation has entrance channel mass asymmetry, α

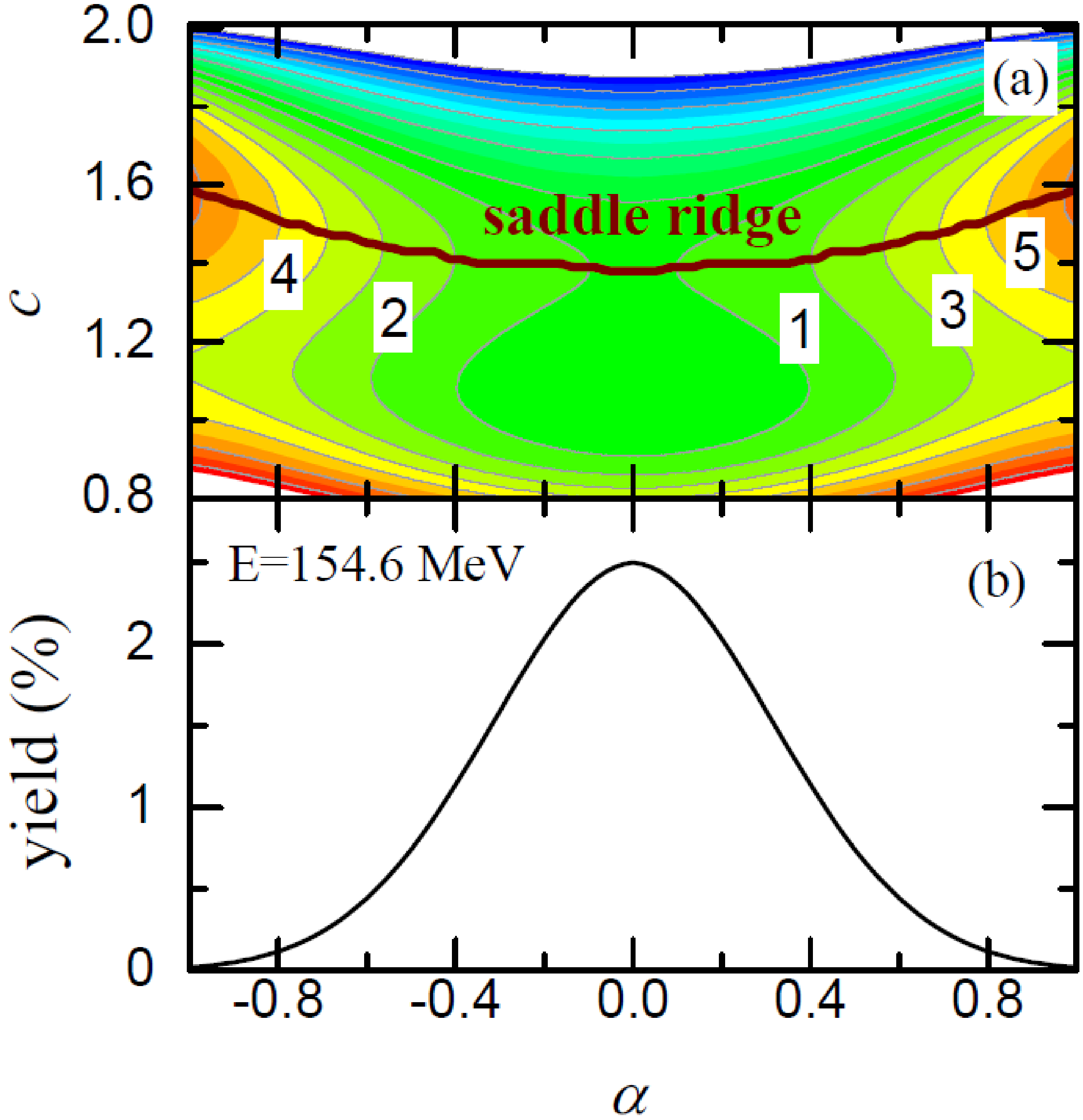

Figure 5.3: Upper panel: Potential energy surface (in MeV) for the compound nucleus ^{225}Np calculated as a function of c and α. The saddle-ridge is shown by the thick solid line. Lower panel: Normalized fission fragment mass distribution calculated on the saddle-ridge.

= (A_T - A_P)/(A_T + A_P) (0.751) much lower than the Businaro Gallone asymmetry (α_{BG}), which is 0.873 [121]. The anomalous increase in the width of the mass distribution may be due to the presence of QF for near and sub-barrier energies. Earlier studies has established that for systems with entrance channel mass asymmetry higher than α_{BG}, there is a mass flow from the projectile to the target [81], thereby leading to increasing mass asymmetry establishing a compact shaped mono-nucleus as in the case of ^{16}O + ^{209}Bi reaction. However, for systems with mass asymmetry lower than α_{BG}, as in the case of ^{28}Si+ ^{197}Au, mass flow is in the direction of more symmetric di-nuclear system. Before forming a equilibrated compound nucleus, it may pass over a mass-asymmetric saddle and thus lead to quasifission.

The mass distribution corresponding to total fusion events is shown in Fig. 5.4 for ^{9}Be + ^{232}Th reaction. The obtained mass distribution is asymmetric having two peaks. The peak to valley ratio (P/V) for obtained mass distribution increases with decreasing excitation energy. The peak to valley ratio is sensitive to the excitation energy of fissioning nucleus. The increasing P/V is an indication of decreasing available excitation energy to the fissioning nucleus. To obtain the mass distribution corresponding to complete fusion, the gate mentioned in Fig. 4.13 was applied to the correlation between parallel and perpendicular velocities of fissioning nucleus. After applying the gate, P/V is lower than that obtained for total fusion events. This low P/V indicates that a higher excitation energy is available for complete fusion events as compared to that obtained for total fusion events. The reason for lower excitation energy for total fusion events is the significant presence of incomplete fusion events corresponding to capture of breakup fragments of projectile by target followed by nuclear fission. The gated mass distribution for ^{9}Be + ^{209}Bi reaction is shown in Fig. 5.5. The mass distribution is symmetric gaussian peaking at A = 109. Unlike the ^{9}Be + ^{232}Th reaction, the mass distribution is symmetric even at a very low excitation energy (E^* = 26.0 MeV), because of the low fissility of ^{209}Bi nucleus as compared to ^{232}Th. This arises from the difference in shell structure effects on the potential energy surface for both the mono-nucleus and the fission fragments.

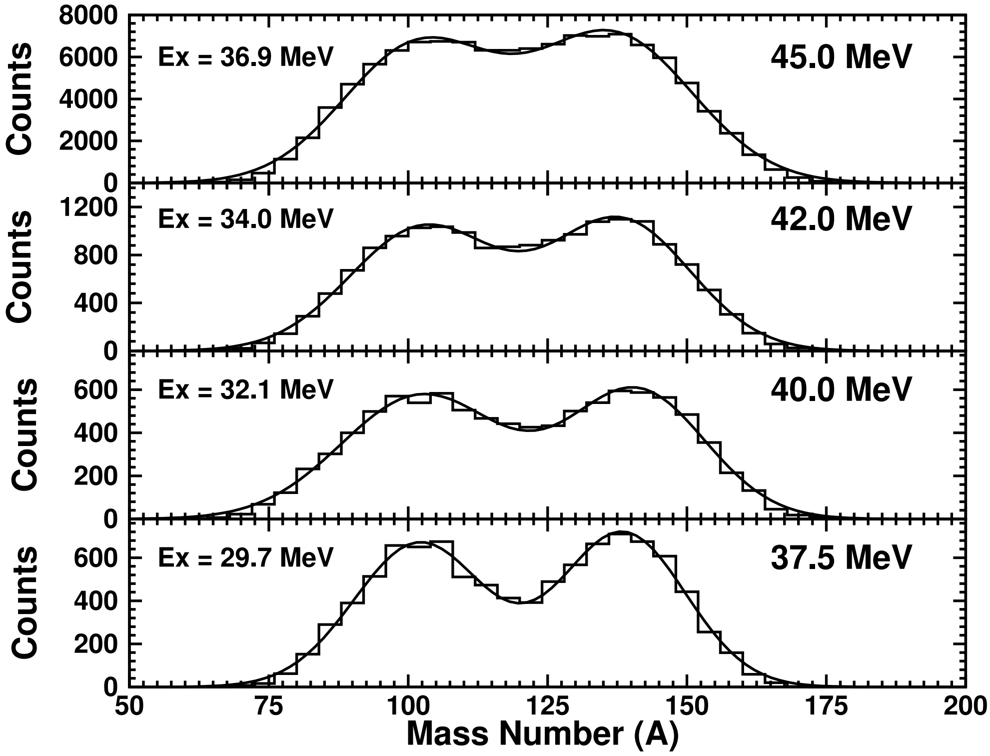

Figure 5.4: Mass distribution corresponding to total fusion obtained at various energies for ^{9}Be + ^{232}Th reaction.

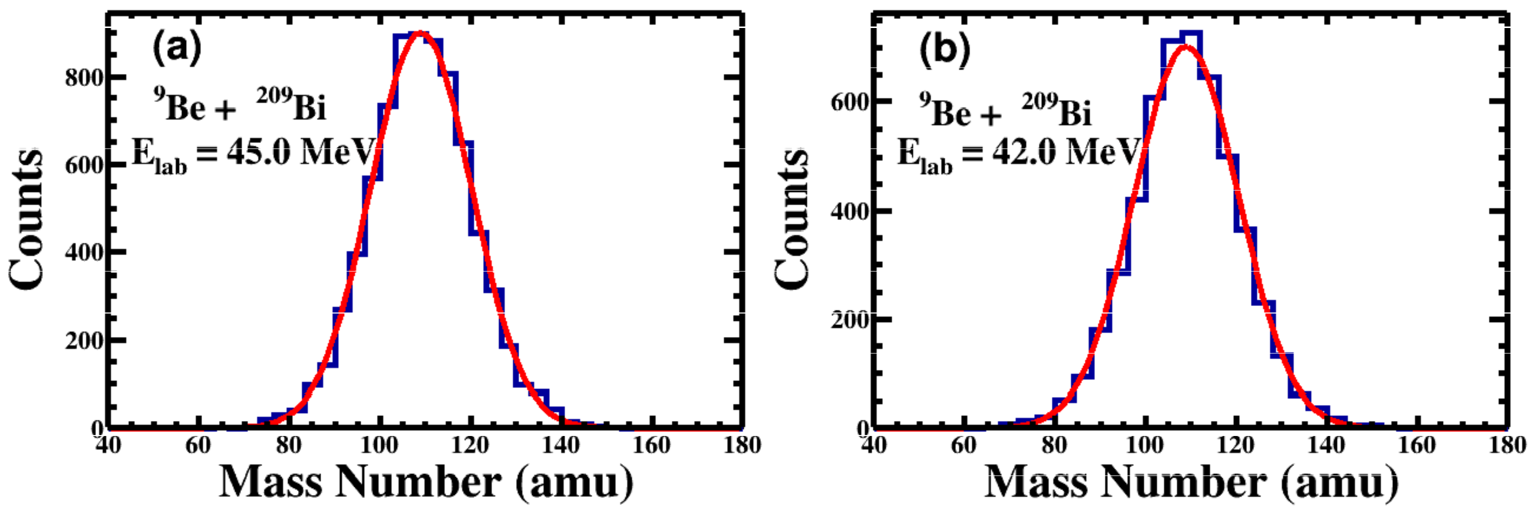

Figure 5.5: Mass distribution obtained at various energies for ^{9}Be + ^{209}Bi reaction.

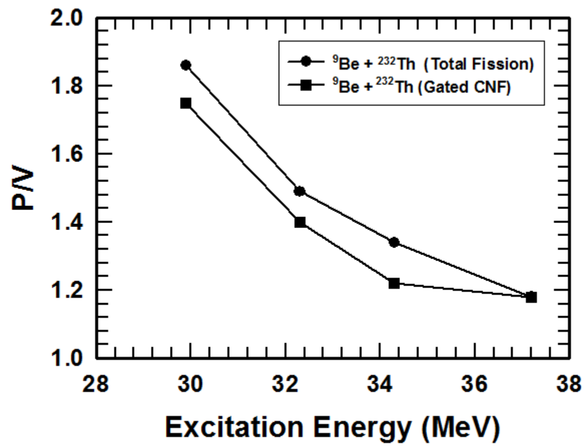

Figure 5.6: Peak to valley ratio obtained at different energies for ^{9}Be + ^{232}Th reaction.

For ^{9}Be + ^{232}Th reaction, we have obtained the fission cross section for different beam energies by placing a gate of ± 2°on the MWPC1, so that all the complementary fragements are detected in MWPC2. The out of plane coverage is also ± 2°. The experimental cross sectional values are plotted in Fig. 5.7. In the same figure we have also plotted the cross section obtained theoretically using the coupled channel code CCFUS [122]. In the present calculation we have assumed axially symmetric shapes of the ^{232}Th target, characterised by nuclear quadrupole and hexadecapole deformation parameters $\beta_2 = 0.217$ and $\beta_4 = 0.09$. The following inelastic channels were included in the calculations: one of them being the 0.77 MeV state of ^{232}Th with $\beta_3 = 0.09$ [123]. The deformation of ^{9}Be is very large ($\beta = 1.3$) [124]. As the reaction studied produces highly fissile compound nucleus, all the fusing events will undergo fission. The calculated fusion cross section has been compared with the present data along with the earlier measured cross section by Appannababu et al. [125]. The enhancement in fission cross section was observed at sub- barrier energies. This may be due to low breakup threshold of ^{9}Be projectile causing enhancement in the breakup fusion-fission process.

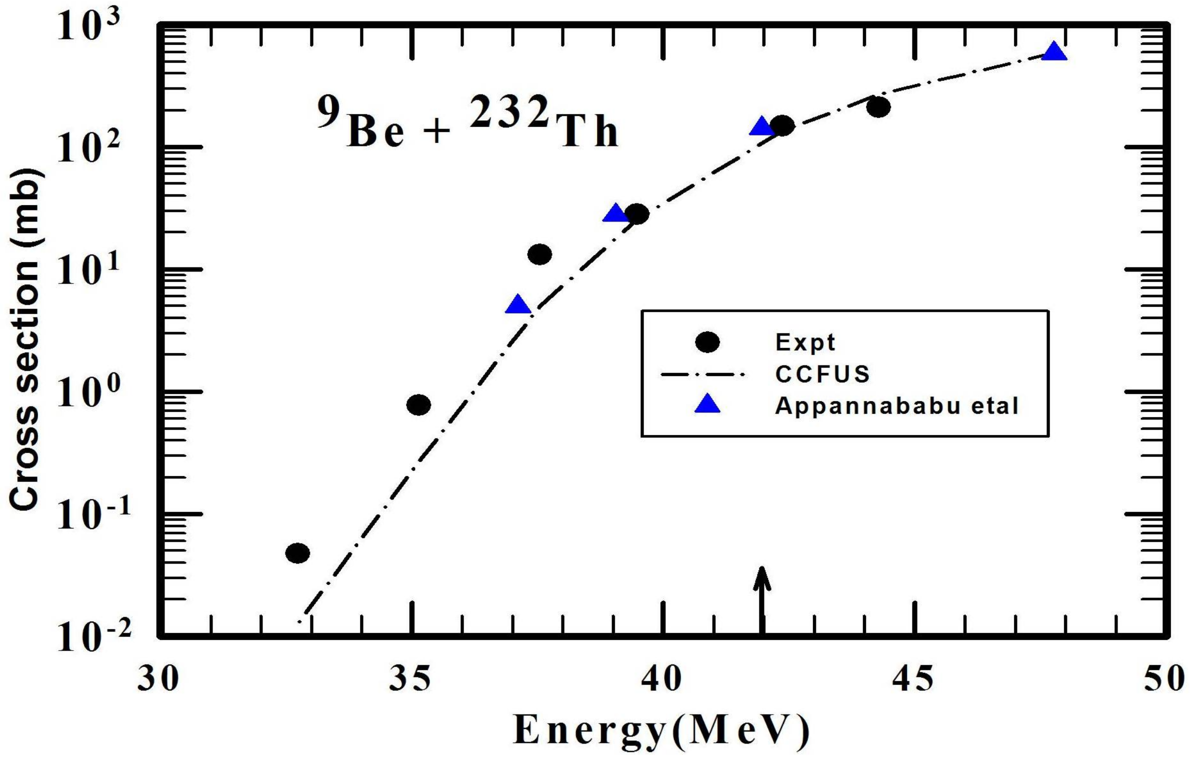

Figure 5.7: Comparision of experimental excitation function with CCFUS excitation function.

Chapter 6

Summary and Conclusion

The understanding of fission dynamics from fragment mass distribution studies is getting improved due to the availability of large experimental data as well as theoretical calculations on fusion-fission and quasi-fission reactions. The fusion-fission process corresponds to complete amalgation of projectile and target followed by fission of the compound nucleus. In fusion-fission, complete equilibration in mass, angular momentum, energy and shape degrees of freedom take place. In some cases, the unstable elongated di-nucleus may also re-separate into two heavy fragments instead of diffusing to more compact stable equilibrated shapes and this premature separation of fission fragments (FFs) is called QF. The fission dynamics has been studied as a function of beam energy around the Coulomb barrier and the deformation of target or projectile. The deviation of the width of the observed mass distribution as a function of excitation energy from theoretical predictions has been interpreted as an experimental signature of the QF events in addition to compound nucleus fission. The main hurdle in the formation of heavy/super heavy evaporation residues is the QF process. It is important to understand the dynamics of QF reactions.

The present thesis focusses on the study of fission dynamics of heavy ion-induced reactions, in medium and heavy mass nuclei, through measurements of fission fragment mass distributions. The experimental measurements were carried out at BARC-TIFR Pelletron-LINAC Facility, Mumbai using heavy ion beams. These experiments were performed in the General Purpose Scattering Chamber at TIFR. The present studied reactions are

1. Fission fragment mass distributions for the reaction ^{28}Si + ^{197}Au.

2. Fission fragment mass distributions for the reaction ^{9}Be + ^{232}Th,^{209}Bi

During the thesis work, we have developed indigenously two Multi-wire proportional counter (MWPC) detectors for the simultaneous measurement of fission fragment time of flight. The detectors were tested to ascertain the performance characteristics for fission fragments from ^{252}Cf source. The velocity distribution of fission fragments from spontaneous fission of ^{252}Cf source has been measured by employing a new TOF method using a BaF_2 detector as "Start" and MWPC as "Stop" detector. The position information has been obtained by using the delay-line method and the position resolution is about 1.0 mm in both X and Y directions. The velocity distribution for FFs from ^{252}Cf obtained from the measured TOF using two detectors (BaF_2 and MWPC) having fast timing signals and known travel path by the fission fragments is found to be very accurate. The width of the velocity distribution has been measured for various fragment energies by degrading them using Mylar foils of four different thickness. It is observed that the width of the distribution decreases with the reduction in the fragment energies for the heavy fission fragments, but the light fragments show a weak dependence on energy. Since the anode pulses from the MWPC are very fast (rise time $\sim$ 6 ns), two similar MWPCs have been found to be suitable for studying the fragment mass distribution in heavy-ion induced fission reactions providing a mass resolution of about 4.26%. The mass width will further broaden due to the evaporation of the neutrons from the fission fragments.

Large experimental data sets on fission fragment mass distributions have come up during last few decades in order to understand the dynamics of fissioning heavy nucleus. In the present thesis, we have studied the mass distribution of fission fragements for the reaction

^{28}Si + ^{197}Au to understand the role of QF at near barrier energies. The experiment was carried out at Pelletron-LINAC Facility at TIFR by accelerating the beam first with the pelletron accelerator to 150 MeV and it is further accelerated up to a maximum 180 MeV in the present experiment using the superconducting linac booster. The Pulsed beam had a period of 107.3 ns and a width of ~ 1.5 ns. The general purpose scattering chamber was used in the present experiment for carrying out fission fragment mass distribution measurements. Two indigineously developed MWPC detectors were used for measuring the time of flight of the fission fragments simultaneously to obtain the velocity distribution of the fragments. The velocity distribution has been used to obtain the mass of fission fragments from the known kinematical conditions. The data was analysed using root software. The contribution of the transfer induced fission component was negligibly small in the present measurement using heavy stable projectile (^{28}Si). The experimental measurements were carried out for energies 25% above the Coulomb barrier to 6% below the barrier. At all beam energies the mass distribution could be fitted with a symmetric gaussian distribution peaking at (A_T + A_P)/2. The experimental variance of the mass distribution shows a sudden change from monotonic decrease to a saturation at energies close to the Coulomb barrier and again a decreasing trend at sub-barrier energies. The variance of the mass distribution was also obtained from dynamical and statistical model calculations for the fission of a fully equilibrated compound nucleus. Both of the theoretical calculations show a monotonic change of the mass variance around the Coulomb barrier. The anomalous dependence of the fission fragment mass width at energies around the barrier may be due to the dominance of the QF process as compared to compound nuclear fission. Detailed measurements by varying the experimental parameters using several projectile-target systems on angular anisotropies and mass-angle correlations will provide very useful information on fission dynamics. Extensive theoretical calculations for non-equilibrated systems are required for a full understanding of various parameters controlling the QF and fully equilibrated compound nuclear fission processes.

Another measurement was carried out to study the mass distribution using a stable weakly bound projectile ^{9}Be to bombard on ^{232}Th, ^{209}Bi targets. This measurement is interesting due to observation of an asymmetric mass distribution with increasing peak to valley ratio (P/V) with decreasing beam energy in the ^{9}Be + ^{232}Th reaction. It is not yet clear whether the weakly bound projectile breaks into two parts and only part of it fuses with the target nucleus producing fission fragments with a total mass less than sum of the target mass (A_T) and the projectile mass (A_P). However, for ^{9}Be + ^{209}Bi reaction, we observed symmetric fission peaking at A = 109. The experiment was performed using a bunched beam in the energy range 37.5 MeV to 45 MeV from the Pelletron facility, TIFR. Two MWPCs mounted at the folding angle were used for coincidence measurement of complementary fission fragments. The mass distribution was obtained using the condition that the mass ratio distribution is reflection symmetric around $\theta_{cm} = 90°$. The experimental folding angle distribution was peaking at an angle predicted by Viola systematic at all energies. From the present measurement of fission fragment mass distributions, it is observed that either complete fusion or break-up induced fission are the main dominating processes, where we observe that sum of mass of two fission fragments is equal to mass of the fissioning nucleus for all energies. From the present measurement, we observe that the P/V values increases with the reduction in excitation energy of the fissioning nucleus and this behaviour is similar to the earlier observations for various weakly bound projectiles bombarding on different targets. The cross section values measured in the present experiment agree quite well earlier measured values obtained from the measurement of fission fragment angular distributions. The enhancement of the cross section at sub-barrier energies as compared to the CCFUS calculations may be due to break-up fusion of ^{9}Be projectile.

6.1 Future Outlook

In several laboratories experimental efforts have been going on in the investigation of the formation of super-heavy nuclei. Such experiments are extremely challenging as the formation of very heavy/super-heavy elements are heavily suppressed not only by equilibrium fission, but also by a non-equilibrium process called QF. The experimental problem is to identify those variables that hinder compound nucleus formation which can lead to a super heavy element formation. This can be addressed by measuring the characteristics of the fusion, fission and non-equilibrium fission events. Further, it is observed that the entrance channel properties and deformation of the interacting systems, play a major role in the nuclear reaction dynamics of non-compound nucleus fission. In this context we want to extend our investigations through a study of fission fragment mass distributions for compound nuclei of higher masses using several target projectile combinations. In addition, it is also found that one can populate high spin states in heavy nuclei (A$\sim$220-240) through incomplete fusion reactions with stable and weakly-bound projectiles. Furthermore with the availability of radioactive ion beams across the world, it will be possible to study of the properties of very neutron rich fissioning nuclei.

Chapter 6

Summary and Conclusion

The understanding of fission dynamics from fragment mass distribution studies is getting improved due to the availability of large experimental data as well as theoretical calculations on fusion-fission and quasi-fission reactions. The fusion-fission process corresponds to complete amalgation of projectile and target followed by fission of the compound nucleus. In fusion-fission, complete equilibration in mass, angular momentum, energy and shape degrees of freedom take place. In some cases, the unstable elongated di-nucleus may also re-separate into two heavy fragments instead of diffusing to more compact stable equilibrated shapes and this premature separation of fission fragments (FFs) is called QF. The fission dynamics has been studied as a function of beam energy around the Coulomb barrier and the deformation of target or projectile. The deviation of the width of the observed mass distribution as a function of excitation energy from theoretical predictions has been interpreted as an experimental signature of the QF events in addition to compound nucleus fission. The main hurdle in the formation of heavy/super heavy evaporation residues is the QF process. It is important to understand the dynamics of QF reactions.

The present thesis focusses on the study of fission dynamics of heavy ion-induced reactions, in medium and heavy mass nuclei, through measurements of fission fragment mass distributions. The experimental measurements were carried out at BARC-TIFR Pelletron-LINAC Facility, Mumbai using heavy ion beams. These experiments were performed in the General Purpose Scattering Chamber at TIFR. The present studied reactions are

1. Fission fragment mass distributions for the reaction ^{28}Si + ^{197}Au.
2. Fission fragment mass distributions for the reaction ^{9}Be + ^{232}Th,^{209}Bi

During the thesis work, we have developed indigenously two Multi-wire proportional counter (MWPC) detectors for the simultaneous measurement of fission fragment time of flight. The detectors were tested to ascertain the performance characteristics for fission fragments from ^{252}Cf source. The velocity distribution of fission fragments from spontaneous fission of ^{252}Cf source has been measured by employing a new TOF method using a BaF_2 detector as “Start” and MWPC as “Stop” detector. The position information has been obtained by using the delay-line method and the position resolution is about 1.0 mm in both X and Y directions. The velocity distribution for FFs from ^{252}Cf obtained from the measured TOF using two detectors (BaF_2 and MWPC) having fast timing signals and known travel path by the fission fragments is found to be very accurate. The width of the velocity distribution has been measured for various fragment energies by degrading them using Mylar foils of four different thickness. It is observed that the width of the distribution decreases with the reduction in the fragment energies for the heavy fission fragments, but the light fragments show a weak dependence on energy. Since the anode pulses from the MWPC are very fast (rise time $\sim$ 6 ns), two similar MWPCs have been found to be suitable for studying the fragment mass distribution in heavy-ion induced fission reactions providing a mass resolution of about 4.26%. The mass width will further broaden due to the evaporation of the neutrons from the fission fragments.

Large experimental data sets on fission fragment mass distributions have come up during last few decades in order to understand the dynamics of fissioning heavy nucleus. In the present thesis, we have studied the mass distribution of fission fragements for the reaction

^{28}Si + ^{197}Au to understand the role of QF at near barrier energies. The experiment was carried out at Pelletron-LINAC Facility at TIFR by accelerating the beam first with the pelletron accelerator to 150 MeV and it is further accelerated up to a maximum 180 MeV in the present experiment using the superconducting linac booster. The Pulsed beam had a period of 107.3 ns and a width of ~ 1.5 ns. The general purpose scattering chamber was used in the present experiment for carrying out fission fragment mass distribution measurements. Two indigineously developed MWPC detectors were used for measuring the time of flight of the fission fragments simultaneously to obtain the velocity distribution of the fragments. The velocity distribution has been used to obtain the mass of fission fragments from the known kinematical conditions. The data was analysed using root software. The contribution of the transfer induced fission component was negligibly small in the present measurement using heavy stable projectile (^{28}Si). The experimental measurements were carried out for energies 25% above the Coulomb barrier to 6% below the barrier. At all beam energies the mass distribution could be fitted with a symmetric gaussian distribution peaking at $(A_T + A_P)/2$. The experimental variance of the mass distribution shows a sudden change from monotonic decrease to a saturation at energies close to the Coulomb barrier and again a decreasing trend at sub-barrier energies. The variance of the mass distribution was also obtained from dynamical and statistical model calculations for the fission of a fully equilibrated compound nucleus. Both of the theoretical calculations show a monotonic change of the mass variance around the Coulomb barrier. The anomalous dependence of the fission fragment mass width at energies around the barrier may be due to the dominance of the QF process as compared to compound nuclear fission. Detailed measurements by varying the experimental parameters using several projectile-target systems on angular anisotropies and mass-angle correlations will provide very useful information on fission dynamics. Extensive theoretical calculations for non-equilibrated systems are required for a full understanding of various parameters controlling the QF and fully equilibrated compound nuclear fission processes.

Another measurement was carried out to study the mass distribution using a stable weakly bound projectile ^{9}Be to bombard on ^{232}Th, ^{209}Bi targets. This measurement is interesting due to observation of an asymmetric mass distribution with increasing peak to valley ratio (P/V) with decreasing beam energy in the ^{9}Be + ^{232}Th reaction. It is not yet clear whether the weakly bound projectile breaks into two parts and only part of it fuses with the target nucleus producing fission fragments with a total mass less than sum of the target mass (A_T) and the projectile mass (A_P). However, for ^{9}Be + ^{209}Bi reaction, we observed symmetric fission peaking at A = 109. The experiment was performed using a bunched beam in the energy range 37.5 MeV to 45 MeV from the Pelletron facility, TIFR. Two MWPCs mounted at the folding angle were used for coincidence measurement of complementary fission fragments. The mass distribution was obtained using the condition that the mass ratio distribution is reflection symmetric around $\theta_{cm} = 90°$. The experimental folding angle distribution was peaking at an angle predicted by Viola systematic at all energies. From the present measurement of fission fragment mass distributions, it is observed that either complete fusion or break-up induced fission are the main dominating processes, where we observe that sum of mass of two fission fragments is equal to mass of the fissioning nucleus for all energies. From the present measurement, we observe that the P/V values increases with the reduction in excitation energy of the fissioning nucleus and this behaviour is similar to the earlier observations for various weakly bound projectiles bombarding on different targets. The cross section values measured in the present experiment agree quite well earlier measured values obtained from the measurement of fission fragment angular distributions. The enhancement of the cross section at sub-barrier energies as compared to the CCFUS calculations may be due to break-up fusion of ^{9}Be projectile.

6.1 Future Outlook

In several laboratories experimental efforts have been going on in the investigation of the formation of super-heavy nuclei. Such experiments are extremely challenging as the formation of very heavy/super-heavy elements are heavily suppressed not only by equilibrium fission, but also by a non-equilibrium process called QF. The experimental problem is to identify those variables that hinder compound nucleus formation which can lead to a super heavy element formation. This can be addressed by measuring the characteristics of the fusion, fission and non-equilibrium fission events. Further, it is observed that the entrance channel properties and deformation of the interacting systems, play a major role in the nuclear reaction dynamics of non-compound nucleus fission. In this context we want to extend our investigations through a study of fission fragment mass distributions for compound nuclei of higher masses using several target projectile combinations. In addition, it is also found that one can populate high spin states in heavy nuclei (A$\sim$220-240) through incomplete fusion reactions with stable and weakly-bound projectiles. Furthermore with the availability of radioactive ion beams across the world, it will be possible to study of the properties of very neutron rich fissioning nuclei.

Summary

During last few decades, considerable progress has been made in the measurement of fission fragment mass distribution to explain various fission processes in heavy-ion reactions. At energies near the Coulomb barrier, several non-equilibrium fission reactions viz., fast fission (FF), quasi-fission (QF) and pre-equilibrium fission (PEQ) processes compete with fully equilibrated compound nuclear fission (CNF). For studying the entrance channel effects on fission dynamics, it is important to carry out detailed investigations on the role of non-equilibrium processes in fission fragment mass distribution. The nuclear deformation, mass asymmetry and orientation of the heavy reaction partners in the QF reaction can play an important role in the dynamical evolution during the fission process. The study of QF reactions is also very important for predicting optimal reactions for future investigation of superheavy elements. Again, QF is a competitive process in the formation of superheavy elements in heavy-ion reactions. Thus, to optimize the exploration of the superheavy element landscape, the key challenge is to understand the competition between non-compound and compound nuclear fission.

From the study of fission fragment angular anisotropies and mass distributions in different target-projectile combinations, anomalous behaviour has been observed at near and sub-barrier energies. Although, for reactions with ^{19}F on ^{209}Bi show anomalous peak-like structure in mass distribution, there is no anomalous behaviour in mass distribution for the ^{16}O + ^{209}Bi reaction, indicating the absence of QF for this system. To understand the role of the entrance channel on fission fragment mass distribution, we have measured the fission fragment mass distribution for the ^{28}Si + ^{197}Au system at Pelletron-LINAC facility, Mumbai. In this reaction we have populated a fissioning compound nucleus having same mass (A_{CN} = 225), as in the case of the ^{16}O + ^{209}Bi reaction. In the present thesis, we have investigated the role of quasi-fission at near barrier energies by measuring the mass distribution for energies 25% above the Coulomb barrier to 6% below the barrier. From the energy dependence of fragment mass width, it is observed that the experimental

variance of the mass distribution exhibits a sudden change from monotonic decrease to a saturation at energies close to the Coulomb barrier and again a decreasing trend at sub-barrier energies. The variance of the mass distribution was also obtained from dynamical and statistical model calculations for the fission of a fully equilibrated compound nucleus. From this observation it was concluded that the entrance channel mass asymmetry plays an important role in the dynamical evolution of the fission process.

In order to investigate the role of weakly bound nucleus on fission fragment mass distribution, we have carried out an experiment to study the fission fragment mass distribution for ^{9}Be + ^{232}Th,^{209}Bi reactions. For ^{9}Be + ^{232}Th reaction, we observed asymmetric mass distribution with increasing peak to valley ratio (P/V) with decreasing beam energy. However, for ^{9}Be + ^{209}Bi system, symmetric mass distribution was observed even for lower excitation (E^{*} = 26 MeV), which implies that nuclear fissility plays a crucial role in the fission fragment mass distribution.

During the thesis work, we have indigenously developed two Multi-wire proportional counter (MWPC) detectors for the simultaneous measurement of fission fragment time of flight. We have carried out the measurement of the velocity distribution of the fission fragments from ^{252}Cf fission. Simultaneous measurement of fission fragment velocities is arguably better experimental technique for the measurement of fission fragment mass distribution. The details of the development of the MWPC detectors, experimental methods, data analysis and theoretical interpretations are presented in this thesis work.

नाम - निशांत कुमार

Thesis Highlight

Name of the Student : Nishant Kumar

Name of the CI/OCC : Bhabha Atomic Research Centre   Enrolment No.: PHYS01201304027

Thesis Title : Understanding of fission dynamics from fragment mass distribution studies

Discipline : Physical Sciences   **Sub-Area of Discipline : Nuclear Fission**

Date of viva voce : 05-10-2020

At energies near the Coulomb barrier, several non-equilibrium fission reactions viz., fast fission (FF), quasi-fission (QF) and pre-equilibrium fission (PEQ) processes compete with fully equilibrated compound nuclear fission (CNF).

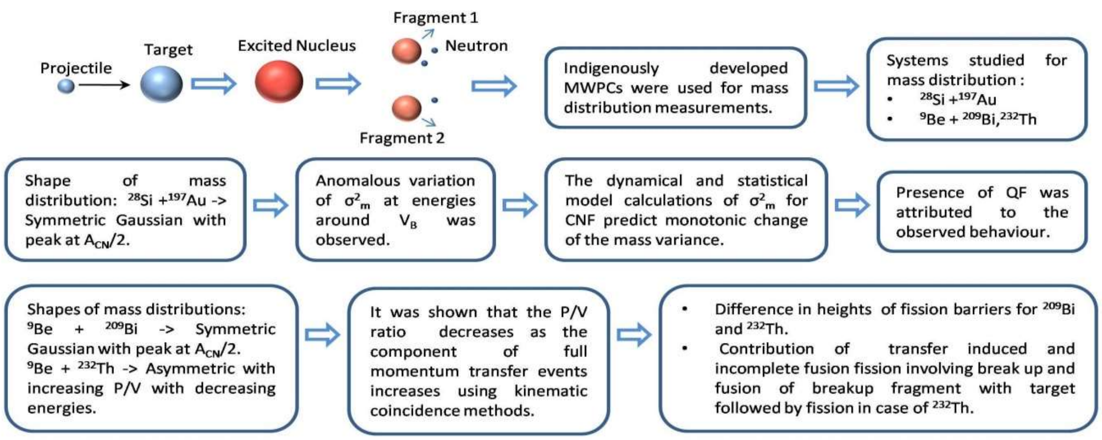

Figure 1. Fission dynamics as seen from fragment mass distribution in systems $^{28}Si + ^{197}Au$ and $^{9}Be + ^{209}Bi, ^{232}Th$.

To understand the role of the entrance channel on fission fragment mass distribution, we have measured the fission fragment mass distribution for the $^{28}Si + ^{197}Au$ system at Pelletron-Linac facility, Mumbai. In this reaction we have populated a fissioning compound nucleus having same mass (A_{CN} = 225), as in the case of $^{16}O + ^{209}Bi$ reaction. From the energy dependence of fragment mass width, it is observed that the σ^2_m (experimental variance of the mass distribution) exhibits a sudden change from monotonic decrease to a saturation at energies close to the V_B (Coulomb barrier) and again a decreasing trend at sub-barrier energies. The variance of the mass distribution was also obtained from dynamical and statistical model calculations for the fission of a fully equilibrated compound nucleus. Presence of QF was attributed to deviation of σ^2_m from theoretical calculations.

In order to investigate the role of weakly bound nucleus on fission fragment mass distribution, we have carried out an experiment to study the fission fragment mass distribution for $^{9}Be + ^{209}Bi, ^{232}Th$ reactions. For $^{9}Be + ^{232}Th$ reaction, we observed asymmetric mass distribution with increasing peak to valley ratio (P/V) with decreasing beam energy. However, for $^{9}Be + ^{209}Bi$ system, symmetric mass distribution was observed even for lower excitation (E* = 26 MeV), which implies that nuclear fissility plays a crucial role in the fission fragment mass distribution.

During the thesis work, we have indigenously developed two Multi-wire proportional counter (MWPC) detectors for the simultaneous measurement of fission fragment time of flight. These detectors were used in the above mass distribution measurements. We have carried out the measurement of the velocity distribution of the fission fragments from ^{252}Cf fission.